EPFL

Thèse n° 8204

Exploring optically active defects in wide-bandgap materials using fluorescence microscopy

Présentée le 1er octobre 2021

Faculté des sciences et techniques de l'ingénieur
Laboratoire de biologie à l'échelle nanométrique
Programme doctoral en microsystèmes et microélectronique

pour l'obtention du grade de Docteur ès Sciences

par

Evgenii GLUSHKOV

Acceptée sur proposition du jury

Prof. L. G. Villanueva Torrijo, président du jury
Prof. A. Radenovic, directrice de thèse
Prof. G. Acuna, rapporteur
Prof. V. Dyakonov, rapporteur
Prof. O. Martin, rapporteur

École polytechnique fédérale de Lausanne

2021

Seize the day, boys.
Make your lives extraordinary.
— John Keating,
Dead Poets Society

To my wonderful Gera
who taught me how the whole life
might not be long enough to love someone…

Acknowledgements

There are so many wonderful people who have in one or another way contributed to me completing this PhD, that it's really hard to thank them all! So, to make this task a little easier, I will proceed in a chronological order (whenever feasible).

First of all, I would like to thank my parents *Tanya and Roma* for giving me life, continuous encouragement and never-ending support. Thank you so much for putting all the efforts into raising your children and giving us the freedom to dream and to chase our dreams!

Naturally, I cannot but thank my grandparents for my wonderful parents, but also for making our childhood so playfully amazing, filled with joy and adventures! Big thanks to my great-great-grandmother *Nina*, who reached the age of 104 years and was a genuine example of longevity and an inspiration for all of us! I was also lucky enough to grow with my great-grandmother *Katya*, who was making the best pancakes I've ever eaten! And my wonderful grandmothers *Tanya and Natasha* were always there during my childhood and teenage years, cooking for us such wonderful meals, always giving us presents and taking care of everything! Thank you so much for all the years you dedicated to us and for all the sacrifices you had to make because of that!

Big thank you also goes to my grandpa *Zhora* for showing me how to cook and eat traditional Uzbek cuisine, and to my grandpa *Vova* (whom I was calling "denda Vova") for driving us everywhere, playing sports with us and buying us chewing gums with stickers! Grandpa Vova was also the first one to start calling me an "academic" - and what has been a joke in childhood later became a reality! Thank you for always believing in me, Deda!

Special thanks goes to my aunt *Liza*, for whom I was kind of the first kid around and she was taking care of me and playing with me and taking me on all sorts of walks and excursions. Twenty years later nothing has changed, and we're still enjoying spending time together with her and her husband *Vova* whenever I visit Uzbekistan!

My next part of acknowledgements goes to the younger generations of my family. Thanks to my wonderful sisters *Ksusha and Natasha*, with whom we shared all the peculiarities of growing up together, with all the fun and not-so-fun parts of it, but still loving each other and keeping a close relationship even being thousands of kilometers apart! I'm very proud of both of you, my little sisters, and I'm sure you will achieve everything that you want in life!

Big thanks also goes to my cousins *Artem, Sasha and Ilona*, with whom we were sharing our

whole childhood, playing together, going for many adventures (both real and imaginary) and just having fun as it looks like on our old family photos and videos! I hope each of you will also achieve your life goals, and that we continue staying close to each other in the years to come!

Apart from my big family, I would like to thank the wonderful teachers I had at school (actually, at two schools #30 and #33 in Ivanovo, Russia). I was lucky with so many of them, but my special thanks goes to my math teacher, *Ludmila Anatolyevna*, who inspired my interest for mathematics and exact sciences and whom we liked to often visit even after graduating from school, keeping a special relationship with her throughout the years. Thank you, *Ludmila Anatolyevna*, for all your support and wisdom!

Of course, a special paragraph is devoted to the teacher, who influenced me the most and with whom we had countless conversations about life, the Universe and everything. Thanks to him the physics classroom became my 2nd home during the last two years of high school, and physics itself became my 2nd nature during all further studies. Thank you, *Grigoriy Grigorievich*, for helping me find my way in life, for your continuous support on this journey, and for all the unforgettable memories from the last decade!

Recalling the school years I cannot but thank my dear friends from that time *Ilya, Vasya and Borya*, with whom we've been through so many things together! It was amazing to have you all along, guys! And I'm really glad every time we manage to see each other! Hopefully, soon not only online, but also in real life! Two more high school friends continue being part of my life for more than 10 years after graduation *Pasha and Dima*. Thank you so much for staying in touch, guys! I hope to see you soon and to travel together!

Shifting to my university years I would like to thank several of my professors, who were really passionate about their topic and eager to transmit their knowledge to us! First such teacher that I had at MIPT was *Ilya Dedinskiy* (a.k.a "Ded"), who not only showed us the beauty of programming, but also inspired many of us to try water sports, such as rafting and kayaking. I also had several great physics teachers throughout my Bachelor's: *Sergey Zhabin, Alexander Milanich, Lev Melnikovskiy, Leonid Sukhanov, etc.* Thank you for not letting my passion for physics fade away!

During my 3rd year of Bachelor's I was lucky to meet prof. *Alexey Ustinov* and to work in his lab in Moscow. This was my first encounter with the state-of-the-art experimental equipment allowing one to explore the realms of the quantum world! Thanks to him I became a part of the quantum community in Moscow and beyond, also getting to travel for international summer schools and conferences. Moreover, thanks to the wonderful atmosphere of freedom, innovation and solid research traditions, I had a chance to learn and grow as a researcher in a very unique and stimulating environment! It was a truly special time for me and I'm grateful to my colleagues from that time *Kolya Abramov, Vladimir Chichkov, Sasha Averkin*, and, especially, *Kirill Shulga and Sebastian Skacel*, with whom we became real friends!

Thanks to prof. Ustinov I also met my next two professors, with whom I worked during my Master's: *Oleg Astafiev*, with whom I had a chance to see the whole process of building a new experimental lab from scratch, and *Tobias Kippenberg*, thanks to whom I actually learnt about

EPFL. Two great postdocs, whom I would also like to thank are *Ivan Khrapach*, who taught me so many things in life, starting from Amarone wine to microfabrication, and *Alexey Feofanov*, a postdoc in the Kippenberg's lab, without whom my stay in the group would not be as pleasant, if at all possible. Finally, I would like to thank prof. *Vladimir Manko* for his guidance during my Master's and for our common work together, that resulted in my first first-author papers.
My years in Moscow would not have been the same without a great bunch of friends, absolutely marvellous in their variety, with whom we shared so many moments together! It is really hard to name you all on the pages of my thesis, but I want you to know, that you are always in my thoughts!
Two special friends that I cannot but name, are *Andrey and Misha*. With Andrey we became friends during the 1st year of my studies at MIPT, first sharing a dormitory and then even living in the same room together. Andrey stayed a close friend throughout the university years, sharing with me common passions (such as dancing) and being always there to support me during difficult times. On the contrary, with Misha we became friends only at the end of Master's, but shared a common passion for physics and education. Together we were showing the beauty of physics at summer schools, sharing not only teaching duties, but also a common tent. Our crazy friendship continued throughout our PhDs and will hopefully survive the adult post-PhD life.

Turning the page to my PhD years at EPFL, I would first like to thank my supervisor, prof. *Aleksandra Radenovic*, for inviting me on this PhD journey, supporting me all way long and providing everything necessary for my work! Thank you, Aleksandra, for being so patient with me and withstanding all my absences! Thanks a lot for the research freedom, as well as for the freedom to follow my passion for education! I highly appreciate that!

Naturally, I would like to thank my colleagues from LBEN, with whom we worked side by side during these years. I'll start from my office mates (BM 2139):
Lely, for teaching me how to handle cells, for nice everyday conversations and enthusiasm in listening to all my crazy projects! (also huge thanks for letting me use your car and kayak!)
Seb, for also letting me drive his car (with him in it, while I still didn't have my driver's license), and for agreeing to be an IPT juror on Sunday in Geneva in an exchange for ramen!
Ke, for always initiating been time and feeding us with chinese food,
Sanjin, for trying to teach me managing skills and for helping every year with the IPT, but also for hours-long discussions about life and its lessons, tasty Balkan food & quality drinks!
Andrey, for being a great friend and colleague, always ready to help at work, discuss problems, and party together. And for letting me drive his car as well! (feels like I've driven cars of most people in the lab)

Now, my thanks also goes to the people from the neighbouring office:
Hendrik, for sharing with me his microscopy experience in the lab and his life wisdom over a beer or under the Leukerbad sky! Also thanks a lot for helping me to transport that washing machine from Conforama to my place - I was very successfully using it during my whole PhD!

Jiandong, for showing a great example of a successful PhD, for having fun together and cooking nice Chinese food for us!
Michael, for always being an example of a systematic approach to research, a fun beer companion and a devoted member of the "King Hendrik" band! Also huge thanks to you for being brave enough to teach me how to drive! I appreciate it a lot!
Martina, for being the ever-present lab member, for your great initiatives, for bringing people together! Thank you for creating the awesome band and being brave enough to play anywhere anytime! It was a lot of fun being a part of this journey and I'm really sorry that I was such a poor band manager! And, of course, thank you for your epic parties! They were definitely lighting up our PhD lives!
Michal, for driving me to France for shopping, for nice Polish vodka, the smell of good coffee and persistency in research! Thanks for being a valuable collaborator and for all the FIB sessions with changing samples! I hope we will get our Nature!
Mukesh, for always being positive, teaching me how to play volleyball and for loving Gera so much! You were also a great example of the association's president and a real help in organization of all of the events!
Miao, for your calm wisdom, systematic approach to science, sense of humour and positive attitude! I also enjoyed a lot our research discussions and the trip to Goettingen!
Simon, for your amazing bread and other tasty treats that you were so often bringing to the office! I do hope to learn from you someday!
Bart, for your crazy research ideas, ever-present smile and your kindness! It was cool to stay in the lab together till midnight, working side-by-side!

Now, switching to my 5th floor colleagues:
Kristin & Adrien, for being a great example of a super-productive team, passionate about science, knowledgeable and always ready to share your experience!
Arno, for actually trying to teach me optics and answering my never-ending questions about rebuilding my setup!
David, for cool brain experiments and a stylish look!
Arielle, for awesome images of mice's organs, great team spirit, motivation and initiative!
Alessio, for showing an example of great style and a positive attitude!
Jochem, for the Arduino-based toys all over the lab!
Nathan, for being the coolest next generation of PhD students in the lab! You literally brought with you a fresh and young spirit that we are all profiting from! Good luck for your PhD years!
And, of course, *Vytautas*, for co-authoring most of my papers, being my conference/summer school buddy, all the crazy adventures we had, and countless other things that we shared! Without you my PhD life would definitely be much less fun! And thank you for your awesome pictures from so many occasions! These are definitely great memories to keep!
Naturally, I would also like to thank people from the neighbouring labs/offices - great colleagues from LANES, LBNC, LBNI, Q-Lab, K-Lab, LQNO, etc. It was a real pleasure working with so many of you! Same goes to my collaborators from other universities, in particular, from Fribourg, Sydney, Mainz and Ulm.

Instrumental for most of my work was as well the help from the CMI staff! I would like to especially thank *Zdenek, Patrick, Giancarlo, Joffrey, Guy, Remy and Cyrille*! Thank you for teaching me microfabrication and for running the cleanroom so smoothly! I was definitely lucky to use it together with *Dr. Anna Archetti* to fabricate photonic chips for our waveguide project! Anna, thank you for your hard work, inspiration and persistence!
One colleague that I want to thank separately is *Dr. Jean Comtet*, with whom we closely worked on 2D materials. Jean, you were a real example of a young and bright researcher, fully committed to follow his passion for science and capable of literally anything! With time I understand more and more how lucky I was to work with you! And I definitely missed you a lot when you had to go back to Paris, but I'm very glad that you found a position there!

Shifting from work, I cannot but thank many of my Russian-speaking friends at EPFL:
Ivan, with whom we studied together at MIPT and then accidentally met in front of Migros! Your enthusiasm fueled so many cool things, that I was proud to be part of! Thank you for your warm friendship and the opportunity to be part of your life with Monique! Also thanks to you I met your wonderful housemates Mitya, Masha, Sergey and Misha!
Dima Vasiliev, for being an awesome friend, guitar teacher, dog sitter, ski and travel buddy, and just the kindest and most true person I know! Thank you for opening the door of our house so many times, all the glasses of hot and cold beverages, that we drank together, and all the deep and heart-warming conversations that we had!
Asya, Sergey, Katya and Artem, for being a great bunch of friends always ready for new parties and adventures! Fedya, for always entertaining us! Sasha, for your crazy energy, youthful fun and omnipresent smile! And the "Diable-Rabbatable" band for the cool music!
Anton, Misha, Dima, Nastya, Denis - for being awesome housemates in our cozy house in St-Sulpice! Thanks for synchronizing in so many ways our expat life in Switzerland, withstanding and inviting so many great people in our living room, organizing countless parties and celebrations, and always keeping a friendly and welcoming atmosphere in the house!
Alex (Sashulya), my coursemate from MIPT, with whom we only got to know each other after graduating and moving to different countries! Thank you for your frequent visits to St-Sulpice, great sense of humour and style, never-ending conversations about skiing, climbing and kayaking, and the superb opportunities to try all these activities together!
Katya & Stas for their contagious enthusiasm for outdoor sports, especially for being with me in the snowboarding minority! I want to also thank Katya for her support with running AERUS, and Stas for introducing me to piloting drones!
Julia and Dasha, for our IPT-inspired common educational trajectory, friendship over the years and distance, and shared knowledge and PhD experience from various countries!
IPT or International Physicists' Tournament played a huge role in my PhD life at EPFL as well. I not only became the team leader of the EPFL team, but also the Swiss representative and the head organizer of the IPT 2019. For this tremendous experience I would like to thank all the EPFL IPT team members, administration of the Physics Section, LOC and IOC members and many volunteers! I especially want to thank *Alexia* and *Jean-Philippe* for their immense organizational help and the amazing team spirit that we shared!

From the first days of my PhD I was also surrounded by four guys, whom I met at the Welcome Day, organized by EPFL. *KD, Patrick, Rada and Andre* formed the apero/opera lovers group, whose goal was not to miss any occasions to culturally celebrate together! And even though KD left us after 1st year, the four of us managed to stay close (I'm still impressed by that) and enjoyed many activities together. Love you, guys! Next apero is at my place!
My life at EPFL was also enriched by several student associations, especially *ArchiTango* and *AERUS*, which became an integral part of me over the course of my PhD years. I'm very grateful to *Joel* for being my first real tango teacher and for transmitting to me part of his passion for Argentinian tango! Merci infinimment, Joel! And my dream of having an official association of Russian-speaking students was brought to life together with Ivan and Dima, whom I want to thank for pushing me towards this goal!
Of course, my life in Switzerland was not limited to the EPFL campus (even though I spent their a significant share of it). I had a chance to meet many wonderful people all around this beautiful country! I want to thank *Olya, Mara, Kim and Marco* for their support, friendship, and hospitality! Marco, thanks to you the region of Chateaux-d'Oex is in my heart forever!

Finally, my biggest thanks goes to two special people, whom I was incredibly lucky to meet on my way. It is impossible to express in words the influence that both of you had on my life, but I will still try! *Nasya*, thank you for giving me courage to start this crazy PhD journey and for all the unforgettable memories associated with it! Thanks for helping me bring Gera to Switzerland and for being next to her till her last moments here. I cannot imagine this journey without you, as you helped me at every step along the way and made it a truly unique one!

Caro, thank you for coming to my life at the moment of need and giving me strength and motivation to finish this 5-year-long roller-coaster ride! Thank you for your immense care, cuteness, sweetness and puppiness! Thank you for reminding me that I'm not that old yet, and showing me the bright side every time when I was feeling down, and pointing towards an amazing future ahead! I'm also incredibly thankful to all your big and wonderful family for accepting me so quickly and easily, and really making me feel welcome in Switzerland! I definitely learned and experienced much more about Switzerland thanks to all of you!

Writing these acknowledgments made me feel blessed for all the wonderful people I had or still have in my life! Huge thanks to each and every one of you, even I somehow forgot to mention your name here (I'm truly sorry and ashamed for that)! Thank you for being a part of my PhD story or preparing me for it. You helped me become a person I am now!
As you probably guessed from the first page of this thesis, I dedicate it and my whole PhD work to my dog *Gera*, fluffy and playful German shepherd, my first and long-awaited pet, that grew together with me trough high school and university years. You taught me so many things, but most of all the real value of love and loss. Thank you for being such a great life companion! I miss you immensely and I hope you are proud of me up there!

St-Sulpice, 25 June 2021 Evgenii Glushkov

Abstract

Defects in solid-state systems can be both detrimental, deteriorating the quality of materials, or desired, thanks to the novel functionality they bring. Optically active point defects, producing fluorescent light, are a great example of the latter. Naturally existing in various materials, of which the so-called wide-bandgap materials constitute a major part, they can be used as sensors, single-photon emitters or even quantum bits. As the defects preferentially absorb only specific wavelengths of light, the whole material can acquire a visible macroscopic color, becoming the more intense the more there are defects in its lattice. Due to this fact such defects are commonly referred to as "color centers".

The most famous example of color centers is the nitrogen-vacancy (NV) center in diamond, consisting of a nitrogen atom that substitutes carbon next to a vacancy (a missing carbon atom) in the diamond lattice. From the 1990s NV centers have been at the forefront of the second quantum revolution, enabling countless experimental demonstrations of quantum phenomena, even at room temperature. Being currently widely used everywhere from secured telecommunication networks to living cells, diamond NV centers have sparked a persistent interest into novel fluorescent defects, both in diamond (e.g. silicon-, germanium- and tin-vacancy centers) and in other wide-bandgap materials.

Very recently a novel class of material platforms hosting fluorescent defects has emerged – namely layered van der Waals (vdW) materials, which can be thinned down to an ultimate single-atom thickness, opening the door into the realm of two dimensional (2D) materials. This area of research has virtually exploded after the discovery of graphene in 2004, followed by continuous reports of the superb mechanical, electrical and optical properties of graphene-based devices. The whole family of graphene-like vdW materials was rapidly and continuously expanding with new members (graphene oxide, fluorographene, borophene, transition-metal dichalcogenides (TMDCs), layered perovskites, etc.), each of which was enabling various functionalities. Thus, on-demand engineering of materials with desired properties has become a reality in the form of vdW heterostructures.

This thesis explores the properties of newly discovered color centers in a layered vdW wide-bandgap semiconductor - hexagonal boron nitride (hBN). These optically-active defects have shown themselves as exceptionally bright single-photon emitters (SPEs) with a tunable emission wavelength, promising facile integration into nanophotonic circuits thanks to the 2D

nature of the material. Moreover, the recently discovered optically-addressable spin defects in hBN hold a great promise for quantum sensing and quantum information processing.
In the current work I have shown how optical super-resolution techniques (specifically, the single-molecule localization microscopy, SMLM) can be useful to study the properties of emitters in hBN, including their spectra and temporal dynamics. By engineering a specialized waveguide-based imaging platform I managed to overcome certain limitations of SMLM-based imaging, in particular the small field-of-view (FOV) and non-uniformity of illumination. I have further showed how the very same imaging platform can be used for the nanophotonic on-chip integration of hBN via direct growth.
In addition, I have also explored the behaviour of hBN defects in aqueous solutions and how there they can be used as nanoscale charge sensors, tracking the diffusion of single protons. Finally, I developed a novel method for the deterministic engineering of optically-active defects in hBN via focused ion beam (FIB) irradiation and water-assisted etching. All together these findings pave the way for the further use of optically-active defects in hBN for applications in nanophotonics, nanofluidics and quantum sensing.

Key words: van der Waals materials, hexagonal boron nitride, hBN, 2D materials, optically active defects, quantum emitters, fluorescence microscopy, SMLM

Résumé

Les défauts dans les systèmes à l'état solide peuvent être à la fois défavorables, en détériorant la qualité des matériaux, ou souhaités, grâce à la nouvelle fonctionnalité qu'ils apportent. Les défauts ponctuels optiquement actifs, qui produisent de la lumière fluorescente, sont un excellent exemple de ce dernier cas. Existant naturellement dans divers matériaux, dont les matériaux à large bande interdite constituent la majeure partie, ils peuvent être utilisés comme capteurs, émetteurs de photons uniques ou même comme des bits quantiques. Puisque les défauts n'absorbent préférentiellement que des longueurs d'onde spécifiques de la lumière, le matériau entier peut acquérir une couleur macroscopiquement visible, d'autant plus intense qu'il y a de défauts dans son réseau cristallin. De ce fait, ces défauts sont fréquemment appelés "centres de couleur".

L'exemple le plus célèbre de centre de couleur est le centre azote-lacune (NV) du diamant, qui consiste en un atome d'azote qui remplace le carbone adjacent à une lacune (un atome de carbone manquant) dans le réseau cristallin du diamant. Depuis les années 1990, les centres NV ont été à l'avant-garde de la deuxième révolution quantique, permettant d'innombrables démonstrations expérimentales de phénomènes quantiques, même à température ambiante. Actuellement largement utilisés partout, des réseaux de télécommunication sécurisés aux cellules vivantes, les centres NV du diamant ont stimulé un intérêt persistant pour les nouveaux défauts fluorescents, tant dans le diamant (par exemple, les centres NV du silicium, du germanium et de l'étain) que dans d'autres matériaux à large bande interdite.

Très récemment, une nouvelle catégorie de plateformes matérielles hébergeant des défauts fluorescents est apparue - les matériaux stratifiés de van der Waals (vdW), qui peuvent être amincis jusqu'à une épaisseur ultime d'un seul atome, ouvrant ainsi la porte au domaine des matériaux bidimensionnels (2D). Ce domaine de recherche a littéralement explosé après la découverte du graphène en 2004, suivie de rapports continus sur les superbes propriétés mécaniques, électriques et optiques des dispositifs à base de graphène. La famille entière des matériaux vdW de type graphène s'est rapidement et continuellement élargie avec de nouveaux membres (oxyde de graphène, fluorographène, borophène, dichalcogénures de métaux de transition (TMDC), pérovskites en couches, etc.) Ainsi, l'ingénierie sur demande de matériaux aux propriétés souhaitées est devenue une réalité sous la forme d'hétérostructures vdW.

Cette thèse explore les propriétés de centres de couleur récemment découverts dans un semi-conducteur vdW à large bande interdite - le nitrure de bore hexagonal (hBN). Ces défauts optiquement actifs se sont présentés comme des émetteurs de photons uniques (SPEs) exceptionnellement brillants avec une longueur d'onde d'émission modulable, promettant une intégration facile dans les circuits nanophotoniques grâce à la nature 2D du matériau. De plus, les défauts de spin optiquement adressables récemment découverts dans le hBN sont très prometteurs pour la détection quantique et le traitement de l'information quantique.
Dans ce travail, j'ai démontré la façon dont les techniques de super-résolution optique (spécifiquement, la microscopie de localisation à molécule unique, SMLM) peuvent être utiles pour étudier les propriétés des émetteurs dans le hBN, y compris leurs spectres et leur dynamique temporelle. En concevant une plateforme d'imagerie spécialisée basée sur un guide d'ondes, j'ai réussi à surmonter certaines limitations de l'imagerie basée sur la SMLM, en particulier le champ de vision (FOV) limité et la non-uniformité de l'illumination. J'ai également démontré comment cette même plateforme d'imagerie peut être utilisée pour l'intégration nanophotonique sur puce de hBN par dépôt chimique direct.
De plus, j'ai exploré le comportement des défauts du hBN en solution aqueuse et leur utilisation en tant que capteurs de charge à l'échelle nanométrique, en traquant la diffusion de protons uniques. Enfin, j'ai développé une nouvelle méthode d'ingénierie déterministe des défauts optiquement actifs dans le hBN par irradiation au moyen d' une sonde ionique focalisée (FIB) et gravure à base d'eau. Tous ces résultats ouvrent la voie à une utilisation plus poussée des défauts optiquement actifs dans le hBN pour des applications en nanophotonique, nanofluidique et détection quantique.

Mots clefs : matériaux de van der Waals, nitrure de bore hexagonal, hBN, défauts optiquement actifs, émetteurs quantiques, microscopie à fluorescence, SMLM

Contents

List of Figures

1 Introduction and thesis outline

"There's Plenty of Room at the Bottom: An Invitation to Enter a New Field of Physics" - this was the title of a lecture given by the famous physicist Richard Feynman at the American Physical Society meeting more than 60 years ago. Feynman, who is continuously inspiring new generations of scientists (including myself) managed to perfectly summarize in one phrase the impressive progress that the field of micro- and nanotechnology has seen in the last half a century. Current abilities to manipulate matter at the level of single atoms and molecules open up countless opportunities and applications.

Interestingly enough, much of this progress was driven by the rapidly developing semiconductor industry, whose products are being used everywhere around us - from medical equipment, to all sorts of gadgets, to cars and airplanes, to data centers that enable the Internet to function. Powered by billions of tiny chips, they are able to process enormous amounts of information in a fraction of a second, shaping the reality of the world we live in. It is the wonder of miniaturizing the working units of these devices, called transistors, that enabled all the variety of applications. Starting from a rather bulky palm-sized device with outer dimensions exceeding several centimeters, scientists and engineers brought the dimensions of transistors down to single nanometers, bridging the scale gap of over 10'000'000 times. This number becomes even more impressive taking into account that currently tens of billions of such nanometer-sized transistors are working together on a small nail-sized chip [1–3].

The micro- and nanofabrication tools that were developed and perfectionized during this half-a-century long quest are not only essential for semiconductor industry, but have found countless other applications. Currently, many of them are being used in the state-of-the-art research facilities, enabling the work of millions of scientists and engineers. These tools typically include photo- and electron-beam lithography systems, ion- and plasma etching machines, thin film evaporators and a myriad of inspection and characterization instruments.

Among these, optical, electron and atomic-force microscopes are playing a central part allowing us to actually see the nanoscale objects being created. Over decades each of these techniques has found specific use cases, based on its advantages, requirements and limita-

tions, and nowadays they are often used together complementing each other and highlighting various aspects of the inspected samples (so-called, "correlative microscopy"). For example, optical microscope can provide you with a quick overview of your sample, which you can then inspect at specific locations with a scanning electron microscope (SEM) to better resolve the nanoscale features or with an atomic force microscope (AFM) to understand the morphology of the surface.

The first to appear historically, the simplest to use and the most widely spread at the moment is, of course, optical microscopy (also called "light microscopy). Starting from the first experiments with lenses and mirrors in the Ancient Greece and in the Arab world, first light microscopes were developed at the end of the Middle Ages by European craftsmen and scientists, including the famous physicists Galileo Galilei and Robert Hooke. Building up on these first inventions, optical microscopes were greatly improved in the 19th century thanks to the major advancements in the fabrication of glass, which is the most common material for optical components. A particularly important contribution to this field has been done by a group of talented German scientists and engineers from Jena, including Carl Zeiss, Otto Schott and Ernst Abbe.

Collaborating with the optical workshop of Zeiss, Abbe developed the theoretical basis of designing light microscopes, laying the foundation for their industrial-scale production. Abbe is also know for formally defining the resolving power of optical microscopy. The corresponding distance at which objects cannot be resolved by a light microscope is called the Abbe limit and, depending on the wavelength of light used, is typically lying within the range of several hundreds of nanometers. This limit is not due to the imperfection of the microscope or its components, but due to the fundamental property of light to diffract at length scales smaller than its wavelength.

Being detrimental for the exploration of the tiniest details of the nanoworld, diffraction nevertheless allows one to see in the optical microscope even the tiniest sources of light - down to the single atoms. These light emitters are generally called point sources and can be represented by any light-producing objects much smaller than the wavelength of light. The process that allows light to be generated at such scale is called luminescence, and can originate from multiple factors, ranging from chemical reactions, to electrical stimulation to external illumination. The latter one is called photoluminescence (PL) and typically refers to the absorption of high-energy photons with a short wavelength and a consequtive re-emission of lower-energy photons at a longer wavelength. Depending on the timescale of the process photoluminescence is further divided into fluorescence (shorter timescale, quicker process) and phosphorescence (longer timescale, slower process). You can probably remember those star-shaped stickers on the ceiling that glow with a yellow-green color at night (especially, after a sunny day), which is phosphorescence at play.

Fluorescence can be as well observed in everyday life, both in minerals that glow under a UV lamp and in living organisms, such as corals and jellyfish. Moreover, fluorescent proteins,

extracted from jellyfish and optimized in the lab, have forever changed how microscopy of biological samples is performed. Together with fluorescent dyes that have been used to label biological tissues from the beginning of the 20th century, they are at the core of fluorescence microscopy - a powerful technique that forms the image of an object using not the reflected light from an external source, but the light emitted by the nanoscale objects themselves. Such fluorescent probes can be either produced in a living organism (fluorescent proteins) or be attached (fluorescent dyes, nanoparticles) to the objects-of-interest via molecular interactions (chemical bonding, antibodies, etc.).

Such point emitters of fluorescent light also exist in various materials, of which so-called wide-bandgap materials constitute an important class. While being optically transparent for the visible light due to their large bandgap, these materials often contain certain defects in their atomic lattice, which become the source of fluorescence. As the defects preferentially absorb only specific wavelengths of light, the whole material acquires a macroscopic color tint, which becomes the more intense the more there are defects in the lattice. Due to this fact such defects are commonly referred to as "color centers".

This thesis explores the properties of such color centers in a novel wide-bandgap semiconductor - hexagonal boron nitride (hBN), which belongs to a class of van-der-Waals (vdW) materials. The name comes from the fact that adjacent layers of atoms in these crystals are held together by van-der-Waals forces and can be relatively easily thinned down by the consequtive removal of layers (e.g. using skotch tape) to the single-atom thickness, producing a two dimensional (2D) material. The most famous member of the vdW family is graphene, for the discovery of which a Nobel Prize in Physics was awarded to Andre Geim and Konstantin Novoselov in 2010. There are many more vdW materials that are receiving substantial attention nowadays, e.g. transition-metal dichalcogenides (TMDs), phosphorene, layered perovskites, etc., which are finding numerous applications in novel optoelectronic devices.

In the following chapters of the thesis I describe the abovementioned topics in more detail. In **Chapter 2** I give a brief overview of existing and developing material platforms hosting optically active defects, with a special emphasis on hBN. Then in **Chapters 3 & 4** I show how super-resolution techniques can be useful to study the optical properties of emitters in hBN (with a focus on localization microscopy), including their spectra and temporal dynamics. In **Chapter 5** I show how single-molecule localization microscopy (SMLM) can benefit from a specialized waveguide-based on-chip imaging platform, greatly improving the field-of-view and illumination uniformity. In the same chapter I also show how this platform can be used for the integration of hBN emitters with waveguides via direct growth. In **Chapter 6** I accentuate the behaviour of hBN defects in aqueous solutions and how their intermittent ON-OFF switching can be used to track the diffusion of single protons at liquid-solid interfaces. Finally, in **Chapter 7** I show a novel method for the deterministic engineering of optically-active defects in hBN via focused ion beam (FIB) irradiation and water-assisted etching. A short conclusion of the current work as well as a brief outlook of the possible research directions in future are presented in **Chapter 8**.

2 A quest for wide-bandgap materials hosting optically active defects

All existing materials can be in principle divided into three large groups based on how they conduct electric current: metals, semiconductors and insulators. Metals are extremely good carriers of electricity with electrical conductivity of up to $10^8\ \Omega^{-1}cm^{-1}$, typical examples of which are well-known materials like aluminum, copper and steel. Insulators, on the other hand, almost do not conduct any electric current, creating a very high resistance from GOhms and higher, which corresponds to the conductivity of $10^{-8}\ \Omega^{-1}cm^{-1}$ and lower. Semiconductors are taking the place in-between, spanning the approximate range of conductivities from $10^{-7}\ \Omega^{-1}cm^{-1}$ to $10^3\ \Omega^{-1}cm^{-1}$ [4, 5].

These differences can be described by the band theory describing the valence and conduction bands that are unique for each material and can be calculated from first principles. The key term here is that of a "bandgap", which refers to the minimal distance between the valence and conduction bands on a band diagram (see Fig. 2.1) . In other words, bandgap signifies the minimum amount of energy that the system has to receive in order for the electron to be able to jump from the valence to the conduction band. Bandgap is usually measured in electron-volts (eV) and for conventional semiconductors lies within the 0.5-1.5 eV range, which gives them a non-zero conductivity at room temperature and the ability to be switched ON and OFF by applying an external bias (physical basis for the functioning of transistors!).

Insulators, on the other hand, are known not to conduct electricity at room temperature due to the large separation between their valence and conduction bands. Nevertheless, electrical conductivity can be achieved in these materials by increasing their temperature (or by other means that will be discussed below). That is why these materials are also often called wide-bandgap semiconductors, having a typical bandgap value of 4-6 eV. Well-known members of this class of materials are diamond, quartz, silicon carbide, zinc oxide, etc. [6–8]

Bandgap of semiconductors can also be tuned by the addition of various dopants to the pure host material. Depending on which elements are used for doping, they can effectively shift either the conduction or the valence band of the material, thus reducing its bandgap. Typical dopants for conventional semiconductors include phosphorus, arsenic, boron, indium

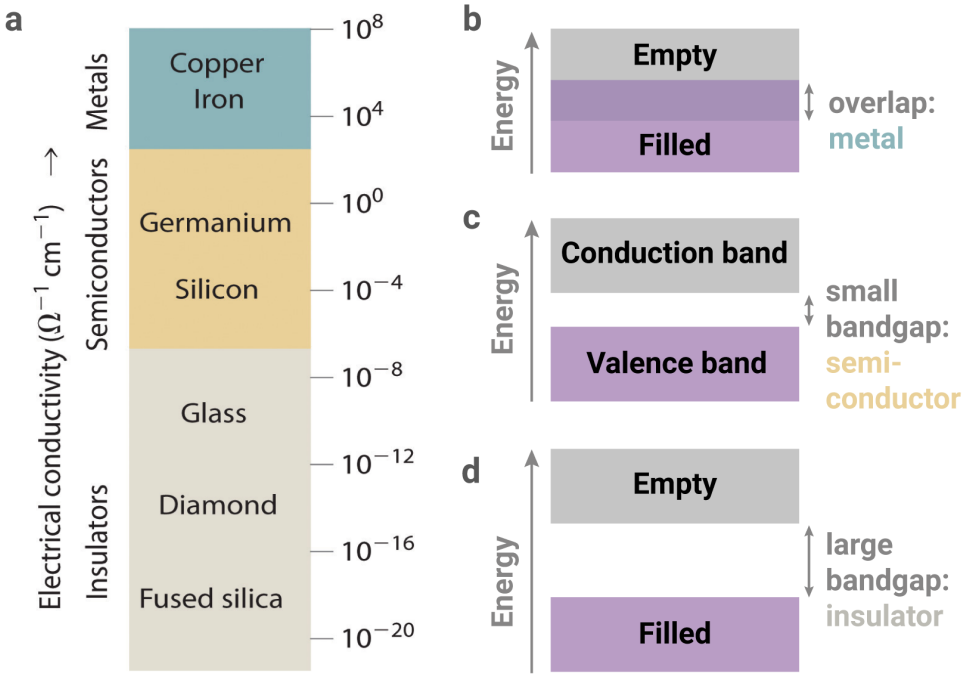

Figure 2.1 – Electrical conductivity of various materials (a) and schematic representation of their band structure (b-d). Adapted from Ref. [5].

and gallium [9], but many other elements can be used for more exotic semiconductors and applications [10].

In reality, the effects of doping are far more complex than just a simple shift of the bands. What the implanted atoms do is they introduce the so-called intra-bandgap defect states within the bandgap of the host material [11, 12]. Transitions between these states can be induced via thermal fluctuations (requiring much lower temperature), or by supplying external energy (e.g. via photons or phonons). These transitions can occur not only within the intra-bandgap states, but also lead to the consecutive population transfer from the valence to the conduction band [13].

A common way of achieving a controllable excitation of electrons from one band to another is to illuminate the material with light of certain energy/wavelength, that should approximately match the energy difference between the ground and excited states. Absorption of such light waves leads to the creation of propagating electron-hole pairs (also called excitons), which can later recombine and emit another photon, typically of a lower energy. This gives rise to photoluminescence that can be observed when illuminating wide-bandgap semiconductors with UV light of a sufficiently short wavelength ($\approx$ 200 nm) [14].

Consequently, light of a longer wavelength can be used to induce transitions between the intra-bandgap evergy levels (Fig. 2.2), while not altering the population transfer between the valence and the conduction bands. Well hidden within the large bandgap of a host material,

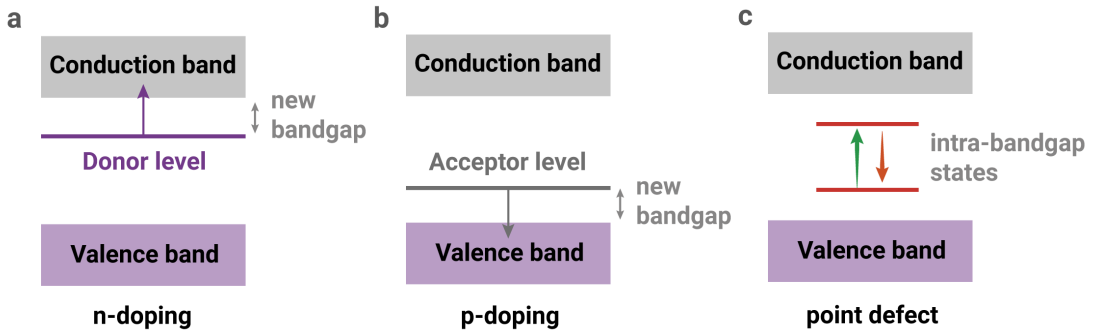

Figure 2.2 – Schematic bandgap structure of doped semiconductors: (a) n-doped, (b) p-doped; and (c) point defects, creating sub-levels within the bandgap, which often can be optically addressed. Adapted from Ref. [5].

these optically addressable energy states of point defects – previously mentioned as "color centers" – become a valuable resource for quantum technologies. They can be used as single-photon emitters [6, 15, 16], quantum sensors [17–19], quantum memories [20, 21], and even to process quantum information [22]. Some of the most common types of existing color centers are described in the following sections 2.1, 2.2, and a more complete overview can be found elsewhere [23, 24].

2.1 Color centers in diamond

Diamond has a cubic crystalline structure (C_{3v} symmetry) with an extremely high density ($1.77 \times 10^{23} cm^{-1}$) and high Debye temperature (2240 K), which makes the diamond lattice an ideal host for hundreds of stable crystallographic defects [23, 25]. Many of these defects produce bright, continuous and non-blinking fluorescence in the visible and near-infrared range (2.3a,b).

For example, the nitrogen-vacancy center, which is most commonly found in natural diamonds due to abundance of nitrogen in the atmosphere, makes the host diamond crystal appear yellowish (2.3a). It is also the best studied diamond color center [26], which has been used to sense various physical quantities (magnetic [17] and electric [27] fields, pH [28], strain [29], pressure [30] and temperature [18, 31]) by utilizing its unique energy-level structure providing an optically-detected magnetic resonance (ODMR) [32].

To understand what ODMR is, one should look at the energy-level structure of the NV^- center. A simplified diagram in Fig. 2.3c shows a ground and an excited state (both triplets with radiative transitions between them), separated by 1.945 eV, and a singlet meta-stable state through which the system can experience a non-radiative transition [33]. At room temperature the sub-levels of both ground and excited states (having different spin projections $m_s = 0, \pm 1$) are non-degenerate, which makes the transitions between them possible (typically, in the microwave range). Although the optical transitions from the ground to the excited state

conserves the spin projection, the rate of transitions to the metastable state is much higher for the excited state with $m_s = \pm 1$ than for $m_s = 0$, so the system will mostly relax to the ground state without emitting a photon. Normally, both sub-levels are equally-populated, but if one applies a constant microwave signal at the transition frequency between them, this makes the $m_s = \pm 1$ states more populated (producing so-called spin polarization). More transitions therefore occur non-radiatively and fewer photons are detected as the fluorescent signal. Scanning the frequency of the microwaves around the transition, produces the ODMR dip shown in Fig. 2.3d, when the frequency of the microwave signal matches the transition energy between the spin sub-levels. The maximum achievable ODMR contrast is estimated to be around 22% [34–36].

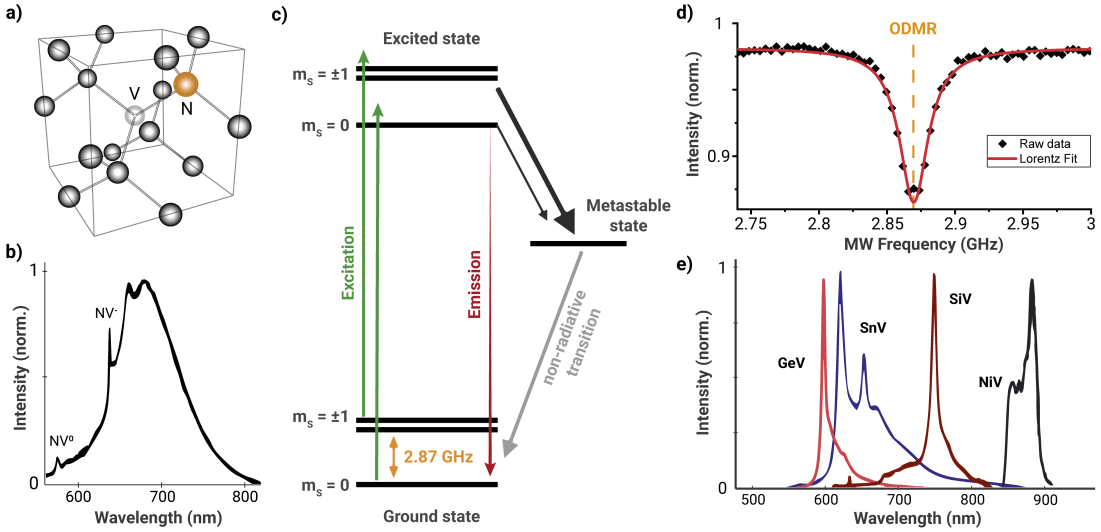

Figure 2.3 – Crystallographic structure (a) and a typical emission spectrum of nitrogen-vacancy center (b) with distinct peaks of diffferent charge states of this defect: NV^0 and NV^-. c) Simplified energy-level structure of NV^- center and d) an example of a recorded ODMR from fluorescent nanodiamonds, fitted with a Lorentzian. e) Spectra of some other emerging color centers in diamond. Adapted from Ref. [37].

In recent years more and more experimentally-produced diamond defects were recognized as prominent emitters for quantum technologies: silicon- [38], germanium- [39], tin- [40] and nickel-vacancy [41] centers. Their emission spectra are shown in Fig. 2.3e, spanning most of the visible to near-infrared spectral range. Owing to their different energy-level structure, each of the color centers is better suited for specific applications (e.g. quantum sensing [17, 19, 27, 28], single-photon emission [42, 43], labeling [44]). However, their production is still challenging and has to be sufficiently upscaled before they can become a widely-used sensing tool (which is already the case for commercially-available bulk single-crystal diamonds, poly-crystalline diamond films and nanodiamonds with NV-centers [45]).

2.2 Color centers in silicon carbide and zinc oxide

While bulk diamond might be shielding well its color centers from the environment, it is far from being easy to grow and process. Therefore significant efforts are focused on exploring point defects in more technologically available materials, such as silicon carbide (SiC) and zinc oxide (ZnO). Both of these materials are relatively cheap and available in various forms and sizes, up to 6" high-quality wafers [8].

Color centers in both pristine and doped zinc oxide have been reported back in 1992 [46], and several research groups have since then observed single-photon emission from these defects [47–49] (mostly, in nanoparticles). However, the photostability of emitters in ZnO remains an issue and the exact atomic structure of the defect is yet to be confirmed [50]. Up to date no signs of spin-dependent emission from color centers in zinc oxide have been reported as well.

Much better progress has been achieved with color centers in silicon carbide, which has multiple lattice stacking configuration (polytypes) and defect types. Among them one of the most promising are neutrally charged divacancies (VV^0) [51, 52], that have been been studied at the single emitter level [53] making them promising candidates for single-photon sources [54]. Other defect types in silicon carbide have also demonstrated ODMR and long coherence times [55], suitable for quantum sensing applications [56].

2.3 Optically active defects in vdW materials

Very recently a new class of materials has emerged as a promising host platform for optically-active defects – the layered vdW materials. Due to their ability to be thinned down to atomically-thin layers, their application in optoelectronic devices gave a great promise of further miniaturization of components down to the ultimate limit [57, 58]. Moreover, various vdW materials can be stacked together [59, 60], resulting in heterostructures with desired properties (e.g. increased carrier mobility in the hBN-graphene stack (3x vs. graphene on SiO_2) [61, 62], self-cleansing of contamination [63] or even superconducting behaviour [64, 65], and many more [59]).

Much of the recent research efforts in the quest for novel quantum emitters were focused on two members of the vdW material family: transition-metal dichalchogenides (TMDCs) and hexagonal boron nitride (hBN). In 2015 several research groups independently reported single-photon emission from localized defects in tungsten diselenide (WSe_2)[66–70] - a semiconductor with a direct bandgap of 1.7 eV. Emitters in WSe_2 were initially found at the edges of the flakes, along defect lines or in transfer-induced wrinkles and bubbles[66, 71, 72], and later engineered at specific locations using local strain[73, 74]. Similar emitters were also found in other TMDCs, like $MoSe_2$, WS_2 and GaSe [15], however all of them operating only at low temperatures.

2.3.1 Quantum emitters in hexagonal boron nitride

In contrast to TMDCs with a relatively small bandgap (1-2 eV), where light emission originates from 0D localized excitons and can typically be measured only in a cryogenic environment [15], color centers in hBN lie deep within its large bandgap (6 eV) and can be measured at room temperature and above (up to 800 K)[75]. Owing to the wide bandgap, pristine hBN doesn't absorb visible light down to deep-UV[14] and constitutes a transparent crystal, similarly to diamond changing its color depending on the contained impurities [76].

hBN is one of the two main allotropes of boron nitride (the other one being the much harder cubic form, cBN, which is almost as hard as diamond) and is a temperature stable (up to $1600^{\circ}C$ in vacuum) and chemically inert material, with an excellent thermal conductivity (100s of $W \cdot m^{-1}K^{-1}$), a high dielectric constant ($\epsilon \approx 4$) and a low friction coefficient [77, 78]. Thanks to these remarkable properties it is widely used as an industrial lubricant in cosmetics, insulator and heat sink in electronics, transparent window material in optics and as high-quality sealing agent [78, 79].

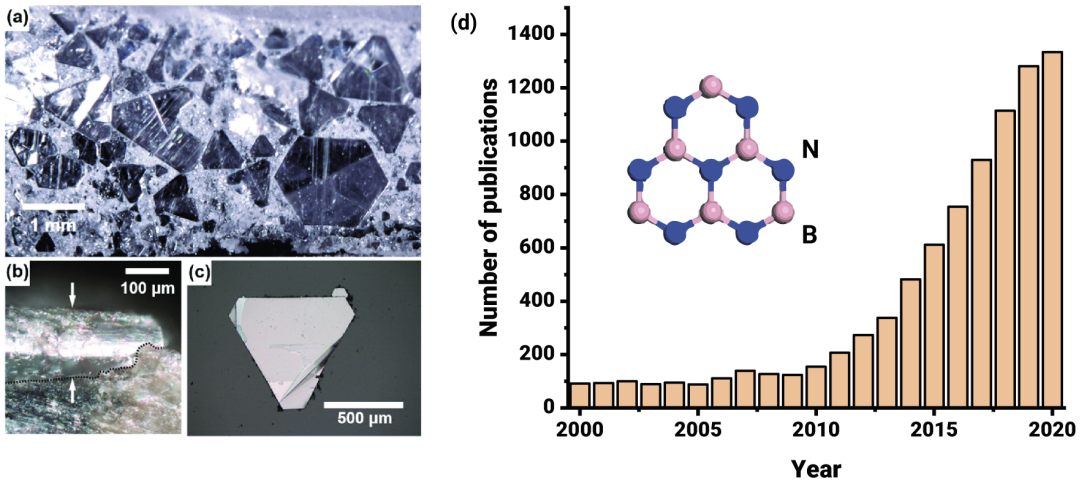

Figure 2.4 – Optical micrograph of (a) hBN crystals on Fe-Cr, (b) side view, and (c) hBN flake transferred onto the substrate-of-interest. Reprinted with permission from Ref. [80] (d) Growth of the popularity of hBN within the scientific community. Source: Web of Science

The rise of hBN as a commonly used substrate in the field of 2D materials came after high-quality hBN crystals were successfully synthesised by Taniguchi and Watanabe [14, 76] and proved to be extremely useful as an underlying layer for graphene-based devices [62] (see the sharp increase in the number of publications mentioning hBN in Fig. 2.4d) . Since then hBN started being widely used in vdW heterostructures [59, 60], both as a bottom and top layer, as well as a thin spacer in various optoelectronic [81, 82] and nanofluidic devices [83, 84]. While the established way of achieving single-crystal hBN films is still its tape-assisted mechanical exfoliation from bulk crystals [60, 85], many more techniques has been developed to either grow and transfer [86–90] or thin down [91] hBN flakes and films. Attempts of directly

growing hBN on the substrates of interest, including photonic chips, are also underway [92–94], however the quality of as-grown material has to still be improved.

The discovery of room-temperature single-photon emitters in hBN was first reported in 2015 by Tran et al. [95] from defects induced in the PMMA-transferred CVD-grown hBN film by high-temperature annealing. Later single-photon emission was measured from sparse defects in bulk single-crystal hBN [96], as well as in exfoliated flakes [97]. Various annealing and irradiation techniques were employed in an attempt to control the emission wavelength of the defects in hBN [98, 99] (see Fig. 2.5), as well as their spatial distribution [97]. While the inspected emitters were usually randomly distributed on hBN flakes with higher occurrence at the edges, defects and wrinkles [100], recent works have shown several approaches to deterministically induce optically-active defects in hBN [93, 101–106]. More in-depth overview of these attempts is given in Chapter 7.

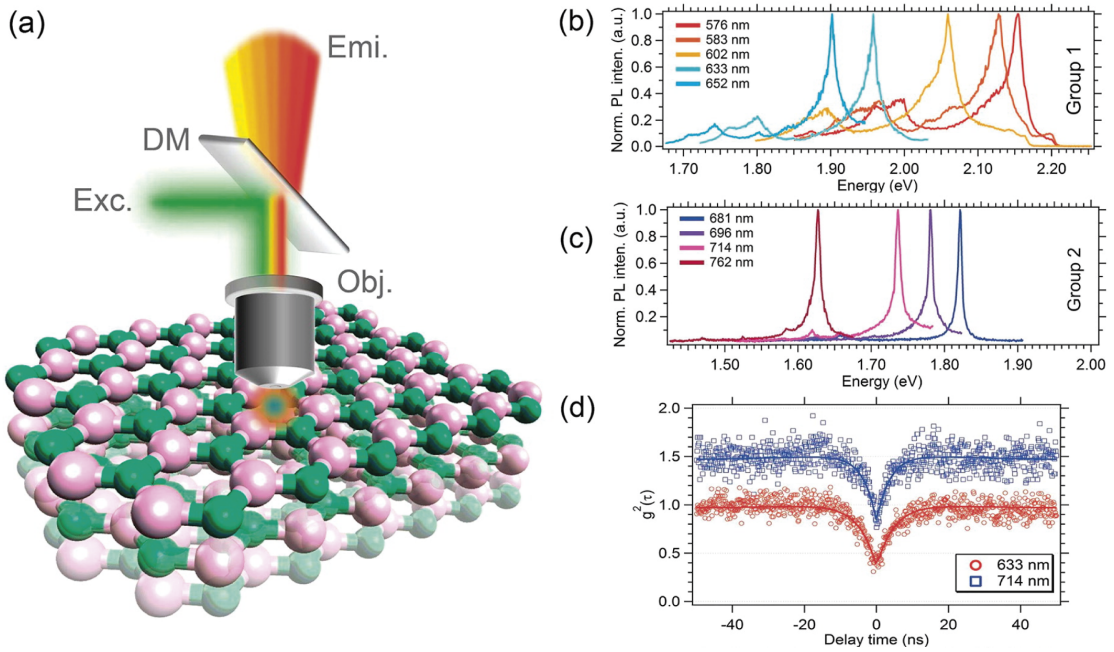

Figure 2.5 – Multicolor quantum emitters in hBN inspected using confocal microscope (a), spectra of shorter- (b) and longer-wavelength (c) emitter types. (d) Second-order autocorrelation functions proving the single-photon nature of the emission ($g_2(0) < 0.5$). Adapted with permission from Ref. [98]

In addition, several groups demonstrated spectral tunability of the emission from hBN defects using either externally applied electric field [107–110] or local strain [111–113]. Optically active hBN defects were also successfully coupled to plasmonic structures [114, 115], optical fibers [116], integrated waveguides [94, 117, 118], ring resonators, grating couplers and photonic crystals [119–121]. Combined with the recent discovery of ODMR in hBN emitters both at cryogenic conditions [122] and at room temperature [104, 123, 124] and the coherent optical control of these emitters [125], they are becoming an increasingly attractive platform for nanophotonics and quantum sensing.

2.3.2 Atomic structure of defects in hBN

What is still not fully understood about optically active defects in hBN is their atomic composition and corresponding energy-level structure [126]. At the moment, at least two defect types with distinct spin properties are experimentally identified with zero-phonon lines (ZPLs) around 600 nm and 830 nm. While the ZPL variation of the first defect type was shown to span the whole range between 550 and 750 nm [98, 127, 128], it initially didn't show any magnetic field dependence and, correspondingly, no ODMR (even though it was measured later at sub-GHz frequencies [113, 122, 124]). On the contrary, the defects emitting closer to 830 nm are exhibiting pronounced ODMR around 3.5 GHz and can therefore be coherently manipulated using optical and microwave excitation [104, 123, 125]. Another defect type has been recently reported with a ZPL around 435-440 nm [105], but the authors didn't comment on its atomic origin.

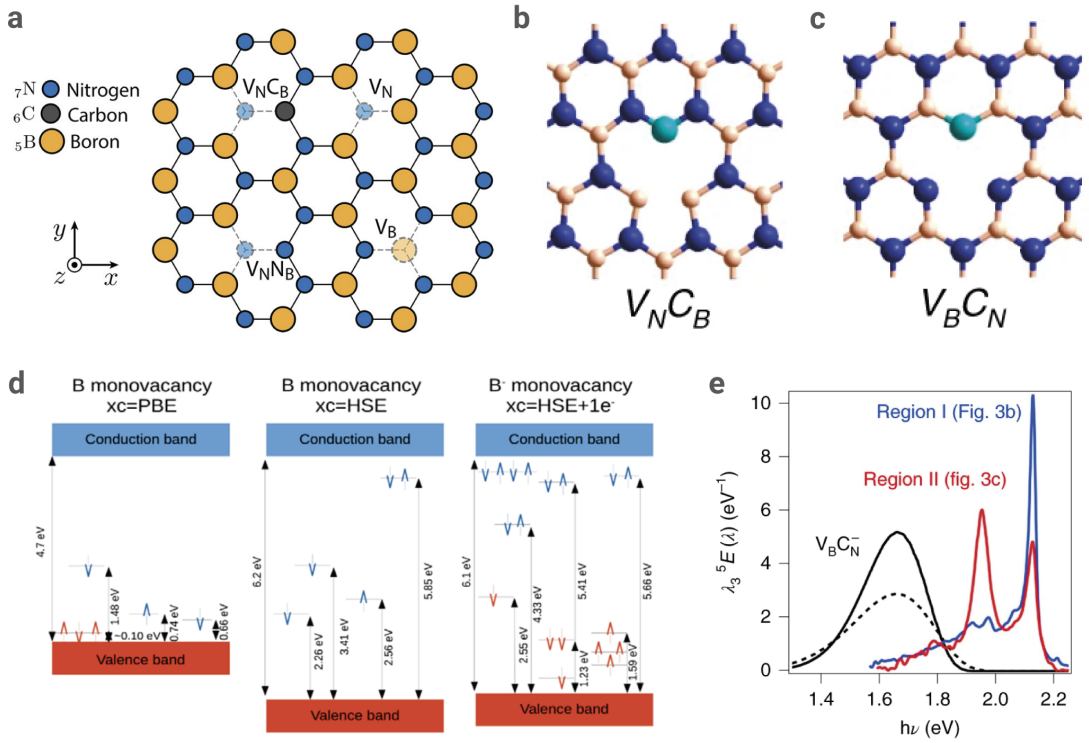

Figure 2.6 – Various possible point defects in the hBN crystal lattice (a), and carbon-related defects (b,c) responsible for the single-photon emission. (d) DFT calculations of the boron monovancies energy states. (e) Comparison of the predicted spectra (black dashed line, basic one-layer model; black solid line, three-layer out-of-plane distorted model) to the observed emission from region I (with implanted carbon defects) and region II (masked during implantation). The predicted spectra are both too low in energy and too broad compared with the experimental ones, clearly demonstrating current state-of-the-art computational uncertainty. Adapted with permission from Refs. [129–131]

First attempts to match experimentally measured spectra with theoretical predictions of the defect structure were made already in the first paper reporting the discovery of SPEs in hBN

[95]. Two potential intrinsic defect types were explored using density-function theory (DFT) calculations: nitrogen vacancy (V_N) and an anti-site complex in which nitrogen occupies the boron site and there is a vacancy at the nitrogen site ($N_B V_N$). The latter was considered as the most likely defect candidate due to it's energy level structure structure, deduced from DFT calculations. Hovewer, the precision of discussed DFT calculations and the multitude of parameters affecting their results, do not currently allow to identify atomic origins of the optically active defects with certainty (see Fig. 2.6), therefore remaining an area of intense debates [130, 131]. For example, the boron vacancy (V_B) was not explored in this study, but later appeared in several publications [127, 129, 130], also in relation to the different charge states of this defect type [129, 132]. Dangling bonds were also proposed as a likely source of the observed emission around 580 nm [133].

Extrinsic defects in hBN have as well been studied using DFT methods, exploring the influence of oxygen, carbon, silicon, sulfur, fluorine and phosphorus on the energy-level structure of corresponding hBN defects [134]. Carbon-antisite defect ($C_B V_N$) seemed to match well the experimentally measured optical spectra, corroborated by other independent studies [135]. Futher confirmation of carbon-based defects in hBN came several years later from experiments with controlled carbon-doped hBN films, grown independently using various methods [113]. This collaborative work has for the first time shown a direct dependence of the density and brightness of SPEs in hBN on carbon concentration during growth. While the ZPLs of the the carbon-related emitters varied depending on the growth method and substrate, such defects had emission spectra in the range from 550 to 750 nm, corresponding to the first defect type mentioned above. Extrinsic carbon-related hBN defects have also shown ODMR in the frequency range of several hundred megahertz, depending on the applied magnetic field [113, 124].

The spin-dependent emission from intrinsic hBN defects has been successfully measured on hBN samples irradiated with accelerated neutrons [136] or focused ion beams [104, 123], resulting in a broad near-IR ZPL, centered around 850 nm. Based on its ODMR and EPR spectra, the most promising candidate for this intrinsic defect type was found to be the negatively charged boron vacancy (V_B^-), a spin S=1 system [137] with a theoretically suggested intersystem crossing [129]. This enables coherent manipulation of such color centers, measurements of their relaxation times and the study of their hyperfine transitions [125]. Moreover, the ability to deterministically create such spin defects at predefined spatial locations [104] makes this system extremely interesting for future applications in integrated nanophotonics.

3 Defects in hBN explored using super-resolution microscopy

Several imaging techniques were demonstrated to be suitable for studying defects in vdW materials at different scales. Transmission electron microscopy (TEM) [138, 139] can be employed to image single defects over an area of several tens of square nanometers with atomic resolution. This process is however often accompanied by the introduction of new defects during imaging (depending on the acceleration voltage) due to intense electron-beam irradiation of the studied sample [139, 140]. However, electron beam can not only induce new defects, but also excite cathodoluminescence of intrinsic ones [141, 142], which allows for in-situ detection of localized fluorescence in TEM and correlative imaging of optically active defects [128].

Near-field techniques, such as scanning tunneling microscopy (STM) [143] and near-field scanning optical microscopy (NSOM/SNOM) [144] have also been successfully applied to study defects in vdW materials [145–147]. While STM can resolve single atoms (and, consequently, point defects), it requires a conductive substrate which quenches the optical signal from the defects. NSOM, on the other hand, works on any substrate, can directly probe the optical response of the material and its defects, but has a coarser resolution of tens of nanometers. Atomic Force Microscopy (AFM) has also proven to be a useful technique to visualise structural defects down to the nanometer level and correlate them with the optoelectronic properties of the material [148]. However, all these techniques are severely limited by the size of the inspected area (typically, several μm^2) and do not allow for high-throughput characterization.

Luckily, many optically active defects in vdW materials can be studied with a versatile far-field optical microscopy, which is a general term for a multitude of various imaging techniques using propagating electromagnetic fields in the optical range (100s of THz). In particular, fluorescence laser-scanning microscopy (LSM) [149–151] has been the workhorse of experimental research on fluorescent defects in solid-state materials[152–154], providing a fast and non-destructive readout of fluorescent emission [35]. Invention of the confocal laser-scanning microscope (CLSM) [155, 156] gave an additional advantage of optical sectioning, thus enabling imaging of isolated defects in bulk materials, nanoparticles and fluorophore solutions [32, 157–159] by rejecting the out-of-plane background signal using a pinhole [160, 161].

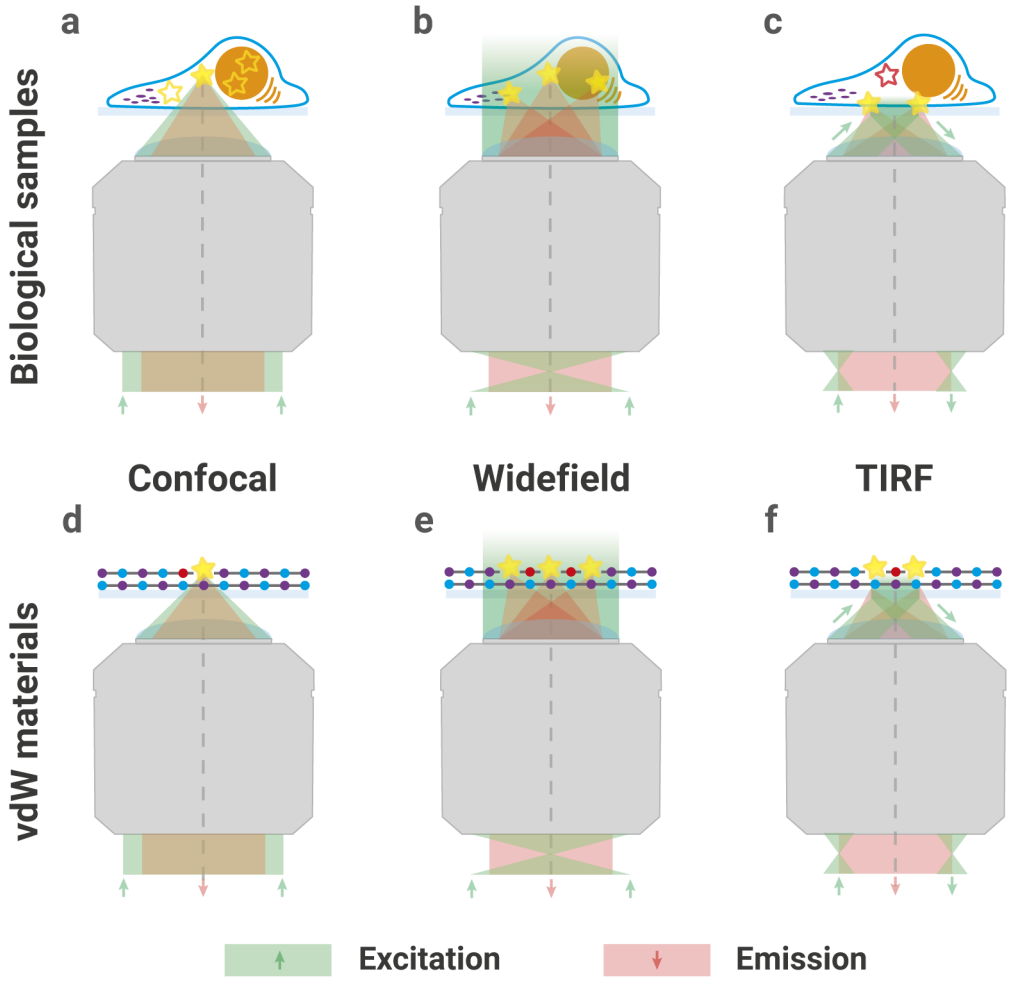

Figure 3.1 – Qualitative comparison of various illumination modalities in optical microscopy. a) Confocal illumination is usually combined with point-by-point scanning and signal acquisition using a single-pixel detector, such as photo-multiplier tubes (PMTs) or avalanche photodiodes (APDs). Sequential excitation of different fluorophores and optical sectioning capabilities allow to record emission from each fluorophore separately and reject out-of-plane signal, which is especially advantageous for imaging thick biological samples. b) Widefield illumination allows for simultaneous excitation and detection of multiple emitters in the field-of-view (FOV) and is typically combined with multi-pixel camera detectors - charge-coupled devices (CCDs) or complementary metal-oxide semiconductor (CMOS) cameras. c) TIRF microscopy employs oblique illumination of the sample, generating exponentially-decaying evanescent waves at the interface, therefore exciting only emitters very close to it (tens of nanometers). This technique also helps avoid fluorescent background from the bulk of a thick sample, as the excitation doesn't reach the fluorophores in the bulk. d-f) Same imaging techniques applied to thin vdW materials. Now widefield illumination doesn't suffer from unwanted background fluorescence and can be advantageous for imaging vdW materials. To further increase the contrast, TIRF modality can be used. Dimensions are not to scale!

While being useful for thicker samples and faster, than the above-mentioned nanoscale techniques, confocal microscopy is still not ideal for high-throughput defect characterization in large-area materials as it is at its core a sequential scanning technique. This is where widefield optical microscopy using camera detectors to image the entire field of view in a single shot comes in handy, particularly for defects exhibiting intermittent ON-OFF switching (blinking), whose characterization cannot be fully done during the confocal scanning (temporal dynamics of the emission cannot be characterized during a single scan). On the contrary, widefield microscopy easily provides access to the statistical distribution of optical properties of large ensembles of emitters, including their spectral and temporal dynamics [127].

The main disadvantage of widefield illumination, causing simultaneous excitation of emitters within the illumination cone and leading to image blur for thick biological samples, is not playing any role for thin vdW materials, with typical thicknesses below 100 nm. Moreover, total internal reflection fluorescence (TIRF) microscopy can be used for a more efficient excitation of emitters in vdW materials, which becomes especially useful once they are immersed in solution. A qualitative comparison of these microscopy techniques is shown in Fig. 3.1. Quantitatively, the comparison of TIRF vs. widefield excitation can be made in terms of signal-to-noise (SNR) and signal-to-background (SBR) increase. For the same hBN flake and same laser power this increase (highly dependant on the flake's thickness) easily reaches 25% for SNR and 100% for SBR, when switching from widefield to TIRF illumination (see Fig. 3.2).

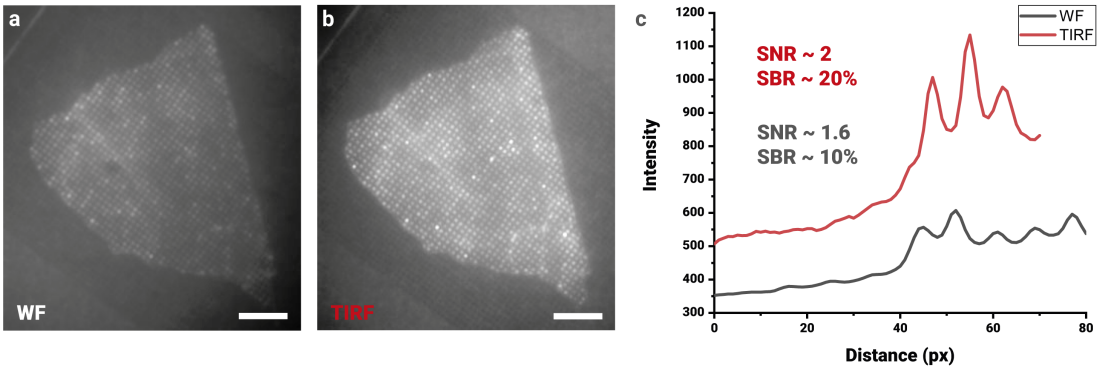

Figure 3.2 – Averaged widefield (a) and TIRF (b) image of the same hBN flake containing optically active defects. Taking line profiles on each of the images (c) one can estimate the SNR and SBR values for both cases.

All optical techniques, however, suffer from one major drawback stemming from the wave nature of light - diffraction, limiting their ability to resolve nanoscale objects. For examples, for optically-active defects, emitting visible light, this limit equals to about 200 nm (laterally) and 500 nm (axially), see Eq. 3.1 and Fig. 3.1. One must note that in principle several resolution criteria exist in literature (see, e.g. Ref. [162], Chapter 12), of which Rayleigh and Abbe limits are the most popular, originating from astronomy and microscopy field, respectively. Even though different resolution criteria slightly vary the exact value of the diffraction limit in each specific case (e.g. coherent vs incoherent illumination), they are still converging to the

above-mentioned values of several hundred nanometers for wavelengths in the spectral range of visible light.

$$d_{x,y} = \frac{\lambda}{2NA} = \frac{\lambda}{2nsin\theta} \quad (lateral) \qquad d_z = \frac{2\lambda}{NA^2} = \frac{2\lambda}{n^2 sin^2\theta} \quad (axial), \tag{3.1}$$

where λ is the wavelength of light used, NA corresponds to the numerical aperture of the lens, n is the refractive index of the working medium, and θ is the maximal half-angle at which light can enter the lens.

The quest to overcome the diffraction limit has been mostly driven by biological applications of fluorescence microscopy, aiming at resolving sub-cellular structures and their functional behaviour[163, 164]. One way to overcome this limit is through the use of near-field methods (SNOM, NSOM) mentioned above, that utilize a sharp probe scanning across the sample to provide resolution down to several nanometers [165–170]. On the contrary, reaching similar resolution in far-field microscopy requires substial efforts, utilizing either non-linear illumination or temporal separation of emission [171]. A brief overview of these methods is given in Section 3.1 with a special emphasis on localisation microscopy techniques, which are mainly employed in this thesis.

3.1 Super-resolution optical microscopy

Before diving into various super-resolution techniques it is important to properly introduce two basic microscopy terms - point-spread function and resolution. They are closely interconnected and applicable to all optical systems, but often overlooked or misunderstood. Sections 3.1.1 and 3.1.2 aim at filling this gap. To go deeper into this subject, please refer to Ref. [172].

3.1.1 Point-spread function (PSF)

Acquiring an image of an infinitely small fluorescent particle or defect for the first time one might be surprised to see that it doesn't form a single bright point on a camera. On the contrary, it shows up as a rather diffuse intensity distribution on the order of half a wavelength of the emitted light, irrespective of the nanometric size of the fluorescent source. This intensity distribution is called a point-spread function (PSF) and is the direct consequence of light diffracting at the circular aperture of the imaging lens (microscope objective). As most of the microscope objectives have a circular aperture the shape of the PSF is generally represented by an Airy pattern, with a bright Airy disc in the middle (Fig. 3.3a).

Even though Sir George Airy himself was a 19th century astronomer, mostly interested in distant stars and telescopes rather than fluorescent emitters and microscopes, his mathematical description of observed concentric ring patterns is still applicable for all optical instruments.

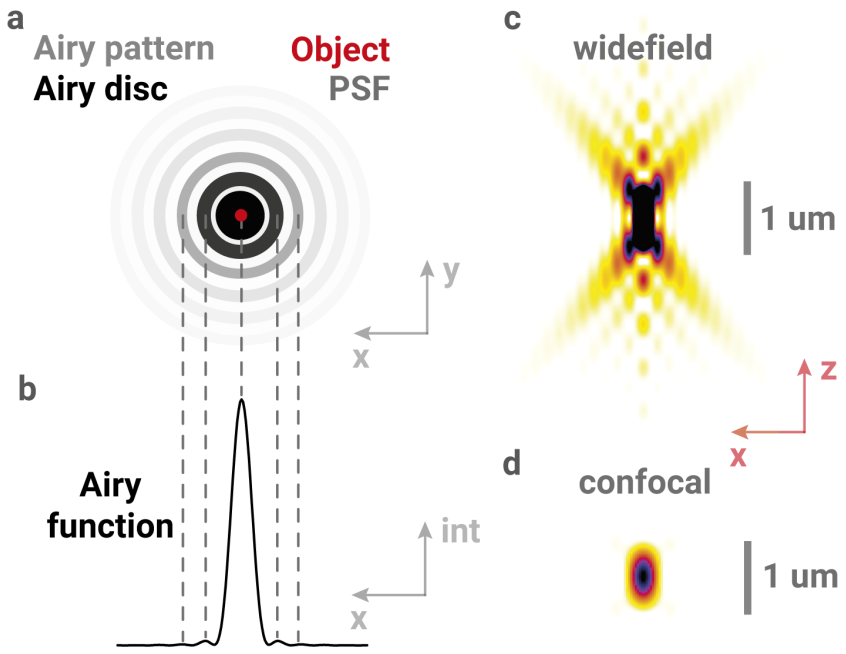

Figure 3.3 – PSF of a point object in XY and XZ planes for both widefield and confocal microscopes. a) Point emitter in the sample plane is seen as an Airy pattern in the image plane (on the camera). b) The intensity profile is an Airy function, which amplitude is defined as $h(v) = 2 \cdot J_1(v)/v$, where $J_1(v)$ is the first-order Bessel function and v is the optical distance, defined as $v = 2\pi \cdot a \cdot r/(\lambda \cdot f)$, where r is the radial distance from the optical axis, a is the radius of the lens, f is its focal length. c) Axial PSF of a widefield microscope, shown in the XZ plane. d) Axial PSF of a confocal microscope, showing an impressive axial PSF reduction, which leads to the optical sectioning capabilities of the confocal microscope. The maximum PSF reduction is achieved with an infinitely small pinhole placed at the focal plane of the tube lens, which also leads to the rejection of most of the fluorescent signal. In practice, the size of the pinhole is chosen as a trade-off between axial resolution and photon counts.

In principle, it is a specific case of a more general Fraunhofer diffraction on a circular aperture (see Chapter 8.1 from Ref. [162] for a more detailed explanation). And the example of Airy shows a deep influence that astronomy had on microscopy, which was historically lagging behind. Another important example of such influence are adaptive optics systems, that were actively used in telescopes to compensate for atmospheric aberrations [173] and then found applications in high-end optical microscopes [174].

PSF of a microscope plays a key role in image formation, be it for a point emitter or for a more complex object that can be represented as a superposition of intensities of multiple point sources. Generally speaking, an image I(x,y) of a certain object O(x,y) in the focal plane of an

optical system with a certain point-spread function PSF(x,y) is represented by a convolution:

$$I(x,y) = O(x,y) \times PSF(x,y), \tag{3.2}$$

Even though the Airy pattern of a PSF is determined by the circular aperture of an objective lens, it can be shaped to have a different intensity distribution (e.g. via a phase mask). PSF shaping can be done both for the detection and for illumination paths of a microscope. First case is implemented in confocal microscopes, while the second plays a key role in structured illumination approaches, which will be discussed in section 3.1.3.

3.1.2 Resolution vs. Localization Precision

It is important to not confuse the term 'resolution' (which typically refers to a two-point metric) with a similar term 'localization precision', which can also be called a one-point resolution [175]. While localization precision defines how well one can determined the position of the point source, resolution gives information about how close two point sources can be to be still resolvable (based on a certain resolution criteria, of which there exist plenty [176]). This difference is especially important in the context of localization microscopy, where localization precision can reach single nanometers and is quite easy to calculate [177, 178], however resolution stays in the tens of nanometers range for most super-resolution techniques and is much trickier to estimate without any prior knowledge [179, 180].

The way that fluorescence microscopy resolution is estimated in practice is using certain nanoscale objects with known dimensions (e.g. from electron microscopy), be it microtubules with fixed diameter of $\approx$ 25 nm [181, 182], DNA-rulers based on DNA origami structures with variable distances between fluorophores depending on their binding sites [183, 184] or other nanoscale rulers. Moreover, resolution can also depend on the sampling of the detection (pixel density) and labeling density in case of fluorescent probes [172]. More in-depth discussion of these effects can be found in Refs. [185, 186].

Having described the basic terms, we can proceed to the discussion of various super-resolution microscopy modalities, which can be divided into two main groups: structured illumination and localization microscopy methods [171, 186–188].

3.1.3 Structured illumination methods

Structured or patterned excitation methods are surpassing the diffraction limit by introducing certain sub-diffraction-limited features into the illumination pattern. The first method of this kind proposed theoretically in 1994 and implemented in 1999 was the STimulation Emission Depletion (STED) microscopy [189, 190]. This approach utilized a second laser to suppress the

fluorescent signal, originating from the circumference of the excitation spot, by matching the resonant energy of the transition between the excited and ground states and thereby causing stimulated emission of photons.

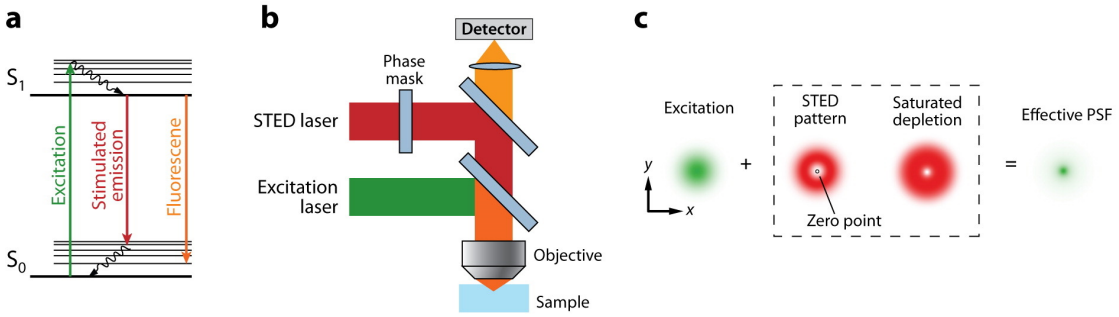

Figure 3.4 – STimulated Emission Depletion (STED) microscopy. (a) The process of stimulated emission. A fluorophore in the ground state can absorb a photon and transition to the excited state. Spontaneous fluorescence emission brings the fluorophore back to the ground state. Stimulated emission happens when the excited-state fluorophore encounters another photon with a wavelength comparable to the energy difference between the ground and excited state. (b) Schematic of a STED microscope. The excitation laser and STED laser are combined and focused on the sample. A phase mask is placed in the light path of the STED laser to create a donut-shaped pattern in the sample plane. (c) A donut-shaped STED laser is overlapped with the excitation laser. Due to saturated depletion, fluorescence from everywhere except for the zero point is suppressed, leading to a decreased size of the effective PSF. Figure reprinted with permission from Ref. [171].

To achieve the sharpening of the excitation PSF the STED laser is sent trough a phase mask, which results in a donut-shape PSF in the focal plane. Even though this process is also governed my diffraction, the nonlinear dependency of the depleted population of molecules on the power of the STED laser forms an effectively smaller excitation spot in the center of the donut beam (Fig. 3.4). By employing a sufficiently high laser power, lateral resolution of tens of nanometers has been achieved [191], while a similar axial resolution was shown by adding a second objective in the 4Pi configuration (4Pi-STED) [192].

Similar concepts has been employed in more general ground-state depletion (GSD) [193, 194] and reversible saturable optical fluorescence transitions (RESOLFT) microscopies [195, 196], aiming at decreasing the extremely high power densities necessary for STED ($\approx 10^9\ W/cm^2$). With these techniques the sub-100 nm resolution can be achieved using low laser power ($\approx 10^3\ W/cm^2$), suitable for living biological samples. Higher laser power can be still used to achieve single-nanometer resolution on stable emitters (e.g. color centers in diamond [197]).

A completely different approach to patterned illumination, called Structured-Illumination Microscopy (SIM), was proposed back in 1966 by Lukosz [198] and implemented in 2000 by Gustafsson [199]. This technique employs a sinusoidal illumination pattern, generated by a laser beam incident on a diffraction grating. Such illumination creates a so-called Moire pattern, which shifts high spatial frequencies to lower ones, thus enabling them to be imaged

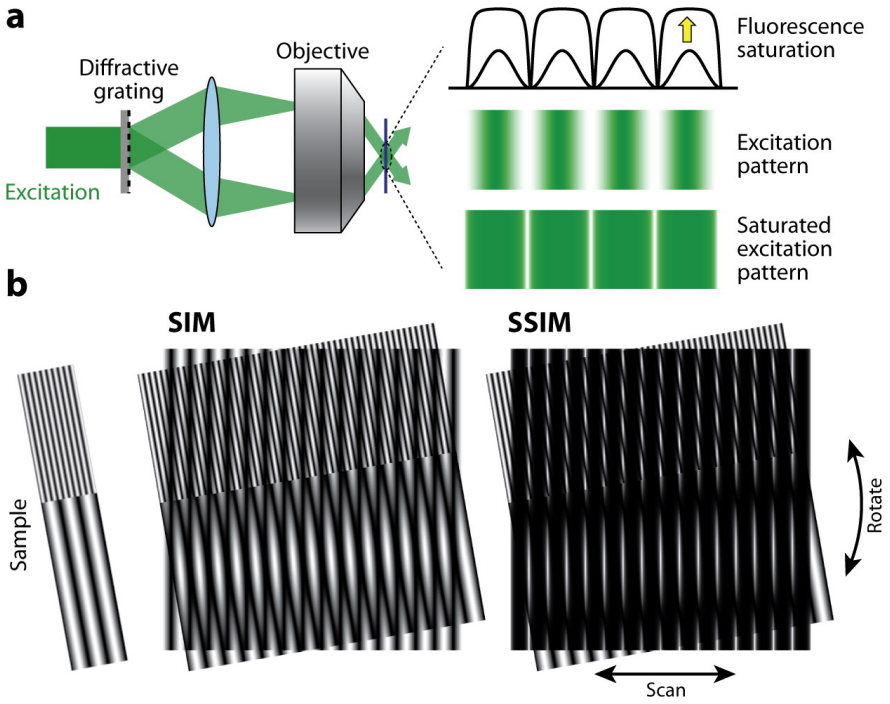

Figure 3.5 – The principle of SIM and sSIM. (a) To generate the illumination pattern a diffractive grating is put into the excitation path, which splits the laser light into two beams. Their interference creates a sinusoidal illumination pattern in the sample plane, which can saturate the fluorescence emission at the peaks without exciting fluorophores at the zero points (b) When a sinusoidal illumination pattern is applied to a sample, a Moiré pattern of a lower spatial frequency is generated and can be imaged by the microscope. Several images are acquired by rotating the excitation pattern and are then used to reconstruct the super-resolved image. sSIM further introduces a high-frequency component into the excitation pattern, allowing features far below the diffraction limit to be resolved. Figure reprinted with permission from Ref. [171].

by the same objective lens. Theoretically achievable resolution limit of SIM is $\lambda/4$, however much higher resolution up to $\lambda/12$ has been demonstrated using non-linear saturated SIM (sSIM) [200]. SIM is also particularly suitable for imaging the dynamics of biological samples in real time [201, 202] as it generally utilizes much lower laser power than STED-like techniques and requires only several frames to reconstruct the super-resolved image unlike localization microscopy methods.

3.1.4 Localization microscopy methods

The basic idea of localization microscopy is easy to guess from its name. Each fluorescent emitter, represented by an Airy disk, can be localised after image acquisition with high resolution. In fact, localization precision, briefly discussed earlier, can surpass the Abbe resolution limit by $\sqrt{N}$, where N is the number of detected fluorescent photons. For most fluorophores N, also called a photon budget, lies within the range of 100-1000 photons, bringing the localization

down to tens of nanometers and lower [177, 188, 203].

This however is not enough by itself to improve the resolution of the acquired images in case the fluorophores are positioned closer than the diffraction limit. Such dense distribution of emitters is nevertheless prevalent for labelling biological structures and is often the case for solid-state defects. The key to enhancing the resolution is the ability to distinguish the signals from nearby emitters within the diffraction-limited spot, which is mostly done by separating their emission in time (see Fig. 3.6).

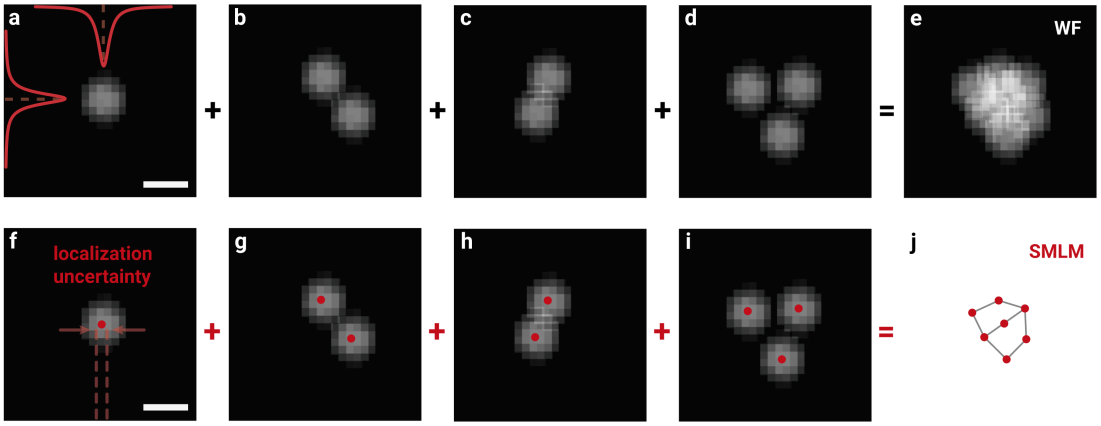

Figure 3.6 – The principle of Single-Molecule Localization Microscopy (SMLM). Individual blinking emitters are recorded with a widefield (WF) microscope as a stack of frames (a-d) and their average (e) gives a blurry image of an hBN flake. However, by localizing individual emitters (fitting the intensity distribution using a 2D Gaussian) on each of the frames (f-i), one can arrive at a much higher localization precision, effectively replacing a widefield PSF by a nanometer-sized point. Summing up all localizations produces the reconstructed super-resolved image (j), allowing to distinguish individual emitters. For larger numbers of emitters in real-life samples thousands of frames are required to effectively sample the structure of interest. Figure inspired by Ref. [186].

The first techniques to implement this concept (PALM - PhotoActivated Localization Microscopy [204], STORM - Stochastic Optical Reconstruction Microscopy [205], FPALM - Fluorescence PhotoActivation Localization Microscopy [206]) were using photoswitchable fluorophores, which could be activated by a brief illumination with a shorter-wavelength laser. After activation they could be excited from the ground to the excited state by using a laser of a longer wavelength, which eventually caused the bleaching of the fluorophores that needed to be reactivated with a shorter-wavelength laser for the next imaging cycle. Separating activation and excitation of the flurophores allowed one to control the fraction of fluorophores emitting at the same time, so that the emitters on a single frame are not too dense to be independently localized. This activation-excitation sequence could be repeated a desired amount of times to sample the structure of interest and obtain resolution down to tens of nanometers [204–206].

These groundbreaking super-resolution methods laid the foundation for the whole field of Single-Molecule Localization Microscopy (SMLM) [188], which has shown tremendous

progress since then. For example, activation, excitation and emission of fluorescence can be also asynchronous, thus speeding up the image acquisition and simplifying the experimental setups [207, 208]. This can be achieved either by utilizing special imaging buffers causing redox reactions [209] or chemically engineering fluorophores with intermittent emission [208, 210, 211]. Another SMLM approach using the binding kinetics of fluorophores to target molecules, called Point Accumulation for Imaging in Nanoscale Topography (PAINT), was first implemented with fluorescent dyes [207, 212, 213] and later developed to be used with fluorescently-labeled DNA strands (DNA-PAINT) [214, 215].

In contrast to fluorescent dyes and proteins, which need to be specifically engineered or treated to be suitable for SMLM applications, fluorescent defects in solid-state materials often exhibit intermittent emission (blinking) by default. This blinking behaviour can be caused by charge traps in the host material [47, 216], photo-ionisation [130, 217, 218], interaction with dissolved charges in solutions [132, 219], etc. Even though for many applications blinking can be detrimental (e.g. single-photon emission for quantum optics and quantum information processing) [15], it provides an invaluable resource for SMLM [216, 220, 221]. Now, powerful SMLM methods could be applied to explore the properties of optically active defects in wide-bandgap materials on an ensemble level with nanoscale resolution, which will be demonstrated in the following sections.

3.2 Super-resolution imaging of defects in hBN

The first attempts to image optically active defects in hBN with super-resolution techniques utilized the GSD-like approach [222] to reduce the effective PSF of a single emitter below the diffraction limit. While successfully exploiting the photophysics of certain hBN defects to demonstrate the proof-of-principle PSF reduction, the early work did not attempt at resolving two closely spaced emitters. Such imaging of two hBN emitters within a diffraction limited spot has been done only very recently using STED [223, 224], achieving a resolution of ≈ 50 nm.

However, the first large-scale demonstration of super-resolution imaging of defects in hBN flakes has been done using SMLM [130]. Here the authors imaged CVD-grown monolayer hBN, which has been transferred onto silicon nitride support chips. The defects present in as-grown hBN flakes showed bright PL signal when illuminated with both 488 and 561 nm lasers and intense blinking when immersed in water. Two types of fluorescence emission were identified, centered around 580 and 620 nm, by analysing thousands of optically active defects.

Further work in this direction has been focused on applying SMLM methods to study spectral and temporal properties of hBN emitters depending on the defect fabrication method and the environmental conditions. The details of this exciting journey are presented in chapters 4-7.

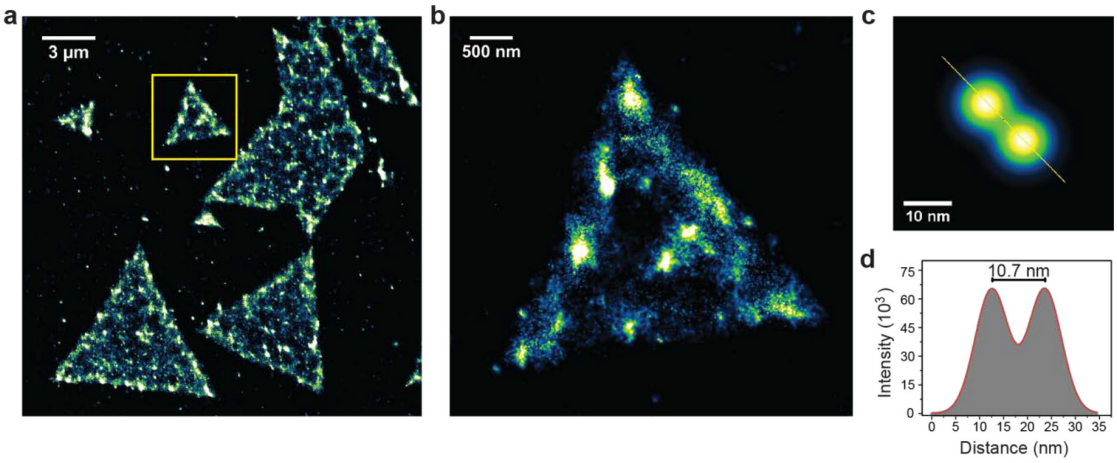

Figure 3.7 – Imaging optically active defects in hBN flakes (a,b) with nanoscale resolution using SMLM. The resolution of 10.7 nm is estimated as a minimum separation between two active defect sites (c,d). Reprinted with permission from Ref. [130].

4 Studying ensembles of defects in hBN using sSMLM

In this chapter I will introduce the spectral SMLM (sSMLM) technique and its application to studying the spectral behaviour of hBN emitters on an ensemble level. This text is the accepted version of the paper

Jean Comtet[1], Evgenii Glushkov[1], Vytautas Navikas[1], Jiandong Feng[2], Vitaliy Babenko[3], Stephan Hofmann[3], Kenji Watanabe[4], Takashi Taniguchi[4], Aleksandra Radenovic[1] *Wide-Field Spectral Super-Resolution Mapping of Optically Active Defects in Hexagonal Boron Nitride*. **Nano Letters** 19, 2516–2523 (2019).

A.R. and J.F. conceived of the project and designed experiments. J.C. developed the experimental setup for spectral imaging. J.C., E.G. and N.V. performed the experiments. V.B. and S.H. produced the CVD-grown hBN samples. K.W. and T.T. produced the bulk hBN crystals. J.C. wrote the paper with input from all authors. A.R. supervised the project.

[1]Laboratory of Nanoscale Biology, Institute of Bioengineering, School of Engineering, École Polytechnique Fédérale de Lausanne (EPFL), 1015 Lausanne, Switzerland

[2]Zhejiang University, Tianmushan Road 148, Xixi Campus, Xi-6, 201, Hangzhou, 310027, China

[3]Department of Engineering, University of Cambridge, JJ Thomson Avenue, CB3 0FA Cambridge, United Kingdom

[4]National Institute for Materials Science, 1-1 Namiki, Tsukuba 306-0044, Japan

4.1 Introduction

Defects in wide-band gap semiconductor materials lead to the creation of energy states well within the band gap, conferring these materials with new and exciting properties due to quantum confinement. A popular and well-studied example of point defects are nitrogen-vacancy (NV) centers in diamond, which can act as single-photon emitters [225], ultrasensitive magnetometers [226] and biological sensors [26].

In recent years, 2D semiconductors and insulators have emerged as new classes of materials able to host functional defects. Single-photon emission from such defects has been demonstrated in 2D Transition-Metal Dichalcogenides at cryogenic temperatures [66–69] and in hexagonal boron nitride (hBN) at room temperature [95]. Defects in 2D materials show great promise for many applications in integrated photonics [57]. The 2D nature of the material favors integration in photonic circuits, while allowing high light-extraction efficiency [6]. Defects in 2D materials also exhibit high sensitivity to their environment, leading to tunable properties [227] and allowing deterministic positioning of emitters through strain engineering [74, 101, 228].

However, defects can also be detrimental, leading to a decrease in the electrical and mechanical properties of materials. For example, the use of hBN as an encapsulation layer in nanoelectronics [62] can be dramatically affected by the presence of defects, causing increased scattering or facilitated dielectric breakdown [229], and precluding for now the use of CVD-grown hBN materials as efficient insulating layers in nanoelectronics [230].

Due to their atomic-scale nature, characterizing defects can be very difficult. Defects can be imaged with high spatial resolution in a transmission electron microscope (TEM) [130], but TEM imaging by itself tends to induce more defects in the sample, and is restricted to very small (~10 nm^2) areas. High-resolution Scanning Probe Microscopy techniques have allowed characterization of 2D materials at the single-defect level [143], and 2D material systems have also been investigated using near-field scanning optical microscopy (NSOM)[144]. Unfortunately, all these scanning techniques share similar limitation as TEM concerning time-consuming sample preparation and small imaging areas. Finally, confocal techniques [95] have been successful at characterizing the optical properties of single defects, but require very sparse samples due to diffraction-limited imaging. There is thus a clear demand in the development of new strategies allowing large-area characterization of defects in 2D materials.

With this goal in mind, we recently established single-molecule localization microscopy (SMLM) as a viable strategy for wide-field mapping of optically active defects in hBN [130]. Using the transient emission properties of individual emitters, we could separate emitters spatially down to 10 nm [130]. However, purely spatial SMLM techniques are still hampered by their lack of contrast, which can lead to substantial overcounting or undercounting of defects densities and precludes multidimensional measurement of defects properties, such as polarization, and spectra.

In this work, we focus on prototypical optically-active defects in hBN, and demonstrate that the implementation of spectral information concomitant to spatial SMLM (obtained by placing a prism in the detection path) is a valuable step forward in the large-area, nondestructive characterization of 2D materials and beyond. Our combined wide-field spectral and spatial super-resolved technique allows the determination of statistical ensemble spectral properties, as well as extraction of spatial, spectral and temporal dynamics of single defects. We demonstrate our approach on both monolayers of CVD-grown hBN materials, as well as irradiation induced surface defects in bulk exfoliated hBN materials. Similar operational principles could be applied to transition metal dichalcogenides at cryogenic temperatures [66–69] or other wide-band gap materials at room temperature such as aluminum nitride, silicon carbide and perovskites [231, 232]. Our approach opens up broad perspectives in the use of SMLM techniques for wide field characterization of defects in a variety of materials, and paves the way for wide-field quantitative multidimensional imaging of optically-active defects [233].

4.2 Experimental set-up

Our set-up is based on a wide-field spectral super-resolution imaging scheme, using a prism in the detection path, previously developed in a biological context [234–236], and with recent extension in physical science fields such as chemistry [237]. As shown schematically in Figs. 4.1a-b, we excite the hBN samples using a 561 nm laser. The energy of the excitation laser (2.21 eV) is well below the band-gap of the hBN material (~ 6 eV), leading to the selective excitation of defects with energies well within the band-gap of the material. Excitation beam from the laser is focused onto the back focal plane of a high numerical aperture oil-immersion microscope objective, leading to the widefield illumination of the sample. hBN samples are deposited on silicon chips and immersed in water to prevent changes of refractive index in the optical path. Wide-field photoluminescence emission from the sample is collected by the same objective and separated from the excitation laser using dichroic and emission filters. Emission light is then split through two paths using a beam-splitter (Fig. 4.1b). Part of the emission going through Path 1 is directly projected onto one half of an EM-CCD chip, with a back-projected pixel size of 100 nm (Fig. 4.1d, Path 1). Emission from individual defects leads to the appearance of diffraction-limited spots on the camera chip (Fig. 4.1d, red boxes), which can then be localized with sub-nanometer accuracy, with a localization uncertainty $\sigma_{\mathrm{x,y}} \sim \frac{\sigma_{\mathrm{PSF}}}{\sqrt{N}}$, where $\sigma_{\mathrm{PSF}} \approx 150$ nm is the standard deviation of the Gaussian fit of emitter's intensity (corresponding to a diffraction-limited spot fixed by the Point Spread Function with FWHM of ≈ 350 nm) and N is the number of photons emitted by the defect during the acquisition of one frame. The second path consists of an equilateral calcium fluoride (CaF_2) prism. This dispersive element leads to an approximately linear shift Δy_{SPEC} [px] in the photoluminescence signal of each emitters relative to their emission wavelength λ, such that $\Delta y_{\mathrm{SPEC}} \sim a \times \lambda$, with $a \approx 0.25$ px/nm (see SI Fig. 1). As shown in Fig. 4.1e, the one-to-one correspondence between the simultaneous images of emitters in the spatial and spectral channels allows mapping of the spectrum of each individual emitter. The sample is further mounted on a

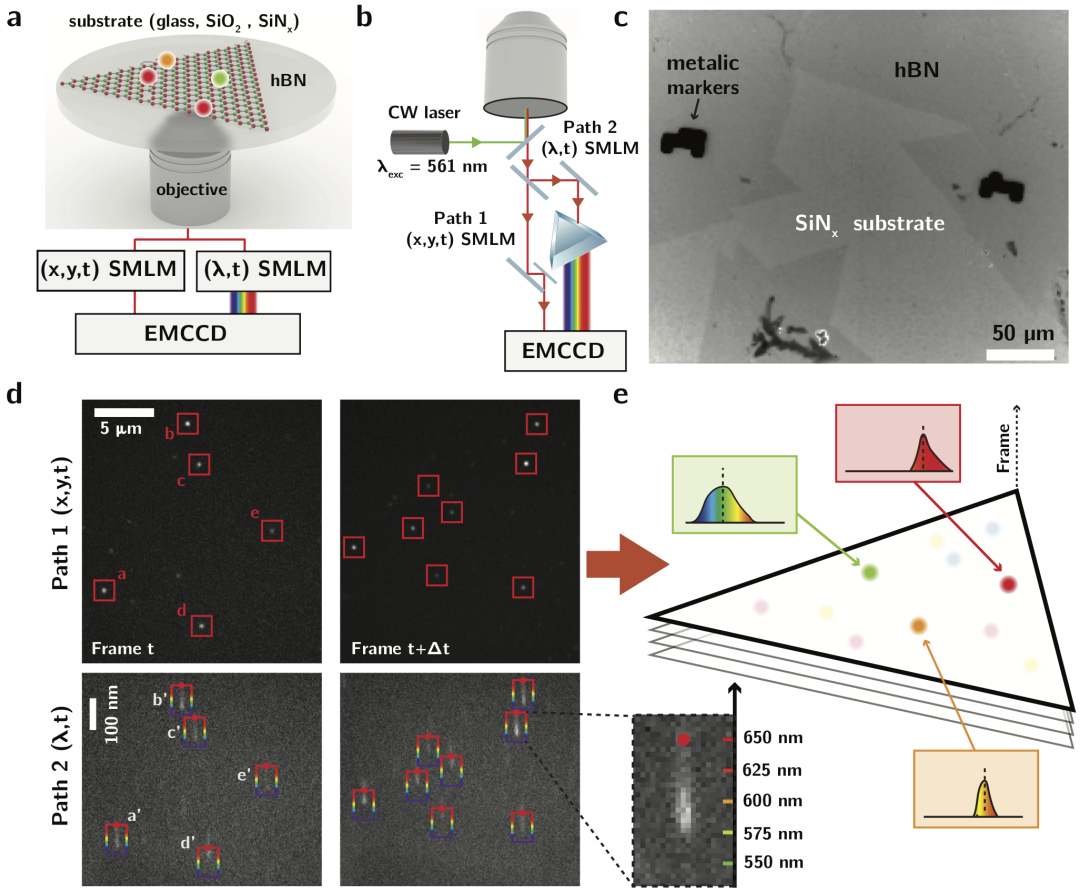

Figure 4.1 – Prism-based wide field spectral characterization of optical emitters in hBN. (a) Principle of the experimental set-up, allowing simultaneous spatial and spectral Single Molecule Localization Microscopy (SMLM) of emitters in hexagonal boron nitride (hBN). (b) Schematic of the experimental set-up. Upon laser excitation, fluorescence signal emanating from single defects is collected by a high NA objective and split towards two distinct paths for spatial (path 1) and spectral (path 2) characterization. Spatial Path 1 leads to diffraction-limited spots for individual emitters, which can be localized with sub-pixel accuracy. Spectral path 2 is composed of a dispersive prism element, shifting the fluorescence of individual emitters according to their emission wavelength. Images from both paths are then projected on the same chip of an EMCCD camera (see d). (c) Wide field image of CVD grown hBN flakes transferred on Si/SiNx chips. (d) Simultaneously recorded wide field image (path 1; x,y,t) and spectral image (path 2; λ,t) of emitters in hBN between successive frames at t and t+δt. Red boxes in Path 1 indicate spatial position of individual emitters, corresponding to diffraction-limited spots. Multicolor boxes in Path 2 show the corresponding images of individual emitters after vertical dispersion by the prism. Red dots in spectral channel indicate the mapped spectral position of 650 nm for each emitter in the spatial channel. The one to one correspondence between spatial and spectral path allows to obtain the full spectra of each individual emitter. (e) Principle of the reconstructed spectral super-resolved image.

piezoelectric scanner, and vertical drift is compensated using an IR-based feedback loop [238]. Residual lateral subpixel drift is compensated through postprocessing using cross-correlations between reconstructed super-resolved images (see Methods for further experimental and computational details).

4.3 Results and Discussion

Continuous green laser illumination of the flakes leads to photoswitching (blinking) of the emitters between bright and dark states [130]. As shown in Fig. 1d, due to this blinking behavior, only a small subset of emitters is active between each frame. This sparse activation allows for spatial localization of individual emitters between each camera frame, and subsequent reconstruction of a spatial and spectral map by summing up successive images, as presented in Fig. 4.1e.

As shown in Fig. 4.2, our wide-field spectral SMLM scheme allows us to map the spectral properties of emitters present in the hBN flakes. We first plot in Fig. 4.2a the distribution of center spectrum for a CVD-grown flake. As can be seen in this distribution, two families of emitters stand out clearly and are characterized by emission spectra centered approximately around $\lambda_1 \approx 585$ nm ("green emitters") and $\lambda_2 \approx 640$ nm ("red emitters"). We can further map the spatial position of each type of emitters in the reconstructed spatial maps of Fig. 4.2b, by summing up individual localization events (as depicted schematically in Fig. 4.1e). The brighter dots on the map thus represent the most active defects, which are emitting through most of the acquired frames. This spectral map allows for a direct estimation of the spatial localization of each defect type. Despite the presence of areas with varying densities of defects in each flakes, no clear spatial segregation is observed between red and green emitters, as they are homogeneously represented throughout the sample.

This type of multimodal spectral distribution is observed throughout our samples. We report in Fig. 4.2c the values of center wavelength for 5 distinct flakes, obtained using similar growth conditions and transfer procedures. Note that several modes can occasionally be observed for the red emitters (Flakes 2 and 4 in Fig. 4.2c, see Fig. S2 for details). Overall, emitters centered around 585 nm have relatively narrow spectral linewidth (FWMH $\approx$ 15 nm), consistent with recent report on similar CVD-grown materials [109], while the second group of emitters (with wavelength between approximately 610 nm and 650 nm) have larger spectral linewidth and show a relatively large sample-to-sample variation, which can be attributed to a variation in the local mechanical [111, 112] and electrostatic[109] environment associated with each flake (e.g. due to residual strains developed during the transfer process). Finally, we show in Figs. 4.2d-e the evolution of the number of localizations per frames and the spectral distribution over more than 30 minutes. As is depicted in Figs. 4.2d-e, the number of localizations per frames decreases exponentially, with a characteristic time $\tau \approx 10$ s due to bleaching of the emitters, while spectral emission remains stable, with progressive reduction of the FWMH of

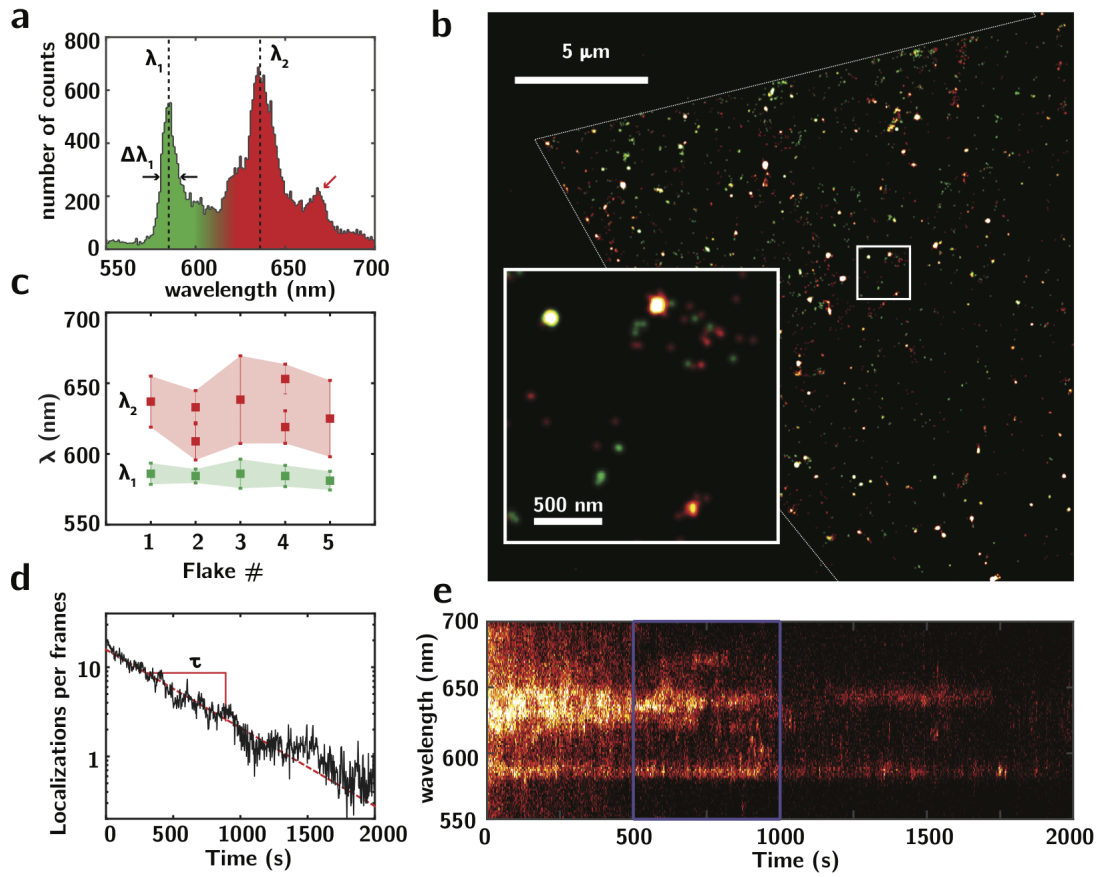

Figure 4.2 – Wide field super-resolved spectral and spatial map of single emitters in CVD-grown hBN flakes. (a) The spectral distribution of center emission wavelengths for a CVD-grown hBN flake. A dual distribution is observed, corresponding to green and red emitters of respective center emission wavelength λ_1 and λ_2. Smaller emission peak indicated by red arrow corresponds to a phonon side-band (see text for details). Bin size is 1 nm. (b) Corresponding spatial map with spectral contrast, showing the position of the two types of emitters throughout the flakes. Localization events are rendered as gaussian spots (see Methods). Spatial maps are rendered from 10,000 successive frames. (c) Sample to sample variation of center wavelengths. Error bars are FHWM. (d) Temporal evolution of the number of localizations per frames (acquisition with 50 ms sampling and 20 ms exposure time). (e) Temporal evolution of the spectral distribution. Blue zone indicates the region used for reconstructing the spatial images in (b) and the distribution in (a).

red emitters probably due to bleaching. Importantly, localizations and wavelength matching can be performed as fast as 20 per frames, showing the potential of the technique for large-area and high-throughput mapping in dense samples. Bleaching in turn can happen due to irreversible photo-oxidation of defects, exposed to the external environment due to the 2D nature of the flakes.

We now proceed in Fig. 4.3, to the characterization of the spatial, spectral and temporal dynamics of individual emitters in hBN, using our wide-field SMLM spectral and spatial super-

resolution scheme. We show that at least two types of defects are responsible for the observed emission lines in CVD-grown flakes (Figs. 4.2a-c). In Fig. 4.3a we first report super-resolved images of individual emitters, rendered as spatial histograms of localizations, using a pixel size of 5 nm. As shown in Fig. 4.3b, we obtain approximately Gaussian distributions, corresponding to spatial uncertainty σ_x between 15 and 20 nm. This value is slightly larger than the estimated spatial uncertainty of each localization, based on photon counts (of the order of 7 nm), which is probably due to residual drift. Remarkably, over the entire number N ≈ 1000 of localizations, this leads to a corresponding final uncertainty for the individual defect center position as low as $\frac{\sigma_x}{\sqrt{N}} < 1$ nm for the most active defects. The central emission wavelength of individual defects (Fig. 4.3c) and full emission spectrum (Fig. 4.3d) can then be measured using the procedure described in Fig. 4.1d. As shown in Fig. 4.3c, for the two representative types of emitters, relatively constant spectral emission is observed over 600 successive localization frames, with distribution width $\Delta\lambda \approx 5$ nm.

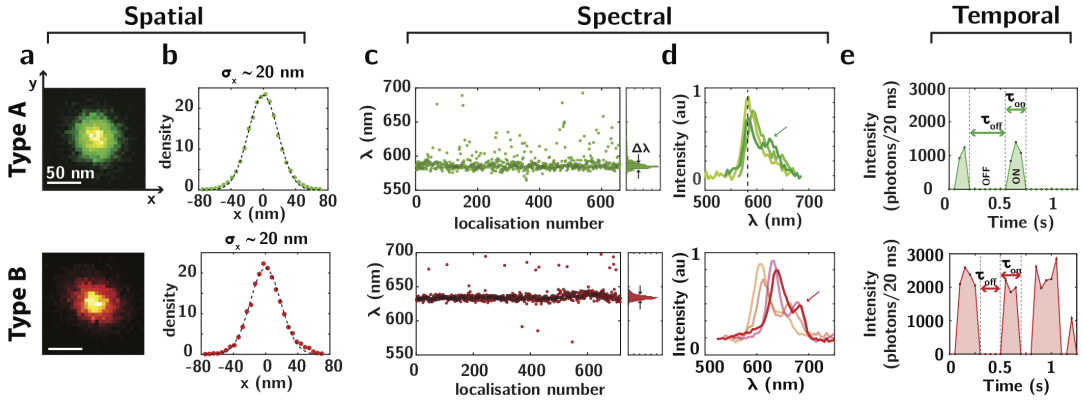

Figure 4.3 – Spatial, Spectral and Temporal dynamics for the two types of defects. (a) Super-resolved image of individual emitters, rendered as spatial (2D) histogram of localization coordinates, with 5 nm pixel size. (b) Projected distribution along the x axis along with Gaussian fit (dotted line), allowing the determination of localization uncertainty σ_x. (c) Variation of the mean emission wavelength over successive localizations, and histogram of emission wavelength. (d) Representative spectra of emitters. The vertical dashed line represents mean emission wavelength. Green and red arrows show respectively phonon sideband in type A and type B emitters. (e) Time trace of emission intensity, showing intermittency in the emission, leading to successive ON and OFF states. All measurements presented here are acquired with 50 ms sampling and 20 ms exposure time.

Representative spectra for the first defect type ("type A") are shown in green in Fig. 4.3d. These defects have a mean emission wavelength centered along the first peak $\lambda_1 \sim 585$ nm in the spectral histogram of Figs. 4.2a,c. Emission spectrum is asymmetric and a phonon sideband can be occasionaly resolved on some spectra (Fig. 4.3d, green arrow). The second type of defect ("type B") is characterized by a mean emission wavelength centered along the second peak $\lambda_2 \sim$ 610-650 nm of the spectral histogram. The spectrum shows a clear Zero Phonon Line and Phonon Sideband, leading to an energy detuning of ~ 140 meV, consistent with previously published work [97, 98, 239]. Remarkably, this phonon sideband is also visible on the ensemble histograms, in the form of a third local maximum in the spectral distribution

(Fig. 4.2a, red arrow). A representative time trace for the emission of each individual emitter is shown in Fig. 4.3e. All defects systematically exhibit a blinking behavior, characterized by emission intermittency, and successive ON and OFF events.

To verify the generality of our approach, we characterized defects in a second class of hBN materials. We started from high-quality bulk hBN crystals [76], which were exfoliated and deposited on Si/SiO_2 substrate (see Fig. S3). Few emitters, corresponding to both type A and type B, were observed on the as-exfoliated flakes, traducing the high quality of the bulk hBN material (see Fig. S4). In order to induce defects in the structure, we exposed the exfoliated crystals to 30 s of oxygen plasma treatment [240] (see Materials and Methods). As shown in Fig. 4.4a, this leads to creation of emitters at the surface of the flakes, with similar blinking behavior as in CVD-grown materials, allowing straightforward localization using SMLM-based spectral super-resolution mapping (representative time trace shown in Fig. S5). Interestingly, as illustrated in Figs. 4.4b-c, the spectral distribution in most of the investigated samples is characterized by a single emission wavelength, showing preferential creation of type A emitters by plasma treatment. Surprisingly, some of the investigated flakes also showed a significant population of type B emitters (Fig. 4.4c, flakes number 2 and 6 and Fig. S6) although most of these emitters are unstable and bleach irreversibly after a few tens of seconds. This differential bleaching could be attributed to distinct chemical reactivity of the two populations of defects.

Focusing on CVD-grown hBN, we now turn in Fig. 4.5 to the photophysical properties of emitters and specifically their intensity and blinking kinetics. We show in Fig. 4.5a a 2D histogram of photon counts as a function of the emission wavelength for the flake investigated in Fig. 4.2. Two clusters (green and red dashed circles) corresponding to type A and type B defects identified in Figs. 4.2a and 4.3 stand out clearly, with high brightness of the order of $\sim 5.10^4$ photons/second. As evidenced on the map, no clear difference of brightness can be made between each type of defects. Phonon Sideband for type A and type B emitters can be identified in this histogram (black circled clusters). To obtain more insight into the properties of the defects in terms of photon emission, we show in Fig. 4.5b the full distribution of emission intensity by grouping the defects according to their wavelength. Interestingly, we observe a long tail in the intensity distribution, in strong contrast to the Poissonian distribution classically expected for non-blinking emitters [241].

Another interesting feature of the emitters investigated here is their blinking kinetics, also observed in several other studies [130, 239, 241], but contrasting with other reports of long-term emission stability for the emitters in hBN [6, 240]. To gather more insight into this blinking behavior, we plot in Figs. 5c-d the distributions of ON and OFF time for defect types A and B (see Materials and Methods). We observe clear power-law distributions, with $P_{\mathrm{on/off}}(t) \sim t^{\alpha_{\mathrm{on/off}}}$, and $\alpha_{\mathrm{on}} \approx \alpha_{\mathrm{off}} \approx 1.9 \pm 0.2$ (red and green lines, Figs. 4.5c-d). Remarkably, these power-law distributions and the associated exponents are consistent with previously observed blinking kinetics on quantum dots [242, 243], where blinking is attributed to ionization of the quantum dots and escape of photoexcited carriers towards surrounding charge traps in the material. Importantly, the power-law scaling characterizes the absence of intrinsic time-scales

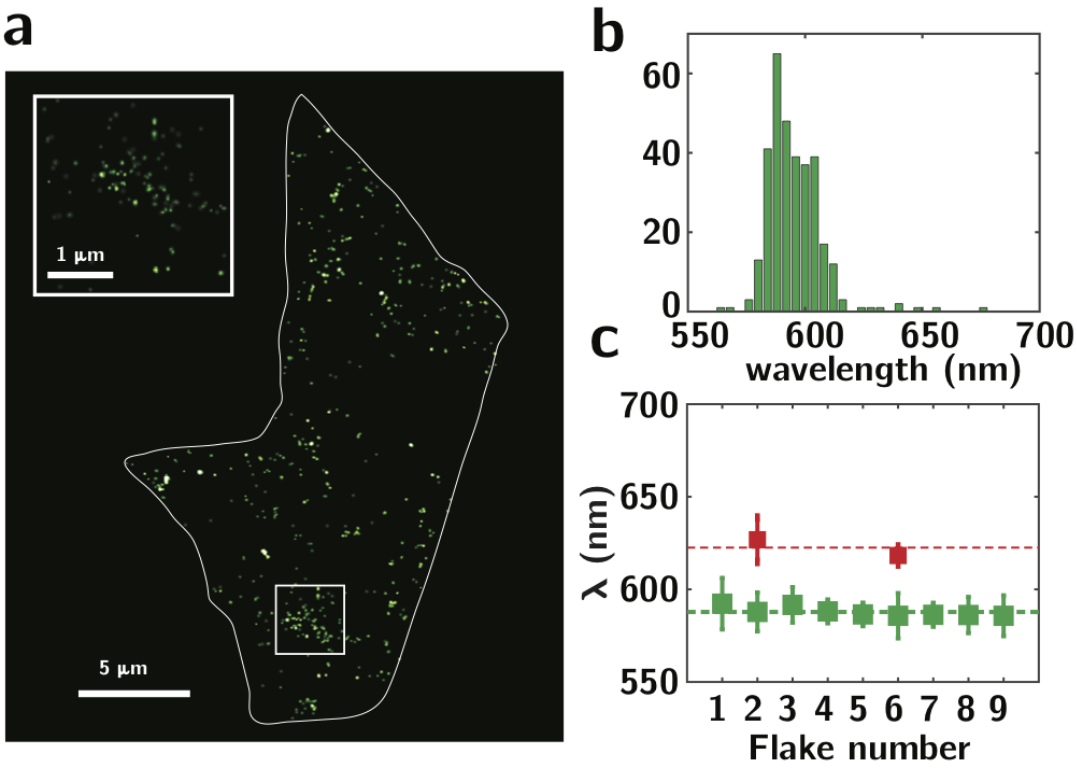

Figure 4.4 – Spatial and spectral characterization of plasma treated exfoliated hBN flakes. (a) Reconstructed map of individual emitters in exfoliated hBN flake, submitted to oxygen plasma for 30 s (see Methods). (b) Distribution of emission wavelength. (c) Sample to sample variation of the emission wavelength. Bin size is 4 nm.

in the blinking behavior and can be interpreted as being due to heterogeneity of charge traps at the material's surface. Similar mechanisms due to photoinduced ionization and change of the charge state of the defects were proposed to explain blinking in NV centers in diamond [218]. The blinking behavior observed in our samples might thus take its origin from charge separation or ionization of the defects, as the monolayer nature of the CVD-grown hBN flakes, and the creation of surface traps in plasma-treated hBN crystals, might allow in both cases for a facilitated escape of photoexcited charge carriers towards surrounding charge traps. This observation suggests a rationale behind the increased photostability observed in annealed samples, as a way to desorb impurities acting as charge traps. Remarkably, the observed similarity in blinking kinetics suggests similar charge affinities for each types of defects (red and green dots, Figs. 4.5c-d). Finally, the long tail in the distribution of emission intensity, shown in Fig. 4.5b, could be related to the observed power-law distribution of blinking times.

An important question remains to understand the reasons for the spectral heterogeneity evidenced in our study and the presence of different emission lines and defects states in CVD grown hBN and irradiated bulk hBN crystals. In the quest towards the assignment of a precise chemical structure to optically active defects in hBN materials, recent works have shown a

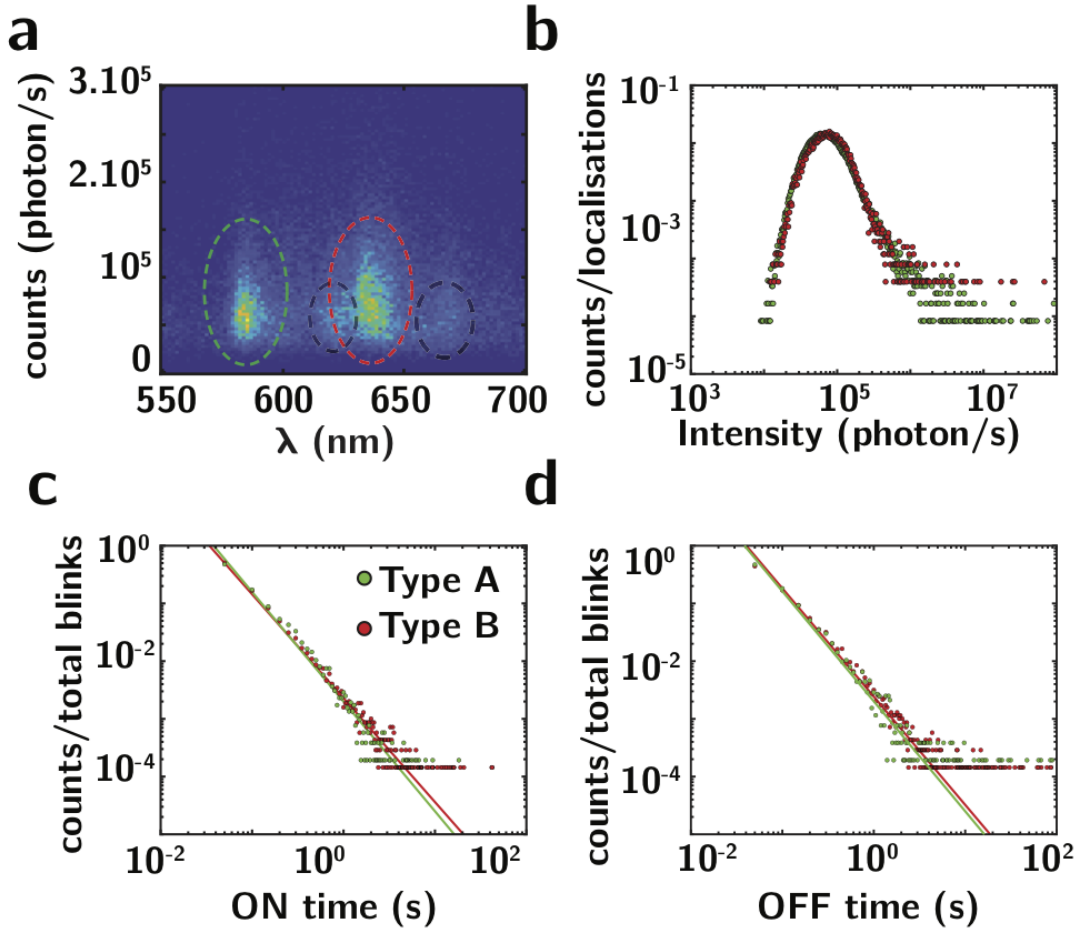

Figure 4.5 – Photo physical properties of emitters in CVD hBN. (a) 2D histogram of photon counts as a function of emission wavelength. The two main clustered distributions are circled in green and red. Phonon sideband of type A and type B emitters are circled in black. (b) Histogram of emission intensity. Red and green dots correspond to each circled distribution in (a). Normalized histograms of on (c) and off (d) times for type A and type B emitters (see Supplementary and Methods). Straight lines indicate power-law scaling of each distribution.

widely heterogeneous spectral response of defects in hBN [97, 244], which was attributed to different chemical structures [245, 246], but also differences in the charge states [239, 247], local dielectric [241], electrostatic [109] and strain environment [111], as well as temperature [244]. Multimodal emission lines with modes around 585 and 630 nm were also observed in several studies [239, 246]. While the blinking behavior observed for each types of defects (Fig. 4.3e) is probably due to reversible ionization or charge trapping, it is also concurrent with clear spectral stability for the emission in the ON state (Fig. 4.3c). Furthermore, the observation of similar blinking characteristics for types A and B defects (Figs. 4.5c, d) suggests similar charge affinities for these two populations. The differences in the spectral shape and zero phonon line distribution of type A and B defects (Figs. 4.2c and 4.3d) could thus point to distinct

chemical structures for these two populations, variations in their local dielectric environment or distinct charge states. Furthermore, the large variation in spectral emission amongst type B defects within different CVD-grown flakes might be attributed to residual strain developed during the transfer process. Despite their relatively large uncertainty, we can expect theoretical predictions from Density Functional Theory to further guide the identification of the exact chemical structure of each type of defects [248], based on their emission wavelength and spectra. Noteworthy, Adbi and coworkers [129] reported Zero Phonon Line for N_BV_N and V_B^- defects of 2.05 eV and 1.92 eV, respectively, corresponding to 605 nm and 647 nm emission wavelength, which is in a relatively fair agreement with our experimental results. However, the fact that we find predominantly one defect type in plasma treated exfoliated flakes might also suggest that type A correspond to intrinsic defects, while type B might occur due to substitutional doping with various impurities, such as C_BV_N [134], or to various oxygen or hydrogen complexes or interstitial defects [137].

4.4 Conclusion

We have shown the potential of spectral SMLM techniques for wide-field and high-throughput spectral mapping and characterization of defects in hBN materials. Our methodology allows the determination of statistical ensemble spectral properties, as well as extraction of spatial, spectral and temporal dynamics of single defects. We identify at least two types of defects in CVD grown materials, while irradiated exfoliated flakes show predominantly one type of defect. Further analysis of the blinking kinetics of optical emitters suggests that blinking is due to transient trapping of photoexcited charge carriers at the material's surface, similar to what is observed in quantum dots. This behavior provides strategies for blinking reduction and increase of photostability through encapsulation of defects and reduction of charge traps via thermal annealing. Our study demonstrates the potential of spectral SMLM as a wide field and high-throughput characterization technique in material science and paves the way towards multidimensional mapping of defects' properties.

4.5 Materials and Methods

4.5.1 Optical set-up

The sample is excited using a 561 nm laser (Monolitic Laser Combiner 400B, Agilent Technologies). Excitation power during imaging, measured at the back focal plane of the microscope objective varies from 20 to 65 mW, corresponding to power densities ranging from 250-800 kW/m^2. We used a high numerical aperture oil-immersion microscope objective (Olympus TIRFM 100X, NA = 1.45). Wide-field photoluminescence emission from the sample is collected by the same objective and separated from the excitation laser using dichroic and emission filters (ZT488/561rpc-UF1 and ZET488/561m, Chroma). Paths 1 and 2 consist of two telescopes26, sharing the same lens L1, with a respective magnification factor 1.6 (Path

1, telescope L1-L2) and 1.4 (Path 2, telescope L1-L3). Lenses are achromatic doublet lenses (Qioptic, L1: f/100, L2: f/160, L3: f/140). The prism (PS863, Thorlabs) is placed at the Fourier plane between L1 and L3, at the angle of minimum deviation. The sample is mounted on a piezoelectric scanner (Nano-Drive, MadCityLabs) to compensate for vertical drift using an IR-based feedback loop28. EM-CCD camera (Andor iXon Life 897) is used with an EM gain of 150.

4.5.2 Fitting and spectral assignment and SMLM images

Localization: Emitters in the spatial and spectral channels are localized using the imageJ plugin, *Thunderstorm* [249]. Briefly, a wavelet filter is applied to each frame. Peaks are then fitted by 2D integrated Gaussians. In the spatial channel, only emitters with intensity at least twice of the background are considered.

Spectral calibration: Calibration between spatial and spectral channels is conducted using red fluorescent beads (20 nm FluoSpheres carboxylated-modified, 580/605). First, we calibrate the field-of-view transformation between spatial and spectral channels. For an emitter with a given wavelength, the relation between its position in the spatial and spectral channel is well approximated by a relation of the form $(x_{SPEC},y_{SPEC}) = A.(x_{LOC},y_{LOC}) + B$, where (x_{SPEC},y_{SPEC}) and (x_{LOC},y_{LOC}) corresponds to the position vector of the emitter in the spectral and spatial channels, respectively, A is a 2x2 matrix and B is a vector. Coefficients for A and B are calibrated by raster scanning a fiducial marker of controlled emission wavelength and mapping its position in both channels. In a second step, bandpass filters with a central wavelength of 600 nm, 630 nm and 650 nm, respectively, and FWHM of 10 nm (Thorlabs, FB600-10) are used to calibrate the relation between the emission spectrum and the vertical shift in the spectral channel. The relation between the vertical shift Δy_{SPEC} [px] of the emission spectra and the emission wavelength λ, is well approximated by a linear relation such that $\Delta y_{\mathrm{SPEC}} \sim a \times \lambda$, with $a \approx 0.25$ px/nm (See Fig. S1).

Spectral assignment: In order to assign a spectra to an emitter, localized in the spatial channel at (x_{LOC},y_{LOC}), we compute its projected position $(x_{SPEC}(\lambda_0), y_{SPEC}(\lambda_0))$ in the spectral channel for a fixed emission wavelength λ_0=650 nm. A pair-search algorithm finds the closest localizations (x'_{SPEC}, y'_{SPEC}) in a vertically-elongated rectangular zone around $(x_{SPEC}(\lambda_0), y_{SPEC}(\lambda_0))$. The corresponding central emission wavelength λ is then estimated as $\lambda = \lambda_0 + 1/a.(y_{SPEC}(\lambda_0) - y'_{SPEC})$.

Spectra generation: Measured spectra in Fig. 4.3d are obtained by averaging the spectrum of single emitters over all frames for which spectral assignment is successful.

Image generation: SMLM images (Fig. 4.2b and 4.4a) are generated as probability maps by plotting 2D Gaussian centered on each position with a standard deviation equal to 20 nm.

Drift correction: Lateral drift is corrected using cross-correlation between reconstructed super-resolved images on CVD-grown materials. No lateral drift correction is applied on

exfoliated hBN flakes, as the lower density of defects leads to weak cross-correlations between reconstructed images.

Blinking kinetics: We obtain the blinking kinetics of type A and type B defects (Fig. 4.5c-d) by following the time-trace of 9 type A defects and 14 type B defects (histogram of mean emission wavelength shown in Fig. S7). OFF state is clearly defined by the absence of localization (Fig. 4.3e).

4.5.3 Sample preparation

CVD-grown materials: CVD-grown materials are produced under similar conditions as described elsewhere [89] (see Fig. S8 for SEM images of flakes on Fe foil). Briefly, as-received Fe foil (100 µm thick, Goodfellow, 99.8% purity) is loaded in a customized CVD reactor (base pressure 1x10^{-6} mbar) and heated to ~940 °C in Ar (4 mbar), followed by annealing in NH_3 (4 mbar). For the growth, 1x10^{-2} mbar NH_3 is used as a carrier gas and 6x10^{-4} mbar borazine $(HBNH)_3$ is introduced into the chamber for 30 minutes. The growth is quenched by turning off the heater allowing a cooling rate of about 200 °C/min.

The h-BN domains are transferred onto SiN_x chips using the electrochemical bubbling method [250] with PMMA as support layer. After transfer, PMMA is removed by successive 1-hour rinses in hot acetone (3 rinses), hot IPA (1 rinse) and hot DI water (1 rinse). Remaining PMMA contamination is further removed through overnight annealing at 400°C in an Argon atmosphere.

Exfoliated flakes: hBN multi-layer flakes are exfoliated from high quality bulk crystals [76] and deposited onto SiO_2 chips (Fig. S3). Type A and type B defects are detected at low concentrations in just-exfoliated flakes (Fig. S4). In order to create defects, hBN crystals are further exposed to a 30 s oxygen plasma at 100 mW under 30 sccm O_2 flow. No annealing was performed.

Sample imaging: Chips with deposited hBN flakes and CVD-grown materials are placed upside down on round coverslips (#1.5 Micro Coverglass, Electron Microscopy Sciences, 25 mm in diameter), previously cleaned in oxygen plasma for 5 minutes. Imaging is further performed in water at room temperature, in order to improve the optical contrast and prevent a discontinuous change in the refractive index. Performing experiments in air by transferring CVD-grown hBN flakes directly on a glass coverslip, we observed a similar spectral signature as that shown in Fig. 4.2, showing that water has little effect on the observed spectral response of this material.

5 On-chip high-throughput imaging platform

As discussed in Chapter 3, TIRF microscopy is highly beneficial for imaging optically-active defects in thin vdW materials. However, as one can see in Fig. 3.1, TIRF configuration typically has a much smaller field-of-view, than regular widefield approach, which prevents it from being used in high-throughput applications. One way to circumvent this limitation is by designing a dedicated high-throughput imaging platform, with decoupled illumination and collection paths, which is the focus of the section 5.1. The text in this section is the accepted version of the paper

Evgenii Glushkov[1], Anna Archetti[2], Anton Stroganov[1,2], Jean Comtet[1], Mukeshchand Thakur[1], Vytautas Navikas[1], Martina Lihter[1], Juan Francisco Gonzalez Marin[3], Vitaliy Babenko[4], Stephan Hofmann[4], Suliana Manley[2], Aleksandra Radenovic[1] *Waveguide-based platform for large-FOV imaging of optically-active defects in 2D materials.* **ACS Photonics** 6, 12, 3100-3107 (2019).

A.R., S.M. and E.G. conceived the project and designed the experiments. A.A. developed the experimental setup for waveguide-based imaging. E.G., A.A. and A.S. designed and fabricated the imaging chips. E.G., M.T., M.L. and J.M. performed the experiments. V.B. and S.H. produced the CVD-grown hBN samples. E.G., J.C. and V.N. performed the data analysis. E.G. wrote the paper with input from all authors. A.R. and S.M. supervised the project.

[1]Laboratory of Nanoscale Biology, Institute of Bioengineering, School of Engineering, École Polytechnique Fédérale de Lausanne (EPFL), 1015 Lausanne, Switzerland.

[2]Laboratory of Experimental Biophysics, Institute of Physics, School of Basic Sciences, École Polytechnique Fédérale de Lausanne (EPFL), 1015 Lausanne, Switzerland.

[3]Laboratory of Nanoscale Electronics and Structures, Institute of Electrical Engineering and Institute of Material Science, École Polytechnique Fédérale de Lausanne (EPFL), 1015 Lausanne, Switzerland.

[4]Department of Engineering, University of Cambridge, JJ Thomson Avenue, CB3 0FA Cambridge, United Kingdom

In section 5.2 we show a further development of this waveguide-based imaging platform, by directly growing thin hBN film on it and characterizing the optically-active emitters it the as-grown material. This approach helps avoid multiple problems related to transferring fragile vdW materials onto the imaging chips and enables future photonic integration of hBN emitters using CMOS-compatible processes. This section is based on the accepted version of the paper

Evgenii Glushkov[1], Noah Mendelson[2], Andrey Chernev[1], Ritika Ritika[2], Martina Lihter[1], Reza Zamani[3], Jean Comtet[4], Vytautas Navikas[1], Igor Aharonovich[2,5], Aleksandra Radenovic[1] *Direct Growth of Hexagonal Boron Nitride on Photonic Chips for High-throughput Characterization.* **ACS Photonics** 8, 7, 2033–2040 (2021).

A.R., I.A. and E.G. conceived the project and designed the experiments. E.G. designed and fabricated the imaging chips. N.M. performed the hBN growth. N.M. and R.R. characterized the as-grown material. E.G. performed optical imaging, A.C. and R.Z. performed TEM characterization, M.L. did the AFM imaging. E.G., J.C. and V.N. analyzed the data. E.G. wrote the paper with input from all authors. A.R. and I.A. supervised the project.

5.1 Characterizing defects in 2D materials using the waveguide microscope

Waveguides have been the workhorse of integrated photonics, serving as the basis for implementing compact passive components such as on-chip splitters, filters, interferometers, resonators and, multiplexers. To add functionality to photonic chips, one further needs to interface waveguides with other materials, which is usually done through coupling with the evanescent field of the waveguide. This method is especially suitable for 2D materials, which due to their minimal thickness down to just a few angstroms, are efficiently excited by the evanescent field from the waveguide [251]. This allows for the fabrication of various active components (light-emitting diodes, modulators, photodetectors) from 2D materials on top of the on-chip waveguides [252, 253]. Such devices may utilize not only the optoelectronic properties of the 2D material itself, but also those originating from the optically-active defects in these materials [70, 254, 255]. The existence of such point emitters has been reported for multiple transition-metal dichalcogenides (TMDCs) [66–69] at cryogenic temperatures and in hexagonal boron nitride (hBN) [95] at room temperature. Recent works have also shown the efficient coupling of the single-photon emission from these defects into the on-chip waveguides, making them a promising platform for the on-chip quantum optics [117, 118].

[1]Laboratory of Nanoscale Biology, Institute of Bioengineering, École Polytechnique Fédérale de Lausanne (EPFL), 1015 Lausanne, Switzerland.

[2]School of Mathematical and Physical Sciences, University of Technology Sydney, Ultimo, NSW, 2007, Australia.

[3]Centre Interdisciplinaire de Microscopie Électronique (CIME), École Polytechnique Fédérale de Lausanne (EPFL), 1015 Lausanne, Switzerland.

[4]Laboratory of Soft Matter Science and Engineering, ESPCI Paris, PSL University, CNRS, Sorbonne Université, 75005 Paris, France.

[5]ARC Center of Excellence for Transformative Meta-Optical Systems (TMOS), Faculty of Science, University of Technology Sydney, Australia.

Several imaging techniques were demonstrated to be suitable for studying such defects in 2D materials at different scales. Transmission electron microscopy (TEM) [138, 139] can be employed to image single defects over an area of several tens of square nanometers, which is however accompanied by the introduction of new defects during this process due to intense electron-beam irradiation of the studied sample [139, 140]. Near-field techniques, such as scanning tunneling microscopy (STM) [143] and near-field scanning optical microscopy (NSOM) [144] have also been also successfully applied to study defects in 2D materials. However, they are all limited by the size of the inspected area (typically, less than several square micrometers) and do not allow for high-throughput characterization of defects due to the time needed for sequential scanning.

While this can be tolerated for certain applications, novel high-throughput inspection methods are crucially needed to rapidly characterize defects in large-area 2D materials [256, 257]. This is especially important in the context of further wafer-scale integration of 2D materials into standard microelectronics fabrication processes. Here a technique-of-choice would be widefield optical microscopy, which uses camera detectors to image the entire field of view in a single shot and thus enables fast characterization of much larger areas than the above-mentioned methods, but provides significantly worse resolution due to the diffraction limit [130].

The quest to overcome this limit has been central in many areas of biology, which led to the creation of multiple super-resolution microscopy methods, including single-molecule localization microscopy (SMLM) [204, 205]. The SMLM technique is based on acquiring a large stack of successive images, each containing sparse switchable fluorophores, which are then localized frame-by-frame. SMLM has become very popular in the biological community, giving rise to the variety of implementations (PALM [204], STORM [205], SOFI [258], PAINT [207, 215], etc.) and the creation of ready-to-use commercial super-resolution microscopes by several manufacturers. Recently, however, this technique has found applications in material science [221] and was applied to study optically-active defects in 2D materials, by treating them as single emitters and reaching localization precisions below 10 nm [130]. Therefore, SMLM allows circumventing the tradeoff between small-scale, high-resolution TEM images and large-scale, low-resolution optical maps. Moreover, to simultaneously analyze not only spatial, but also the spectral distribution of optically-active defects in 2D materials, a spectral super-resolution technique was recently applied to study emitters in hBN [127]. This allowed their properties to be studied at the ensemble level and revealed multiple populations of fluorescent defects in this material.

Established widefield super-resolution techniques, however, typically provide a field-of-view of less than ~50x50 μm^2, which is further reduced down to ≈20x20 μm^2 in the total internal fluorescence (TIRF) mode, especially suitable for imaging 2D materials. This mainly happens due to the lack of the illumination uniformity achievable through high-NA objectives [259], and is insufficient for high-throughput characterization of 2D materials. To overcome this limitation and simultaneously increase the excitation efficiency of defects in atomically-thin

2D materials, one can use the integrated waveguides as an imaging platform by utilizing their evanescent field for excitation. This requires a certain re-thinking of the geometry of the waveguides, motivated by the high-throughput imaging requirements.

In the integrated photonics community, waveguides are typically meant to be single-mode, which limits their cross-sectional width to a fraction of a micrometer in the visible range. Obviously, this is not sufficient for large-area imaging, where ideally the width of the imaging waveguide should be expanded to tens of micrometers, being limited only by the imaging objective and the chip size of the camera used (≈200 μm for commercial detectors at suitable magnifications for single-emitter detection). Naturally, such wide waveguides are inherently multimode, so a slow adiabatic expansion of the single-mode waveguide to reach the required imaging width is needed in order to uniformly excite the photoluminescence in 2D materials [260].

Following this approach, we demonstrate here the use of a waveguide-based imaging platform, recently applied for SMLM bioimaging [184, 261], for the characterization of defects in 2D materials. The proposed platform decouples the excitation and collection paths, allowing the collection of the PL signal through a high-NA objective while simultaneously exciting the optically-active 2D materials over a large area (up to 100x1000 μm^2) in TIRF mode. This allows for a hundred-fold increase in imaging speed per area, compared to traditional TIRF microscopy or PL mapping, and paves the way towards high-throughput PL characterization and optical inspection of defects in 2D materials.

Experimental Setup

The central element of the waveguide-based imaging platform is a silicon chip with multiple silicon nitride (Si_3N_4) waveguides buried in the layer of silica cladding (Fig. 5.1a, b). The chip was designed using numerical simulations to have a high coupling efficiency, low losses and uniform field distribution [184], and fabricated using standard microelectronic fabrication processes (see Materials and Methods for details). Particular attention was paid to the input interface of the waveguides, where surface roughness strongly affects the coupling efficiency. To mitigate those losses, we utilized a two-step lithography and etching process, designed to minimize the damage to the input facet [184]. Further increase in coupling efficiency was achieved by adding an inverted taper coupler (~150 nm wide tip) at the beginning of each waveguide that increases the effective size of the fundamental mode to match the mode size of the input beam. Naturally, the optimal width of the input taper coupler depends on the excitation wavelength and the coupling method used (641 nm laser light and a 50x objective, in our case).

The second important requirement for a proper waveguide design is the reduction of transmission losses, maximizing excitation in the imaging area containing the 2D material. Transmission losses were reduced by covering the surface of the waveguides with a protective layer of SiO_2 cladding everywhere except for the small area, the so-called imaging well, where the

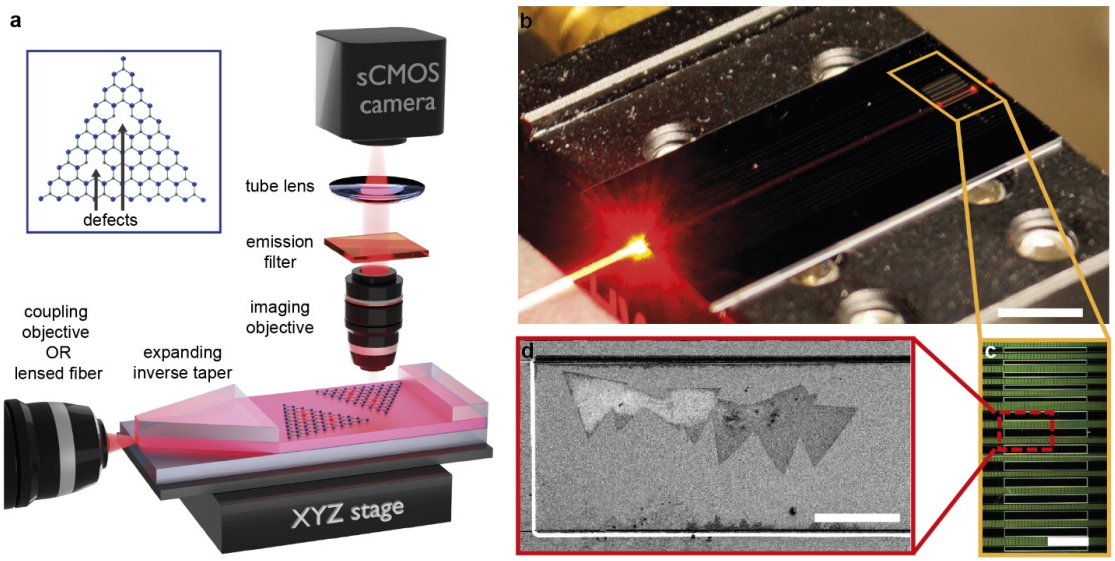

Figure 5.1 – Concept and implementation of the waveguide-based platform for high-throughput PL characterization and super-resolution imaging of 2D materials. (a) Simplified schematic of the imaging setup, where the laser light is focused onto the tapered entrance of the waveguide from the left and is creating an evanescent field on the surface of the imaging well. This excites the fluorescence in the flakes of 2D materials, which is detected through the imaging column. The inset on the top left shows the atomic structure of a 2D material (e.g. hBN) with defects. (b) Waveguide chip placed on the piezo stage. The red laser is coupled in from the left facet and its propagation inside the waveguide is visible due to scattering. The scattering signal is significantly higher in the imaging well (outlined in yellow), where the protective top silica cladding is removed. (c) Multiple imaging wells on the same waveguide chip, placed after the expansion taper reached the needed width of the waveguide (25, 50 or 100 μm in the chip shown). (d) An SEM image of transferred CVD-grown hBN flakes inside one of the imaging wells. Scale bar: 5 mm (b), 500 μm (c), 50 μm (d).

sample is placed for imaging (see Fig. 5.1c,d for the optical and SEM micrographs of the well, respectively). Moreover, as discussed above, we preserved the uniform evanescent field in the imaging wells up to 100 μm wide, by adiabatically expanding the fundamental mode from the inverted taper coupler with an expansion rate of less than 1% (schematically shown in Fig. 5.1a).

To use the described waveguide chip, we built a simple and cost-effective upright microscope using readily-available optomechanical components. As shown in Fig. 5.1, the platform consists of a sample holder to immobilize the waveguide chip, which is placed on top of a 3-axis piezo stage used for alignment, a long-distance coupling objective, an excitation source (561 nm or 641 nm laser), a high-NA imaging objective and an sCMOS camera, which collects PL through exchangeable emission filters in between (see Materials and Methods for details). Alternatively, the waveguide chip can be directly imaged on any existing upright microscope with the addition of a coupling objective or a lensed fiber to couple the laser light into the waveguide chip, which is demonstrated in the SI (Fig. S2). The use of a lensed fiber further

reduces the cost and complexity of the platform and is especially beneficial when imaging is performed in vacuum or in a cryogenic environment.

5.1.1 Results and discussion

To demonstrate the capabilities of the platform for the investigation of 2D materials, we transferred CVD-grown molybdenum disulfide (MoS_2) and tungsten disulfide (WS_2) flakes - two of the most often used two-dimensional TMDCs - onto the waveguide chips (see Materials and Methods for details). Monolayers of MoS_2 and WS_2 exhibit bright photoluminescence in the visible range (emission maximum at ~670 nm for MoS_2 and ~630 nm for WS_2) [262–265], due to the direct bandgap of ~2 eV, and possess strong excitonic effects [57], which make them especially attractive for applications in optoelectronics and nanophotonics. Particularly interesting is the ability of such materials to form van der Waals heterostructures with desired functionalities [81, 266].

Though point defects in two-dimensional TMDCs are usually not optically-active at room temperature, they have an effect on the photoluminescence of the material. The PL of TMDCs is normally reduced with the increasing density of defects, thus serving as an indicator of the quality of the 2D material. PL can also be enhanced through defect engineering [74, 255, 267] and chemical treatment [267, 268]. In Fig. 5.2 we show the measured widefield PL signal from MoS_2 (Fig. 5.2a) and WS_2 (Fig. 5.2b) flakes excited by the evanescent field on the surface of waveguide chips, together with their spectra (see Materials and Methods for details). Both materials demonstrate a bright PL signal, compared with the background, even with the excitation laser power as low as 10 mW, measured before the coupling objective. Such power density is orders of magnitude smaller than what is typically needed to illuminate a similar area for PL measurements on conventional widefield microscopes.

Another advantage of the waveguide platform is the fast acquisition time for PL maps. To obtain the PL maps in Fig. 5.2 (~100*100 μm^2) acquisition time of 100 milliseconds was used, which makes a significant difference in comparison with the sequential scanning micro-PL, where typical acquisition times for such large areas are on the order of minutes (1000x slower). This difference becomes even more significant for larger-area flakes (shown in Fig. S3) and continuous films of 2D materials, which are currently under development. An advantage of micro-PL comes from the ability to simultaneously record the spectrum of the photoluminescence, though requiring even longer integration times to achieve a good signal-to-noise ratio. That is why for high-throughput PL analysis spectral characterization capabilities can be further added to the demonstrated waveguide-based platform, e.g. following the approach in Ref. [127].

Upon closer examination of the PL image of the WS_2 flake (Fig. 5.2b), a pronounced dark triangular region can be observed in the center of each flake, which presumably consists of several atomic layers of the 2D material produced during initial growth at the nucleation center. This is further confirmed by the atomic force microscopy (AFM) scan (Fig. 5.2c), which

reveals an averaged line profile with a step of ~1.5 nm at the boundary of the dark region. These multilayer structures exhibit much dimmer photoluminescence due to the change from a direct bandgap in monolayer WS_2 to an indirect band-gap in the multilayer material [269]. Therefore, the waveguide-based platform can be used as well for a quick search of multilayer regions on a grown monolayer 2D material, even in case of poor optical contrast.

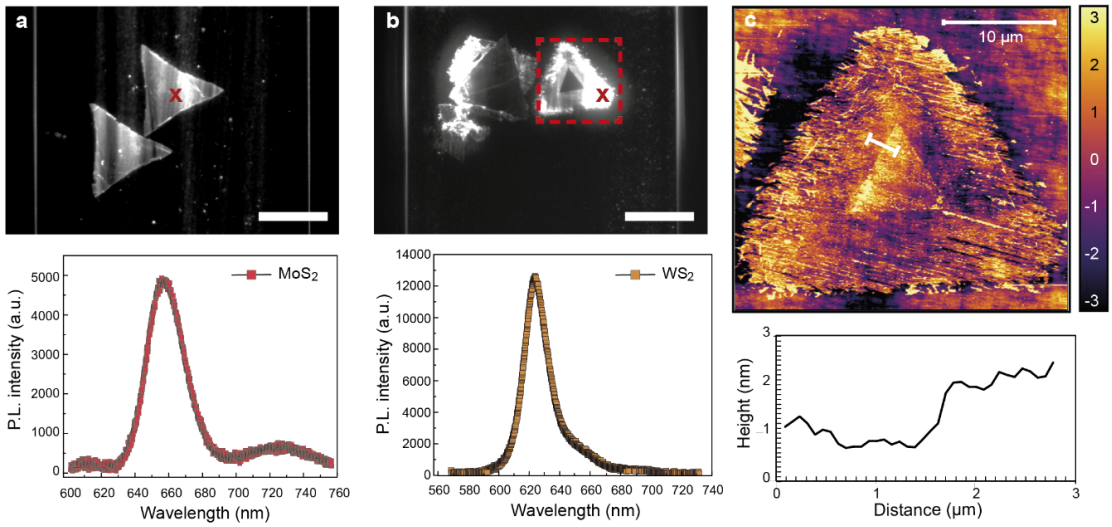

Figure 5.2 – Photoluminescence imaging of 2D semiconductors on waveguides. (a) MoS_2 flakes in the imaging well (top) and the PL spectrum taken at the position of the cross (bottom). (b) WS_2 flakes and their PL spectrum, respectively. (c) AFM scan of dark and bright regions of the WS_2 flake inside the red square and the corresponding averaged line profile (indicated by the width of the line ends), showing a step of ~1.5 nm, corresponding to a multilayer material in the center of the flake. The rough borders of the flake are due to the transfer method used. The stripes seen in (a) are also due to the imperfections in the waveguide and transfer residues, which can disturb the mode profile and create some interference. Scale bar: 25 μm (a, b).

To investigate the capabilities of the waveguide-based imaging platform for super-resolution defect characterization, we transferred samples of CVD-grown monolayer hBN to the imaging wells on a waveguide chip (see Materials and Methods for details). As monolayer hBN on top of silicon nitride is barely visible by either bright- and dark-field optical microscopy, we directly proceeded with the investigation of the transferred flakes using fluorescence. Typically, such CVD-grown hBN contains a substantial density of optically-active defects, so we could excite them using laser illumination, coupled into the on-chip waveguide, and record the emitted signal with an sCMOS camera. A typical time-averaged widefield image clearly shows multiple hBN flakes inside an imaging well in Figure 5.3b.

As was previously reported [130], emitters in hBN exhibit pronounced photoswitching between the bright and dark states (blinking) under continuous laser illumination, such that only a fraction of emitters is visible in each of the acquired frames (see Fig. S6 for the temporal properties of the studied samples). This enables temporal separation and localization of sparse active emitters with sub-pixel precision by fitting each of the diffraction-limited luminescence

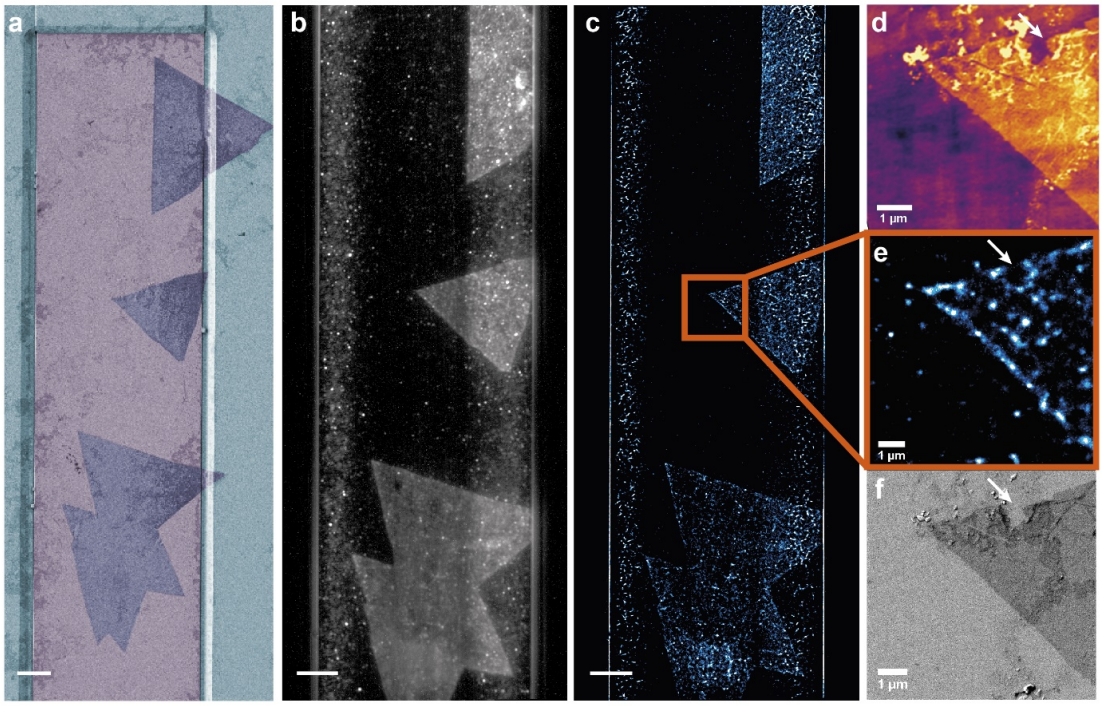

Figure 5.3 – Imaging of optically-active defects in hBN on waveguides. (a) An SEM image showing multiple hBN flakes inside a single imaging well, false-colored for clarity. Si_3N_4 waveguide (violet), SiO_2 cladding (light-blue), hBN flakes (dark blue). A larger area is shown, compared to (b) and (c) to demonstrate that only the parts of the flakes inside the imaging well are excited by the evanescent field. (b) Fluorescent image obtained using 641 nm laser excitation (2'000 frames, averaged). The observed stripes along the edges of the imaging well are due to residues and inherent impurities in the silica cladding [270]. The impurities are activated in the high field intensity regions owing to the curved cross-section of the waveguide [271]. (c) Reconstructed super-resolved image, obtained from the same stack of 2'000 frames. (d-f) Correlative imaging of the ROI, shown by an orange rectangle, with a distinct sub-micrometer feature (AFM, SMLM, SEM). Scale bar is 10 μm (a, c), all images are obtained from a single FOV without any stitching.

spots with a 2D Gaussian intensity profiles and a reconstruction of a super-resolved image by summing up all localizations over a large number of frames (~2'000, in our case). The resulting super-resolved image for the acquired image stack, reconstructed using the ThunderSTORM plugin [249] for ImageJ [272] is shown in Fig. 5.3c. Additional reconstructed images of large-area hBN flakes are shown in Fig. S4.

As reported in Fig. 5.3c, not only hBN flakes produce the fluorescence, especially in the areas near the edges of the waveguide. Presumably, this parasitic signal is due to polymer residues and inherent impurities in the silica cladding [270]. These impurities are excited in the regions of the waveguide where the excitation field intensity is high due to the curved cross-section of the waveguide, which was intentionally fabricated like that to minimize the scattering losses [271]. To see the distinction between such emitters in the background versus the ones in hBN

flakes, we additionally analyzed their temporal dynamics (SI, Fig. S6c). We also analyzed the spectrum of the observed emission to verify it was coming from the optically-active defects in hBN (Fig. S5), which matches the previously published spectra for CVD-grown hBN [130, 273] and is inherently different from the photoluminescence of polymer residues [274].

To further characterize the transferred 2D material on waveguides, we performed scanning electron microscopy (SEM) (Fig. 5.3a) and AFM (Fig. 5.3d) imaging. The strong contrast of hBN on top of silicon nitride in SEM enables relatively quick imaging of sufficiently large areas on the sample to locate all transferred hBN flakes and check for possible polymer residues (visible in areas close to the imaging well in Fig. 5.3a) mainly coming from Poly(methyl methacrylate) (PMMA), used in the transfer process (see Materials and Methods for details). Higher-resolution SEM imaging, followed by AFM scans of the selected regions-of-interest (ROIs), demonstrates the advantages of the waveguide imaging platform for correlative super-resolution imaging (Fig. 5.3d-f), thanks to the natural reference frame of each imaging well and waveguide labels, used to navigate the waveguide chip.

While acquired super-resolved images of emitters in hBN provide valuable information about the spatial and temporal distribution of defects in the transferred flakes, for high-throughput characterization of the material it is important to have a certain figure-of-merit, linked to the properties of the material under study. One such figure-of-merit could be the average density of optically-active defects [130], which would be inversely proportional to the quality of the hBN film in comparison to the defect-free crystal. This information can be easily extracted from the localization table (Fig. S7), used to generate the super-resolved image, which allows for an easy integration into automated characterization procedures.

Furthermore, as both the core and the cladding of the waveguide chip are chemically stable, the platform can be readily used to explore the effect of chemical treatments on the optical properties of 2D materials. One example is the treatment with a super-acid, such as bis(trifluoromethane)sulfonamide, which was demonstrated to increase the photoluminescence of 2D materials [267]. More complicated treatments [275, 276] could be used to heal the defects in CVD-grown 2D materials in an effort to bridge the gap in their quality in comparison to almost defect-free bulk crystals. Moreover, using simple PDMS-based microfluidic channels on top of the waveguide chip, one could image the temporal evolution of such treatments, multiplexed over several waveguides on the same chip.

The waveguide-based platform is also advantageous in the context of further integration with on-chip electronics and microwave circuits. Recent studies have identified certain optically-active defects in hBN, that demonstrate clear signatures of an optically-detected magnetic resonance (ODMR) [122, 123]. This discovery opens up a plethora of possibilities for the optical manipulation and readout of spin states in hBN, which is essential for quantum information processing and quantum sensing algorithms. Thus, the addition of microwave and DC lines becomes a necessity and could be easily achievable on the waveguide chip with standard microfabrication techniques.

5.1.2 Conclusion

We have designed a novel waveguide-based platform for the investigation of defects in 2D materials and demonstrated its high-throughput capabilities for the characterization of optically-active defects in hexagonal boron nitride. We further showed the capabilities of the waveguide-based platform for correlative imaging of defects in 2D materials beyond the diffraction limit. Extending this approach to other types of 2D materials (MoS_2, WS_2), we explored their evanescent-field-driven photoluminescence. Therefore, our approach paves the way towards high-throughput characterization and exploration of defects in various 2D materials both at room temperature and in the cryogenic environment.

5.1.3 Materials and methods

Optical setup

The home-built microscope has two excitation lasers with a wavelength of 64 7nm (CUBE, Coherent) and 562 nm (OBIS, Coherent), which are then coupled into the input facet of the on-chip waveguides using a long-working-distance objective (50x, NA 0.55, Mitutoyo). A dipping imaging objective (Nikon CFI Plan 100XC W, 100x magnification, NA 1.1) is mounted from the top with the help of two connected Z-stages, one for long-travel-range vertical translation (VAP10/M, Thorlabs) and another one for fine micrometer-positioning (LNR25D/M, Thorlabs). The same stages hold a set of removable emission filters (ZT405/488/561/640rpc or ET700/75, Chroma). Another mechanically-stable system, built with four posts and four rectangular optical breadboards, holds the sCMOS camera (PRIME 95B, Photometrics) and the tube-lens (TTL200, 200mm, Thorlabs). Such double mechanical system decouples the vertical motion of the objective from the heavy components and ensures the stability during imaging and quick Z-adjustment.

The waveguide chip is placed in a custom-made holder (3D-printed or micro-machined), which is then screwed into an independent double-stage system, in which the first stage (M-401, Newport) enables the FOV adjustment and the second one (MAX311D/M, Thorlabs) is used to align the entrance of the waveguide with the focused laser beam and maximize the coupling efficiency. A more detailed description of the setup can be found in Ref. [184], together with the complete set of design files.

Chip fabrication

We fabricated channel waveguides with a rectangular cross-section using Si_3N_4 as the core and SiO_2 as the cladding material on standard silicon wafers, 100 mm in diameter and 525 micrometers thick. The core material, stoichiometric silicon nitride (Si_3N_4), 150 nm thick, was deposited using low-pressure chemical vapor deposition (LPCVD) process on top of the 2 micrometer-thick layer of thermally-grown SiO_2 on silicon substrate. To transfer the layout of the waveguides onto the wafer, we used electron-beam lithography, followed by dry reactive

ion etching (RIE). A top cladding layer (2 μm of SiO_2) was deposited by LPCVD (LTO, Low Temperature Oxide). Further photolithography and dry etching steps were used to define the imaging wells. To define the waveguide facets as well as the chip borders two more steps of photolithography and etching were needed to have a spatial separation of the smooth waveguide entrance from the rough chip border. After the deep etching the wafer was grinded from the back till the chips were split apart using the DAG810 automatic surface grinder. The step-by-step fabrication process is schematically shown in SI (Fig. S1) and further detailed in Ref. [184].

2D Material growth

CVD-grown hBN material was produced under similar conditions as described elsewhere55. Briefly, as-received Fe foil (100 μm thick, Alfa Aesar, 99.99% purity) is loaded in a customized CVD reactor (base pressure 1x10-6 mbar). Borazine $(HBNH)_3$ is introduced into the chamber through a leak valve from a liquid reservoir. After growth (45-90 s borazine exposure at $6x10^{-4}$ mbar and 900 °C), the heater is switched off and the foils are slowly cooled in vacuum.

MoS_2 and WS_2 were grown by the CVD process reported previously [257, 277].

2D Material transfer

The as-grown hBN sample was spin-coated with poly(methyl methacrylate) (PMMA, Mr=495, 4% solution in anisole, 3000 rpm) and baked for 5 min at 180°C. The hBN/PMMA layer was lifted-off from the Fe substrate using the electrochemical bubbling method57 and transferred onto the waveguide chips. Similarly, MoS_2 and WS_2 materials, grown on sapphire substrates, were spin-coated with PMMA (Mr=495, 4% solution in anisole, 2000 rpm) and baked for 5 min at 180°C. The MoS_2/PMMA and WS_2/PMMA layers were lifted-off in DI water from the substrate and transferred onto waveguide chips.

The 2D material flakes were precisely aligned into the wells by using a micropositioning stage and a recently reported transfer method [278]. After the transfer, PMMA was removed by a successive 1-hour rinse in hot acetone (3 rinses), hot IPA (1 rinse) and hot DI water (1 rinse). Remaining PMMA contamination is further cleaned by annealing at 400°C in argon (100 sccm) and hydrogen (10 sccm) atmosphere for 8h.

Imaging and data analysis

Imaging was performed using a dipping objective with DI water and an excitation power of the laser varying from 10 to 100 mW. The acquisition time of the sCMOS camera was adjusted to maximize the signal-to-noise without creating overlapping localizations (typically, 50-100 ms). The acquired stacks of thousands of frames were recorded using Micro-Manager [279] and saved as TIFF files. These files were then imported to the ImageJ software [272] and

analyzed using the Thunderstorm plugin [249]. The analysis consisted of applying a wavelet filter to each frame and fitting the peak intensities by 2D Gaussian profiles. Only emitters with intensities at least 1.2 times the standard deviation were then assembled into a localization table, which was used to render the super-resolved image (Normalized Gaussian).

Photoluminescence spectrum

Micro-photoluminescence measurements were performed in air at room temperature. A 50x air objective was used to focus the 488 nm laser on a 2 μm spot on the sample to excite the PL, which was collected through the same objective onto the spectrometer (Andor Newton). Laser power was fixed to 300 μW and 450 μW for MoS_2 and WS_2, respectively. The acquisition time was set to 60 seconds for the spectra shown in Fig. 5.2.

AFM & SEM imaging

The devices were imaged using an atomic force microscope (Asylum Research Cypher) operating in AC mode. The SEM imaging was performed using a ZEISS Leo electron microscope at 1 kV acceleration voltage.

Acknowledgements

We would like to thank LIGENTEC SA and the EPFL Center of Micronanotechnology (CMi) for their help with chip fabrication and the EPFL Laboratory of Quantum Nano-Optics for the assistance with the spectral measurements. E.G. acknowledges the support from the Swiss National Science Foundation through the National Centre of Competence in Research Bio-Inspired Materials. V.B. and S.H. acknowledge funding from the European Union's Horizon 2020 research and innovation program under grant agreement no. 785219.

Supporting Information

Schematic representation of the typical process flow used to fabricate the waveguide chips, adding lensed fibers to an existing microscope to use the waveguide platform, large-area MoS2 flakes on waveguides, hBN flakes on different waveguides, spectra of optically-active defects in hBN, temporal properties of the blinking emitters in hBN and average density of emitters in hBN flakes. This material is available free of charge at https://pubs.acs.org/doi/abs/10.1021/acsphotonics.9b01103.

5.2 On-chip CVD growth of hBN for high-throughput characterization and facile device integration

Characterizing defects in as-grown crystalline materials is a crucial step towards their further use in devices and applications. This is especially true for the rapidly developing field of two-dimensional (2D) materials, where defects in the crystalline structure drastically alter their mechanical, optical, electronic and quantum properties. Typically, such defects are characterized by means of scanning confocal microscopy [95], near-field scanning optical microscopy (NSOM) [144, 147], and atomic force (AFM) [148] or scanning tunneling (STM) microscopies [143, 280]. For the atomically-high resolution of structural defects, transmission electron microscope (TEM) is often utilized [128, 139], however this approach can also induce additional defects in the material under study [140]. The main disadvantage of all these characterization approaches is a small field-of-view (FOV) of up to 100 nm^2, which makes them incompatible with high-throughput wafer-scale processes, crucial for microelectronics and photonics industries.

On the contrary, widefield optical microscopy is routinely used for material characterization purposes, allowing for high-speed inspection, but lacking the nanoscale resolution needed to detect single defects. This disadvantage can be often compensated through the use of various super-resolution microscopy techniques, including single-molecule localization microscopy (SMLM) [204, 205]. SMLM has been recently used for the characterization of optically-active defects in 2D materials [127, 130, 132], in particular those with "blinking" defects (stochastically switching between their ON and OFF states), such as in hexagonal Boron Nitride (hBN). Furthermore, the use of specialized on-chip imaging platforms [184] has drastically increased the throughput of the technique [281].

Defects, however, are not only intrinsic properties of 2D materials, occurring during their growth on a catalytic metal substrate (typically, Cu, Fe, Pt) [88, 282, 283]. Inspection and incorporation of 2D materials into functional or test devices very often requires a transfer step to move the grown 2D material onto the substrate of interest. Naturally, this process might induce additional defects [284] and, in most cases, contamination from the transfer process [278]. During the transfer, the 2D material can also crack, acquire wrinkles and trap tiny air bubbles, all of which unpredictably changes the local stress and influences the optoelectronic properties of its defects [72, 100, 111, 278, 284, 285].

To tackle this challenge, we report here the direct growth of hexagonal boron nitride on silicon nitride-based waveguide imaging chips and demonstrate both confocal and high-throughput widefield characterization of the as-grown material and its optically-active defects, under various imaging conditions. We also compare this approach to the previously demonstrated polymer-assisted transfer process, and show the clear advantage of having an intact material, enabled by the direct growth, particularly in an aqueous environment. We further characterize the obtained 2D material using TEM, electron energy loss spectroscopy (EELS), and Raman spectroscopy, confirming the chemical and structural composition of CVD-grown hBN.

5.2.1 Results and discussion

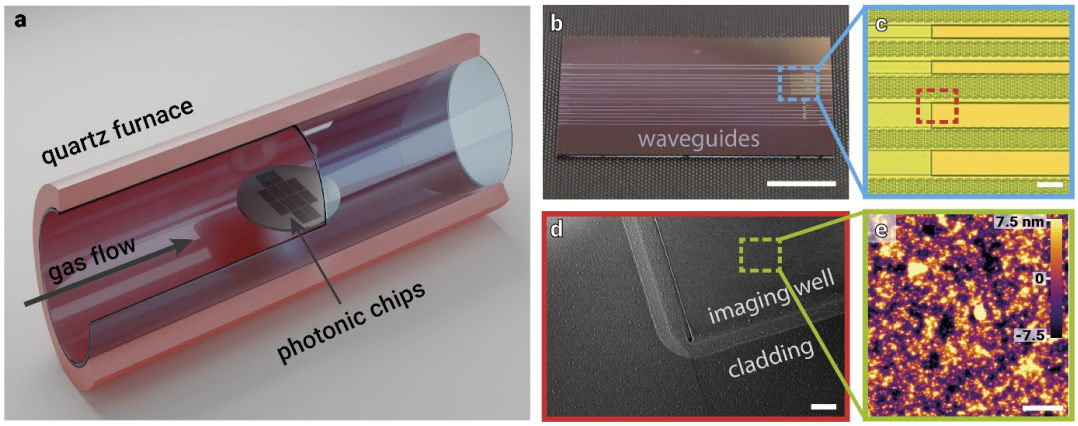

Figure 5.4 – Direct growth of hBN on silicon nitride photonic chips. a) Furnace for CVD growth of few-layer hBN with loaded silicon nitride substrates. b) Single 10x20 mm chip with multiple silicon nitride waveguides, running horizontally across the whole chip. Scale bar: 5 mm c) Optical micrograph of the zoomed-in region from b), showing a number of imaging wells on waveguides. Scale bar: 100 μm d) Scanning electron microscope (SEM) micrograph of a zoomed-in area next to the imaging well (dashed rectangle in c) after the growth. Scale bar: 20 μm e) AFM image of the directly grown hBN film on silicon nitride. Scale bar: 2 μm

We performed a low-pressure chemical vapor deposition (LPCVD) growth of hBN directly on the fabricated silicon nitride waveguides in a quartz tube furnace using ammonia borane as a precursor [109, 286]. The schematic of the CVD reactor is shown in Fig. 5.4a and the detailed description of the growth process can be found in Materials and Methods section below. Waveguide imaging chips were fabricated on silicon wafers using silicon nitride as a core layer and silicon dioxide as top and bottom cladding. Each chip contained several waveguides (Fig. 5.4b) with imaging wells (Fig. 5.4c, d) - areas where protective top cladding was removed to have direct access to the surface of the waveguide core. After extensive cleaning, waveguide chips were loaded into the furnace and left in vacuum overnight. The growth was performed at a temperature of 1200^{o}C for 45 minutes, which resulted in a formation of an hBN film covering the whole surface of the chips [131].

While it is not straightforward to observe the uniformly-grown hBN layer on the optical micrographs (Fig. 5.4b,c), the SEM image (Fig. 5.4d) shows an increased surface roughness after the growth, which is further confirmed by the AFM analysis in Fig. 5.4e and Figs. S1-2 in the Supplementary Information. The grown material has a comparable morphology inside and outside the imaging well, i.e. on crystalline silicon nitride versus amorphous silicon dioxide, which is shown in Fig. S1. The relatively high surface roughness [92] is due to the growth protocol optimized to efficiently incorporate optically-active emitters in hBN (Fig. S3), which results in a uniform, but non-epitaxial growth of the hBN film, confirmed by the Raman and Energy Dispersive X-ray spectroscopy (EDX), and TEM (Figs. S3-S5). Further TEM analysis, including the Electron Energy Loss Spectroscopy (EELS), confirms the structural and

elemental composition of the grown hBN film (Figs. S5,S6).

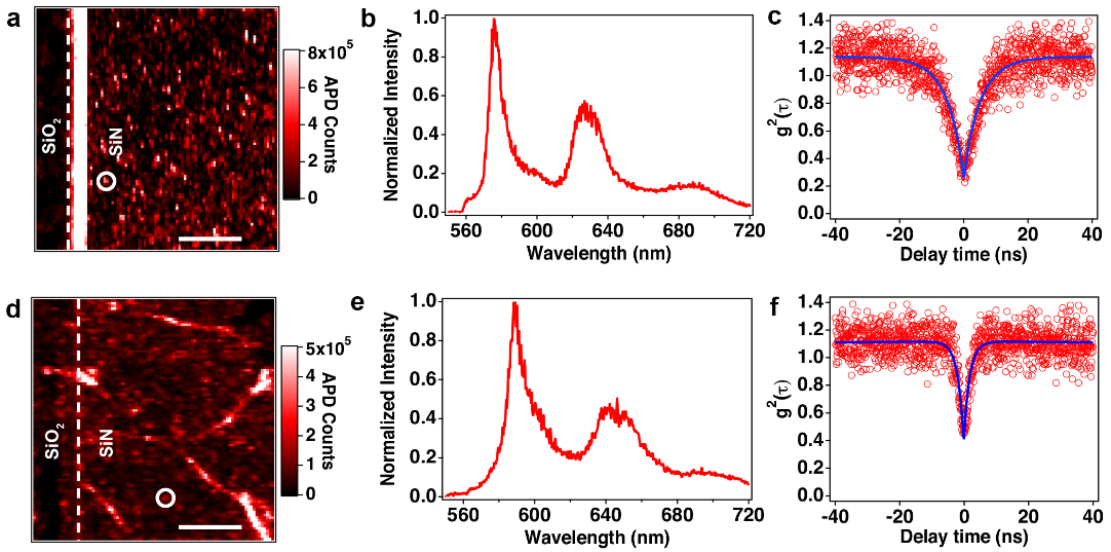

Figure 5.5 – Confocal imaging of directly-grown (a-c) vs transferred (d-f) hexagonal boron nitride. a,d) Confocal scans of the area next to the imaging well. b,e) Representative spectra of one of the inspected emitters from the confocal scans. c,f) Autocorrelation functions for the same emitters, confirming their single-photon nature. The bright lines visible in d) are supposedly transfer-induced wrinkles, possibly containing polymer residues. All measurements were done in air.

Directly after growth, the imaging chips were inspected using a home-built confocal microscope, revealing multiple single-photon emitters (SPEs) in the as-grown material with characteristics similar to the ones reported in literature [109]. The results of this characterization are shown in Fig. 5.5a-c. In parallel, hBN grown via a similar CVD-process on copper foil [109] was transferred onto one of the clean imaging chips using a standard polymer-assisted transfer process [278]. This chip with transferred hBN was inspected as well using the same confocal microscope and the results of its inspection are shown in Fig. 5.5d-f.

On both chips it is possible to identify the characteristic SPEs in hBN in the visible region. Representative spectra, taken in air, in each case (Fig. 5.5b,e) display sharp ZPL lines at 578 nm and 590 nm for the direct growth and transferred samples, respectively. In both cases quantum emission is confirmed via second order autocorrelation analysis displaying $g_2(0)<0.5$ (Fig. 5.5c,f). However, when comparing the two approaches, one can notice the presence of cracks, folds and polymer residues in the transferred hBN and their absence in the as-grown material. Importantly, this has far-reaching consequences for large-area statistical characterization of the optically-active defects in the material, which we further demonstrate using widefield localization microscopy.

Most of the widefield imaging presented further was performed using the custom-built waveguide microscope, schematically shown in Fig. 5.6a and described in detail in Ref. [184]. Importantly, and in contrast to confocal measurements in Fig. 5.5, all widefield characteriza-

tion displayed in Figs. 5.6-5.8 was done in water to explore the charge dynamics of emitters and maximize the achievable collection efficiency and resolution. Briefly, the imaging chips with hBN on top were placed into a custom-made sample holder and the laser light was coupled into the on-chip waveguides using a long working distance objective. The evanescent field of the propagating light excited the optically-active hBN defects on the waveguide surface (inside the imaging wells where the protective cladding has been removed). The excited region of the waveguide is highlighted in Fig. 5.6b by the red rectangle. The fluorescent signal was captured by a separate water-dipping objective and recorded using an sCMOS camera (see Materials and methods for the details of the imaging setup).

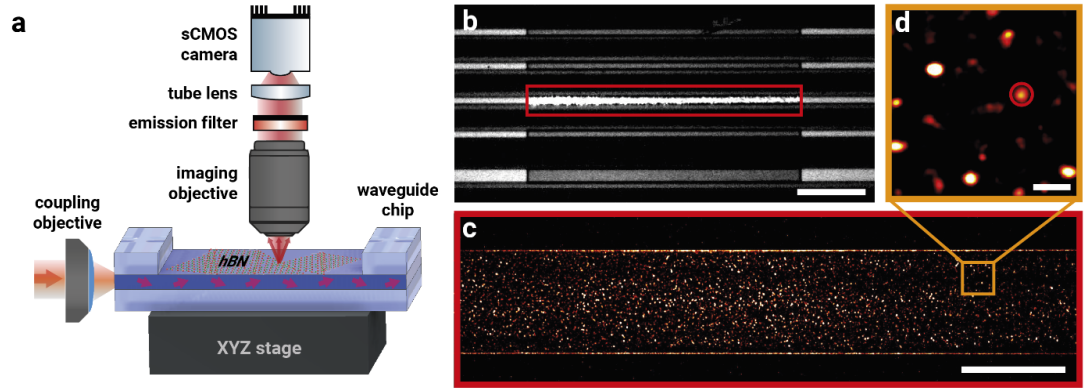

Figure 5.6 – Waveguide-based widefield imaging of optically-active emitters in as-grown hBN. a) Simplified schematic of the waveguide microscope. b) Overview of the imaging wells when the laser light is coupled into one of the waveguides (red rectangle). Scale bar: 250 μm c) Reconstructed image of emitters in hBN inside the imaging well, highlighted in b). Scale bar: 25 μm d) Zoom-in on a region in c), showing individual emitters. Scale bar: 1 μm

While the utilized imaging platform can be used to characterize any type of fluorescent defects, including the optically stable centers, blinking is often observed as a result of emitters interacting with their local environment [130, 132]. This effect is significantly enhanced once the material is immersed in liquid, which is necessary for applications in nanofluidics and biosensing [132, 219, 287, 288]. Moreover, as high-resolution imaging is in general mostly performed in aqueous solutions to compensate for the refractive index mismatch, the induced ON-OFF switching of the optically-active defects allows for their precise spatial localization and attribution of their properties using SMLM techniques [127, 130].

Each SMLM recording consists of several thousand frames, acquired with a typical exposure time between 20 and 100 ms, which are then processed to localize the point emitters and reconstruct the super-resolved image. The result of this process is shown in Fig. 5.6c and one can see a relatively uniform coverage of the surface of hBN in the imaging wells by the optically-active defects. A zoom-in on one of the areas in Fig. 5.6d shows isolated optically-active emitters, with a typical localization uncertainty around 60 nm (Fig. 5.7a). This value is estimated by analysing the distribution of localizations for each emitter, shown in the inset of

Fig. 5.7a.

To further assess the ensemble properties of the optically-active defects, we utilized a spectral super-resolution (sSMLM) technique, providing a combined spatial and spectral information about the localized defects [127]. Such capabilities could be easily integrated into the waveguide microscope by introducing a dispersive prism into the collection path, however here the existing setup with the direct excitation was used. This approach allowed us to see the spectral distribution of the optically-active emitters over the whole FOV, revealing two sets of defects ("green" and "red") activated either by 561 or 647 nm laser illumination, respectively (Fig. 5.7b). These two sets of emitters were previously reported in Refs. [127, 273], where the emission peak around 580 nm is attributed to the zero-phonon line (ZPL) of the most commonly observed defect type [113]. The emission at 610 nm may originate from either the phonon side band of the emitters or additional family of ZPLs, known to occur in as-grown materials [273], while the relative amplitudes of these peaks can be influenced by the emission filters used (50% transmission at 575 nm, in this case). It is important to note here, that the sSMLM technique shows a statistical distribution of spectra across the FOV, so it should be viewed as an averaged overlay of all recorded spectra of isolated emitters.

The third peak in Fig. 5.7b, centered around 670 nm, most probably corresponds to an hBN defect of another type. Its emission is not very pronounced when excited with a green laser (532 or 561 nm), but is significantly enhanced upon excitation with the 647 nm laser. This defect type has been previously reported in Refs. [127, 273] and is observed in both exfoliated and CVD-grown hBN. The spatial distribution of both types of defects is shown in Fig. 5.7c, with little spatial co-localization of the defect sites. This question remains to be further explored on ensembles of defects with varying density. In Fig. 5.7d we have also checked the ON-OFF statistics of defects in as-grown hBN, which has a similar power-law distribution ($P(t) = Ct^{\alpha}$, with $\alpha_{ON} \approx$ -2.0, $\alpha_{OFF} \approx$ -1.5) for both excitation wavelengths, to those reported in literature [127, 281] (see Materials and methods for the details). This graph clearly shows longer average OFF times for both types of emitters, while the power-law dependence hints on the absence of the intrinsic timescales in the blinking behaviour, which can result from photoinduced ionization and charge state transitions due to the charge traps at the surface of the material.

Finally, we compare the optically-active defects in as-grown hBN on the imaging chip to the ones in the hBN film, transferred onto the imaging chip using the PMMA-assisted wet transfer method [278]. We first inspected the samples with both as-grown and transferred material using SEM, which enables quick visualization of possible residues and contamination. Indeed, in Fig. 5.8a most of the contrast on the image comes from the residual polymer film, which is further confirmed by AFM imaging in Fig. S7. Additionally, one can see multiple transfer-induced tears in the transferred hBN film. In contrast to that, the surface of the chip with an as-grown hBN looks clean and smooth (Fig. 5.8c). A closer comparison of the surfaces of two chips is provided by AFM measurements in Figs. S1,S7-8.

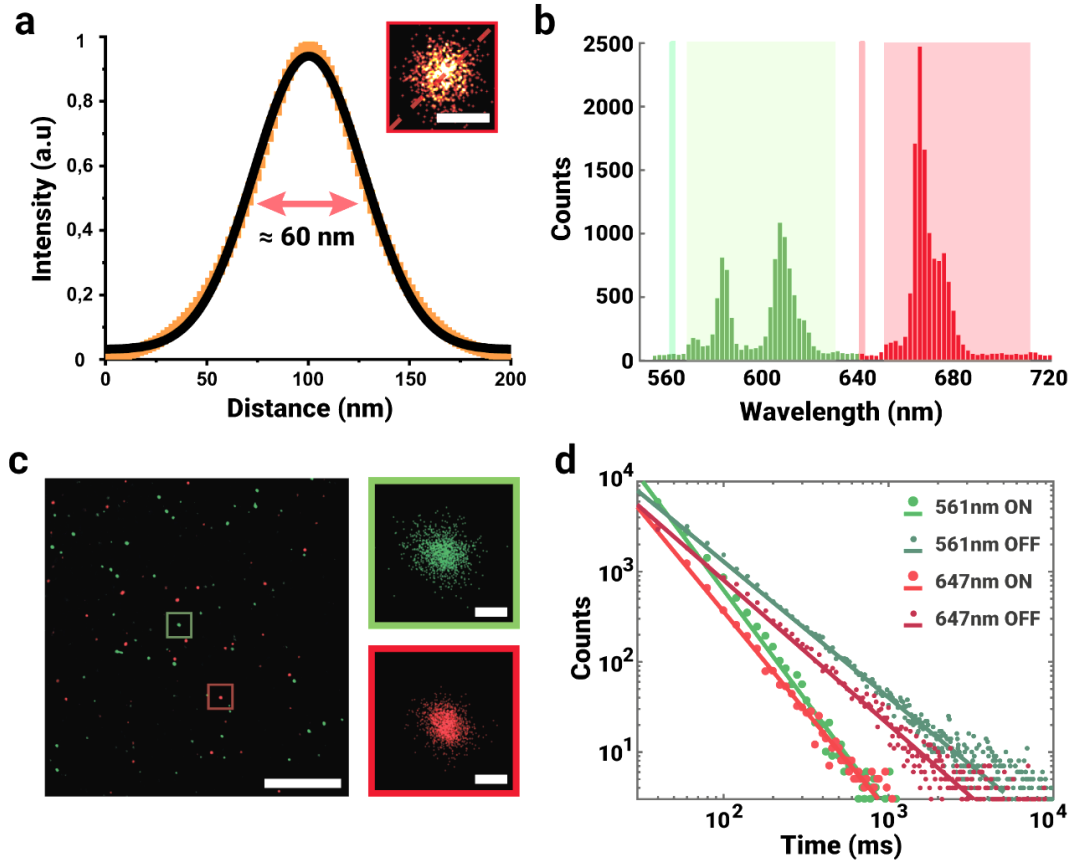

Figure 5.7 – Ensemble properties of optically-active emitters in as-grown hBN. a) Typical Gaussian intensity profile of an individual highlighted emitter in Fig. 5.6d. The inset shows a further zoom-in into the reconstructed image of the localized emitter. Scale bar: 100 nm b) Spectral statistics of emitters in the as-grown hBN, obtained using an sSMLM technique. Semi-transparent lines show the laser excitation wavelengths. Coloured semi-transparent regions represent the transmission bands of the emission filters used. c) The spatial map of two types of emitters, coloured according to their spectra. Scale bars: 5 μm, 100 nm (zoom-ins) d) Temporal statistics of blinking emitters, showing the distribution of their ON and OFF times for two excitation wavelengths (561 nm and 647 nm).

The fluorescence images of the transferred and directly grown hBN further confirm the differences in terms of sample cleanliness between the two approaches. Looking at the imaging wells of waveguide chips in Figs. 5.8b,d, one can see the transfer-induced imperfections and contamination in Fig. 5.8b and their absence in Fig. 5.8d. Contamination-induced fluorescent background also influences the proper localization of emitters by the SMLM algorithm, leading to reconstruction artefacts, which is why we don't display the reconstructed super-resolved image in Fig. 5.8b. On the other hand, the as-grown material shows predominant emission from the isolated optically active defects that exhibit blinking, and the reconstructed super-resolution image can be obtained, as shown at the bottom right of Fig. 5.8d.

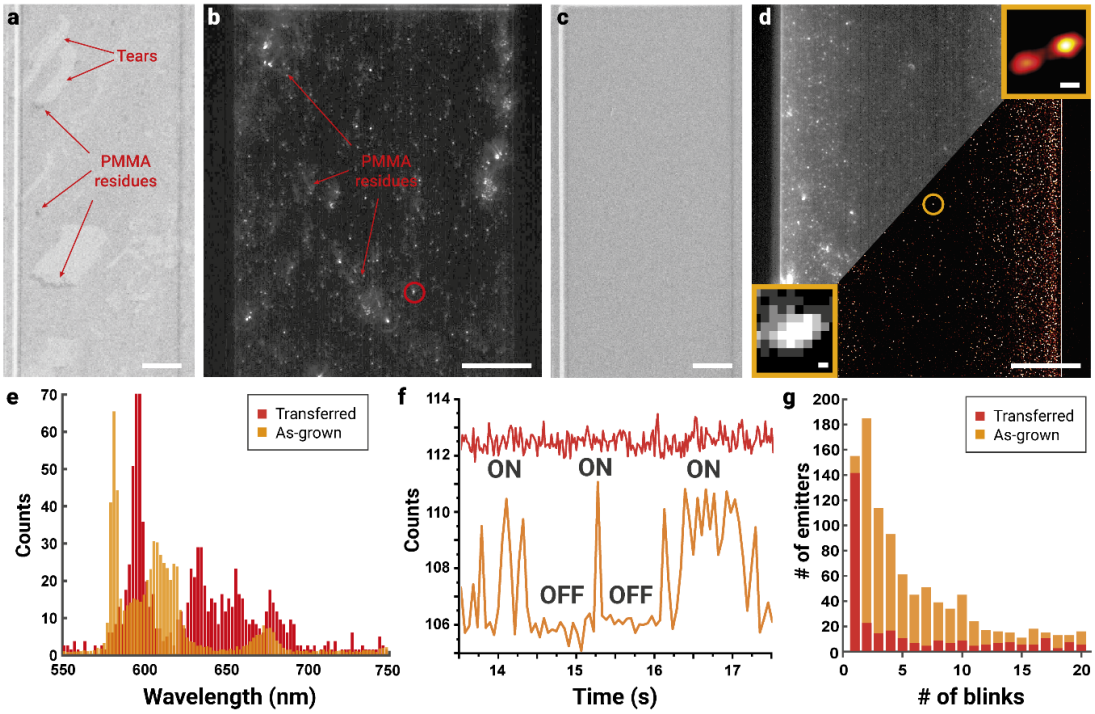

Figure 5.8 – Large-FOV imaging of transferred vs directly-grown hBN. a) SEM micrograph of transferred hBN film inside the imaging well on the waveguide chip. Some of the thicker residues from the PMMA-assisted wet transfer can be seen as darker regions on top of the hBN film with transfer-induced tears. b) Averaged stack of fluorescence images of the area inside the imaging well, obtained using the waveguide-based platform. c) SEM micrograph of the imaging well on the waveguide chip with directly-grown hBN. d) Composite image of the defects in directly-grown hBN. Imaging performed the same way as in b). Top left part shows the averaged stack of fluorescence data, while the bottom right shows the reconstructed super-resolved image. No isolated flakes are seen as hBN uniformly covers the area of the chip. Insets show a zoom-in on a selected emitter. Scale bar: 25 μm (a-d), 100 nm (insets) e) Averaged ensemble emission spectra of the photoluminescence in transferred vs as-grown material, obtained from hundreds of localized emitters from respective samples. f) Temporal intensity traces of the highlighted emitters in b) and d), respectively. g) Whole-FOV temporal statistics of the emitters in b) and d), confirming at the ensemble level the observed temporal dynamics seen in f). All imaging was done in DI water.

To further elaborate on these differences, we studied the spectral and temporal (Fig. 5.8e-g) characteristics of the defects in as-grown and transferred materials. Averaged emission spectra from the ensemble of emitters found on both types of samples, are shown in Fig. 5.8e, demonstrating previously-described ZPLs. The diagram includes any localized emission, irrespective of its source, with a sufficiently small spot size (100 nm $<\sigma<$ 1000 nm). Relatively broader peaks and a higher background for the transferred material can be attributed to the transfer-induced contamination [289]. The spectral measurements were done using an sSMLM setup, described above (see Materials and methods for more information).

Comparing the temporal behaviour of emitters, we found that the ones in the transferred hBN film did not exhibit the typical blinking behaviour in water, in contrast to the emitters in the as-grown material (Fig. 5.8f). This is the case not just for selected emitters, but stays valid for the hundreds of them in more than a 100x100 μm^2 FOV (Fig. 5.8g). Therefore, the super-resolution enhancement was achieved only for the emitters in the as-grown sample, increasing the ability to detect closely-spaced individual defects below the diffraction limit (Fig. 5.8d, insets).

The performed analysis shows the benefits of the widefield SMLM technique for optical studies of fluorescent defects in 2D materials. This is especially true for blinking defects, which can easily go undetected during confocal scanning. Both techniques, however, are complementary to each other and help to properly validate the observed emission patterns. Their co-integration in a single optical setup, together with the capabilities of a large-FOV spectral SMLM, will be a necessary next step to increase the throughput of such optical inspection.

Naturally, growth of 2D materials on dielectric substrates is still far from being defect-free monolayers, but even in the current state the material is already useful for certain applications in nanophotonics. Constant progress in this field renders a CMOS-compatible wafer-scale process reachable in the nearest future. Such process will allow having several dedicated imaging chips per wafer, to characterize the as-grown material, while filling the rest of the wafer with functional devices.

In-situ fast and high-throughput characterization of quantum emitters on waveguides can also accelerate the integration of 2D materials with nanophotonic circuits. To this extent, emitters of choice can be coupled onto the selected on-chip waveguides and addressed through them. This has already been shown with the exfoliated flakes [117], and the possibility of directly growing the 2D materials [94] will largely simplify this process, allowing its CMOS-compatible scale-up.

5.2.2 Conclusions

We demonstrated direct growth of an hBN film on silicon nitride photonic chips. The embedded optically-active defects in the as-grown hBN were characterized using both a standard confocal microscope and a novel large-FOV waveguide-based imaging platform. The latter clearly unveils the advantages of the direct growth approach over PMMA-assisted wet transfer for the integration of hBN with photonic chips. The presented growth method could be extended to wafer-scale devices, diminishing the need for wet transfer of 2D materials that often results in cracks, wrinkles and polymer residues. Our approach paves the way for the future use of CVD-grown hBN in integrated photonics, coupled with high-throughput optical methods for 2D materials characterization.

5.2.3 Materials and methods

LPCVD growth and transfer of hBN

hBN was grown via low pressure chemical vapor deposition (LPCVD) in a tube furnace, using a similar protocol and setup and described in detail elsewhere26. Ammonia borane (Sigma Aldrich) was used as a precursor for growth. Growth was performed for 1 hour at 1200^oC, a pressure of 2 torr, in an Ar/H2 (5%) environment, and the precursor was heated to 95^oC for sublimation. The waveguide substrates were heated to 1200^oC in an Ar/H2 environment and kept at this temperature for 1 hour prior to growth to remove any residual surface contaminants.

hBN films grown on copper were transferred to prefabricated waveguide samples using a PMMA assisted wet-transfer technique [109]. Briefly, PMMA (Microchem A3) was spin coated on the as-grown sample. Copper was etched with a 0.5M ammonium persulfate solution, after which the PMMA/hBN film was washed in water before being picked up on the waveguide sample. Finally, PMMA was removed in warm acetone overnight.

Raman characterization

Raman analysis was performed on an In-Via confocal Raman (Renishaw) system with a 633 nm excitation laser. Spectrometer calibration was performed using a blank Si substrate to 520 cm^{-1}.

Confocal characterization

PL experiments were performed with a lab-built scanning confocal microscope utilizing a continuous wave (CW) 532-nm laser excitation source (Gem 532, Laser Quantum Ltd.). The CW pump laser was passed through a 532 nm line filter and a half-waveplate before focusing on the sample with a high numerical aperture objective (100×, NA =0.9, Nikon). A fast steering X−Y steering mirror (FSM-300) was used for scanning. Light emission was filtered through a 532-nm dichroic mirror (532 nm laser BrightLine, Semrock), with an additional 568-nm long pass filter (Semrock) to fully remove laser light. The sample emission was then collected through a graded-index multimode fiber with an aperture of 62.5 μm, and subsequently directed to a spectrometer (Acton Spectra Pro, Princeton Instrument Inc.) or to two avalanche photodiodes (Excelitas Technologies) in a Hanbury Brown-Twiss configuration for spectroscopy and photon counting measurements, respectively. Time-correlated single photon counting was performed via a (PicoHarp 300, PicoQuant). All $g_2(\tau)$ measurements were analyzed and fit without background correction, and without additional spectral filtering.

TEM characterization

Samples were imaged and characterized by means of transmission electron microscopy (TEM). Images were obtained with 80 kV of accelerating voltage to not induce additional defects into the material. Fig. S5 was obtained using FEI Talos in the high-resolution TEM (HRTEM) mode. Fig. S6 was obtained in the scanning TEM (STEM) mode of a double-C_s-corrected and monochromated FEI Titan Themis in order to perform the electron energy loss spectroscopy (EELS) analysis to measure the bandgap energy and confirm the material composition.

Widefield fluorescence imaging

Imaging was performed using a waveguide microscope described in Refs. 14,15. Briefly, laser light was coupled into the on-chip waveguide using a long-working distance objective (Mitutoyo, 50x, NA 0.55) with a nominal laser power from 50 to 100mW. The excited fluorescence was collected through a dipping objective (CFI Plan 100XC W, 100x magnification, NA 1.1) in DI water and imaged on the sCMOS camera (PRIME 95B, Photometrics). The acquisition time of the sCMOS camera was adjusted to maximize the signal-to-noise without creating overlapping localizations (typically, 50-100 ms). The acquired stacks of thousands of frames were recorded using Micro-Manager [279] and saved as TIFF files.

Super-resolution image processing

The acquired image stacks were imported to the ImageJ software [272] and analyzed using the Thunderstorm plugin [249]. The analysis consisted of applying a wavelet filter to each frame and fitting the peak intensities by 2D Gaussian profiles. Only emitters with intensities larger than the standard deviation were then assembled into a localization table, which was used to render the super-resolved image. The temporal and spectral statistics were analysed in MATLAB. Briefly, the duration of ON and OFF states was calculated for each emitter from the localization table, and their distribution was plotted on the log-log scale (Fig. 5.7d) for two excitation wavelengths. The spectral statistics was acquired following the protocol in Ref. [127]. All processing scripts used are available upon a reasonable request from the corresponding authors.

AFM & SEM analysis

The devices were imaged using an atomic force microscope (Asylum Research Cypher) operating in AC mode. The SEM imaging was performed using a ZEISS Leo electron microscope at 1 kV acceleration voltage. The EDX analysis was done using a ZEISS Merlin electron microscope.

Acknowledgements

We would like to thank LIGENTEC SA and the EPFL Center of Micronanotechnology (CMi) for their help with chip fabrication and the EPFL Laboratory of Quantum Nano-Optics for the assistance with the spectral measurements. We also thank Prof. Suliana Manley for supporting our work and generous access to the microscopy set-up. E.G. acknowledges the support from the Swiss National Science Foundation through the National Centre of Competence in Research Bio-Inspired Materials. I.A. acknowledges the Australian Research Council (CE200100010) and the Asian Office of Aerospace Research 894 and Development (FA2386-20-1-4014) for the financial support.

Supporting Information

The Supporting Information is available free of charge on the ACS Publications website at DOI: https://doi.org/10.1021/acsphotonics.1c00165

AFM image of the directly grown hBN, AFM image of the bare chip, Confocal spectral characterization of the as-grown material, EDX characterization of directly-grown hBN in SEM, Estimating interlayer distance via selected-area FFT of the TEM image, Electron energy loss spectroscopy (EELS) analysis of directly-grown material, AFM image of the transferred hBN film, Line profile from the AFM image of the transferred hBN film.

6 Defects in hBN reveal the complex charge dynamics in aqueous solutions

In this chapter I will show how SMLM-based tracking of blinking defects in hBN helps uncover the complex dynamics of single charges at liquid-solid interfaces in aqueous solutions. This text is the accepted version of the paper

Jean Comtet [1], Benoit Grosjean[2], Evgenii Glushkov[1], Ahmet Avsar[3,4], Kenji Watanabe[5], Takashi Taniguchi[5], Rodolphe Vuilleumier[2], Marie-Laure Bocquet[2] and Aleksandra Radenovic[1] *Direct observation of water mediated single proton transport between hBN surface defects.* **Nature Nanotechnology** 15, 7, 598-604 (2020).

E.G. observed the phenomenon, A.R. and J.C. conceived and designed the experiments; J.C. performed the experiments, with help from E.G. and A.A.; J.C. analyzed data and wrote the paper, with inputs from all authors; B.G. carried out ab-initio simulations, with inputs from R.V. and M.L.B; K.W. and T.T. contributed materials; A.R. supervised the project; All authors discussed the results and commented on the manuscript.

[1]Laboratory of Nanoscale Biology, Institute of Bioengineering, School of Engineering, École Polytechnique Fédérale de Lausanne (EPFL), 1015 Lausanne, Switzerland.

[2]PASTEUR, Département de chimie,École normale supérieure, PSL University, Sorbonne Université, CNRS, 24 Rue Lhomond, 75005 Paris, France.

[3]Electrical Engineering Institute, École Polytechnique Fédérale de Lausanne (EPFL), Lausanne, Switzerland.

[4]Institute of Materials Science and Engineering, École Polytechnique Fédérale de Lausanne (EPFL), Lausanne, Switzerland.

[5]National Institute for Materials Science, 1-1 Namiki, Tsukuba 306-0044, Japan

Proton transport in bulk water is known to occur via the so-called Grotthuss mechanisms [290], whereby protons tunnel between individual water molecules along liquid wires formed by hydrogen bonds. This remarkable transport mechanism, speculated almost 200 years ago explains the anomalous and peculiarly high mobility of hydronium and hydroxide ions in bulk water [291]. At interfaces, the situation is much more complex, with experimental and theoretical efforts pointing to a wealth of effects, ranging from specific proton desorption barrier [292] potentially facilitated by interactions with water molecules [293] and hydrogen bonding [294–296], peculiar charging effects due to water negative self-ion [297], to 2D confinement of protons at hydrophobic interfaces, leading to facilitated lateral transport [298–301]. However, interfacial transport of protons, and its relation with the surrounding aqueous water environment has so far remained elusive, due to the lack of direct measurements at the single molecule scale and in environmental conditions. A finer molecular understanding of proton transport at interfaces would have fundamental importance for a range of fields and materials, from cell membranes in biology [298–301], metallic and oxide surfaces for catalysis and surface science [293, 302–304], to polymeric surfaces for fuel cells [305–309] and membrane science [310–313].

Here, we use single molecule localization microscopy to resolve the transport of individual excess protons between defects at the surface of hexagonal boron nitride (hBN) crystals. Our label-free approach relies on the protonation-induced optical activation of defects at the surface of the flake. Building upon the recent application of super-resolution microscopy to hBN defects [127, 130], we are able to follow spatial trajectories of individual excess protons, through successive hopping and activation of surface defects. We reveal heterogeneous water mediated proton mobility under illumination, with proton transport limited by desorption from individual defects. Our observations demonstrate that interfacial water provides a preferential pathway for proton and charge transport. This finding, along with the chemical nature of the defects in aqueous conditions, are corroborated by full quantum molecular dynamic simulations of pristine and defected hBN/water interfaces. Our findings and observations have general implications for proton transport between titrable surface groups or surface traps, as arising at a variety of biological [298, 300, 314] and solid-state [292, 302, 305, 307, 315] interfaces.

6.1 Reactivity of hBN surface defects in aqueous conditions

As shown in Figure 1a, our sample is composed of multilayer boron nitride flakes, exfoliated from high quality crystals [76]. Such exfoliated hBN flakes are atomically smooth and host very few intrinsic defect sites [316]. Defects are deterministically induced at the surface of the flake through a brief low-power oxygen plasma treatment [127, 317] (SI S1.4). Wide-field illumination of the sample with a continuous green laser (λ_{exc} = 565 nm) leads to localized emission from optically active defects at the surface of the flake, characterized by uniform emission at 585 nm (2.08 eV), consistent with previous reports [127, 239] (*Fig. S1*).

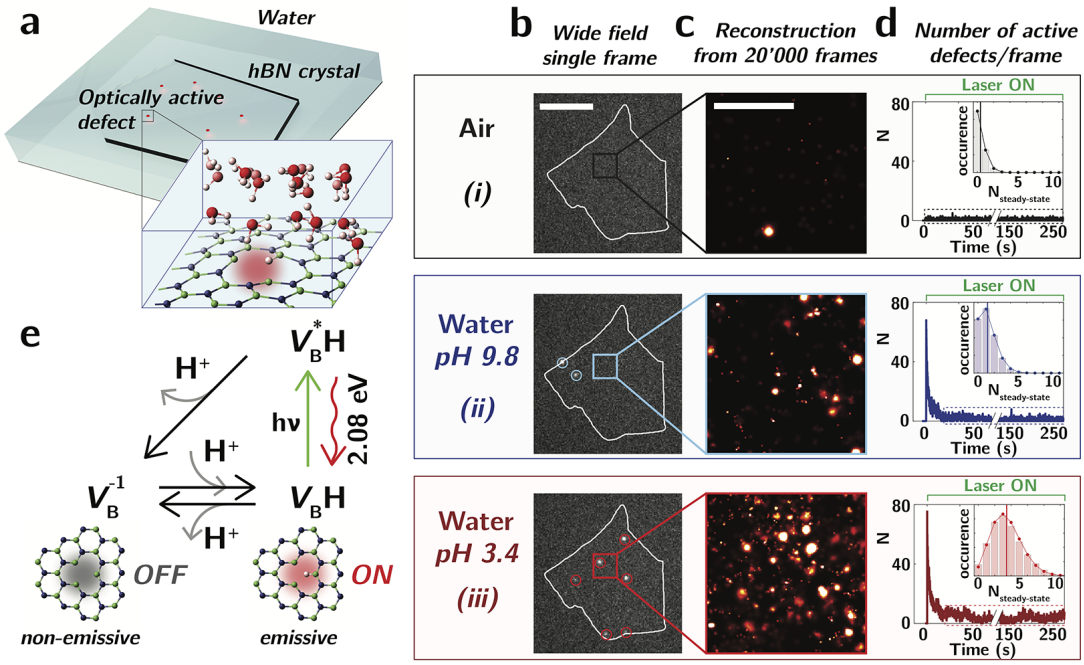

Figure 6.1 – Reactivity of hBN defects in aqueous conditions: protonation activates defects. a) hBN crystal containing irradiation-induced surface defects is illuminated by a continuous green laser, leading to localized emission from optically active defects (red). The crystal can be exposed to various environmental conditions (air or water solutions of varying acidity). Inset: Zoom on a surface defect (protonated boron vacancy $V_B H$), surrounded by water molecules. Boron, nitrogen, oxygen and hydrogen atoms are represented respectively as blue, green, red and white. (b-d) Larger defect reactivity in aqueous acidic conditions, comparing flake in air *(i)*, in basic *(ii, pH 9.8)* and acidic *(iii, pH 3.4)* water solutions. b) Wide field image of an hBN flake, obtained with 20 ms exposure time. Emission from individual surface defects can be localized with ~ 5-40 nm uncertainty (red and blue circles, see SI S1.2). Scale bar: 5 μm. c) Reconstructed super-resolved images of the flake surface (SI S1.3). Scale bar: 1 μm. d) Number N of emissive defects as a function of time for the three environmental conditions. In air, the number of active defects is consistently small. In water, we observe a large number of active defects upon illumination, which decreases to reach a steady-state (dashed box, see SI S2 and Fig. S5 for analysis of the relaxation kinetics). Inset shows the histogram of the number of active defects per frame at steady-state $N_{steady-state}$, fitted by Poisson distributions. Vertical lines in inset show the average number of defects per frame. A larger activity of surface defects is evidenced in acidic conditions, consistent with protonation induced activation of surface defects. e) Three state model for the protonation induced transition between non-emissive negatively charged boron vacancy V_B^-, and emissive neutral protonated boron vacancy $V_B H$, with excited state $V_B^* H$ (Fig. S4).

Remarkably, as shown in Figs. 1b-d, we observe a drastic change in the photoluminescence response of the hBN flake when exposed to air (*i*, black) or to aqueous solutions of varying acidity (*ii* blue; *iii* red, corresponding to pH 9.8 and pH 3.4), pointing to the high reactivity of surface defects in aqueous conditions. 6.1b shows the wide field image of the hBN flake under uniform illumination, with the flake physical boundary highlighted as white contour. For each frame, emission originating from surface defects can be localized with subwavelength uncer-

tainty, with a typical localization uncertainty $\sigma_{LOC} \approx 5-40$ nm, scaling as $\sigma_{LOC} \sim \sigma_{PSF}/\sqrt{N_\phi}$, with $\sigma_{PSF} \approx 150$ nm fixed by the point spread function of the microscope and N_ϕ the number of emitted photons (Fig. 1b, black, blue and red circles, SI S1.2). Consecutive localization of emitters over successive frames (here 20'000) allows us to reconstruct a super-resolved spatial map of the defects at the surface of the crystal [127, 130], with a zoom on a 2x2 μm^2 area shown in 6.1c. We observe in 6.1c that while only few defects are active in air, a large number of defects are homogeneously activated in aqueous conditions (Fig. S9 for super-resolved maps of the entire flake). This difference is also highlighted by monitoring the number N of emissive defects per frame under illumination (6.1d, inset). In air, the number of active defects per frame is consistently low, with $<N> \approx 0.3$ active defects/20 ms. Immersing the flake in water, we observe upon illumination an initially very large number of active defects (here $N \approx 70$, corresponding to $\approx$1 active site/μm^2), pointing to the activation of defects luminescence due to solvent molecules (*Fig. S9*). The number of active defects decreases upon illumination over tens of seconds (Fig. S5), to reach a steady-state, characterized by $<N> \approx 1-4$ active defects/20 ms. Importantly, the luminescent state of defects is recovered over sufficiently long dark periods as well as through successive drying and wetting steps (Figs. S6, S7).

Varying water acidity further allows us to identify environmental protons H^+ as being the chemical species responsible for the activation of defect luminescence. Comparing the two pH conditions in Figs. 1b-d, we indeed observe an increase by a factor of ≈ 2 in the number of emissive defects at acidic pH (6.1d, inset), as well as an increase in the density of activated emitters (6.1c). This monotonic increase in defect's activity in acidic conditions was systematically observed in all investigated crystals over 12 pH units (*Fig. S10*).

To rationalize our observations, we perform ab-initio molecular dynamic simulations of a defective hBN interface in water (6.1a, inset, SI S5 and Supplementary Movie 1). Based on recent simulations on anhydrous bulk hBN defects [137] and high-resolution TEM images of hBN monolayers [130, 318], we probed the reactivity of boron monovacancy complexes in water, namely V_BH (identified as the likely 2 eV emitter [137]), and V_B^- (non-emissive at 2 eV, having a lower acceptor defect state in the gap). Our simulations demonstrate that solvated aqueous protons behave like charge-compensating centers and incorporate easily on the negatively charged defect V_B^-, through $V_B^- + H^+ \Rightarrow V_BH$, consistent with the large activation of luminescence observed in the aqueous environment.

These numerical observations allow us to propose the phenomenological three-state model, depicted in 6.1e. In the absence of illumination, the number of protonated defects is fixed by acid-base equilibrium $V_B^- + H^+ \Leftrightarrow V_BH$. Probing this equilibrium experimentally, we determine a pKa $\geq$ 14, consistent with the strong basicity evidenced by the simulations (*Fig. S8*). Upon illumination, defects in the protonated state are converted to their excited state V_B^*H, from which they can either radiatively decay back to the ground state V_BH, or lose their protons to be converted back to V_B^-, through an excited state proton transfer [319] (Fig. S4). This second non-radiative pathway leads to the initial decrease of the number of active defects upon illumination (6.1d and Fig. S5) by effectively shifting the chemical equilibrium between

V_B^- and V_BH, reaching a second steady-state level under constant laser illumination. This photoacidic behavior is consistent with the relative excited state energy levels of the protonated and deprotonated defect [137] (Fig. S4). Consistently, a decrease in the number of active defects at steady-state is observed for increasing illumination power (*Fig. S11*). While reported here for the first time for defects in hBN, this ON/OFF transition between distinct protonation states is commonly observed for fluorescent dyes [320, 321]. Note finally, that while our observations and ab-initio simulations are consistent with the V_BH/V_B^- transition between emissive and non-emissive states, other types of defects with nitrogen dangling bonds and distinct protonation states could also be responsible for these observations.

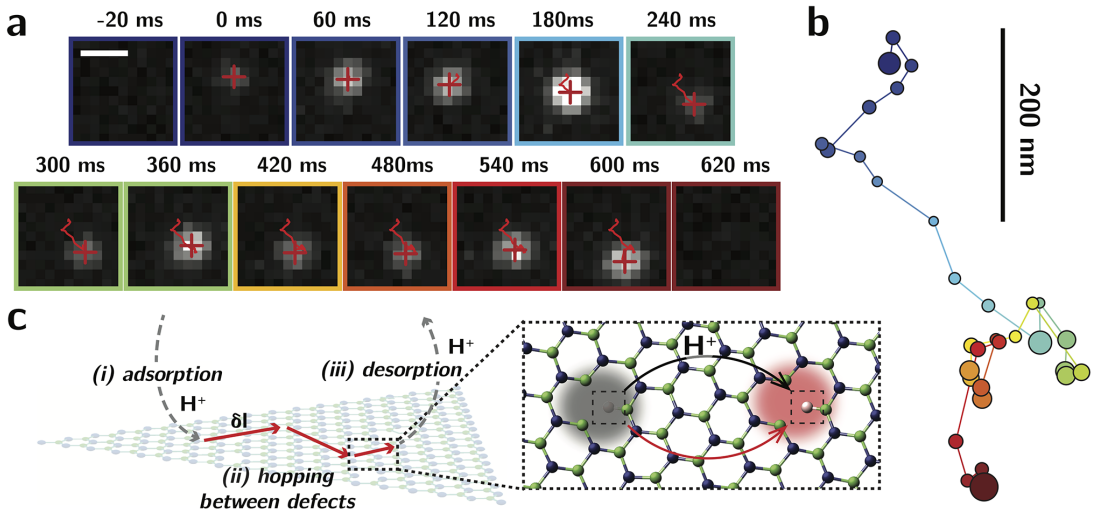

Figure 6.2 – Luminescence migration reveals proton trajectories. a) Time series for spatial migration of luminescence at the surface of the flake, with wide field images showing localized diffraction-limited spot at the surface of the flake (red cross) and reconstructed spatial trajectory in red (Supplementary Movie). Scale bar: 500 nm. Projected pixel size is 100 nm. b) Reconstructed trajectories showing successive activation of adjacent defects at the surface of the flake and color-coded with increasing time. Localized defects are represented as dots, with radius corresponding to localization uncertainty. c) Schematic depicting luminescence migration events, consisting of successive *(i)* proton adsorption (appearance of a luminescence spot at the surface of the flake) *(ii)* excess proton hopping between surface defects (diffusion of the luminescence spot) and *(iii)* proton desorption from the surface of the flake (disappearance of the luminescence spot).

6.2 Luminescence migration reveals proton trajectories

Since the defects are emissive in their protonated form, monitoring luminescence events at the flake's surface allows us to directly track down the spatiotemporal dynamics of defects protonation. 6.2a shows the temporal evolution over 600 ms of the luminescence in a 1x1 μm^2 region at the surface of a flake immersed in DI water (pH ~ 5.5), with subpixel localization of the emitter's position shown as the red cross. As highlighted in this sequence of images, a

single diffraction-limited luminescence spot spatially wanders between successive frames over a total distance of ≈ 500 nm. Consecutive localizations allow us to reconstruct the position of successively activated defects, shown as the red line trace in 6.2a and the reconstructed trajectory in 6.2b, with radius corresponding to uncertainty in localizations. The observation of the consecutive activation of luminescence of nearby defects over 30 successive frames, points to the presence of a single activating excess proton, hopping from defects to defects (6.2c, inset) and leading to the observed spatiotemporal activation of luminescence. Importantly, monitoring defect activation over the whole flake allows us to discard artefacts in these observed trajectories related to stage drift or random activation of emitters (Figs. S14 and S15). As schematically represented in Fig. 6.2c, this observed sequence of correlated luminescence events must then corresponds to *(i)* the adsorption of a proton at one defect's site, leading to the appearance of a luminescence spot at the flake's surface (6.2a, t = 0 ms) followed by *(ii)* the hopping of the excess proton between nearby surface defects over the total residence time T_R, with successive hopping length δl and *(iii)* the desorption of the proton from the flake surface, leading to the extinction of luminescence (6.2a, t = 620 ms). Importantly, we demonstrate through simulations that such correlated luminescence events and trajectories cannot stem from the random activation of emitters at the surface and must correspond to the correlated transfer of a single excess proton between defects (SI S3.4). Following the three-state model of 6.1e, the variation in luminescence intensity observed between successive frames could stem from fluctuations between radiative and non-radiative recombination of the excited defects, e.g. due to transient proton unbinding and geminate recombination. Albeit in a different context, the concepts presented here for single proton tracking are similar to strategies explored in single molecule and single enzyme catalysis [322–324].

These correlated proton trajectories occur consistently and repeatedly upon constant illumination (Supplementary Movie 2). We track and analyze their dynamics using standard single particle tracking techniques [325], focusing on the steady-state regime with a constant averaged density of active defects per frame of ≈0.1-1 per 10 μm^2 (6.1d, dashed boxes). Individual trajectories are defined by correlating localizations less than ~300 nm apart between successive time frames. This threshold is rigorously defined by measuring the statistics of hopping length δl (Fig. S13). Importantly, this tracking methodology is robust with respect to the correlation length and sampling time and is validated against simulations of random activation of emitters (Fig. S14). As shown in 6.3, ≈ 1700 individual trajectories longer than 200 ms (10 successive frames) can be successfully identified over 180 s (Supplementary Movie 2). Representative trajectories are highlighted in 6.3a-c (see also Fig. S19 and Supplementary Movies 4-8). Remarkably, a large heterogeneity is observed between distinct trajectories at the single molecule scale. Some excess protons remain at a fixed position (a), while others migrate over up to 1 μm (6.3, (b-c) and Fig. S19). Long adsorbing steps (40-100 ms) within one uncertainty-limited defect, separated by relatively long hopping events (50-200 nm) are also observed in some trajectories (red dashed circles, (c)). For each individual trajectory, we can compute the associated Square Displacement $\mathrm{SD}(t) = \langle (X(t) - X(t=0))^2 \rangle$ which characterizes the diffusive character of these random walks. From the initial increase of the square

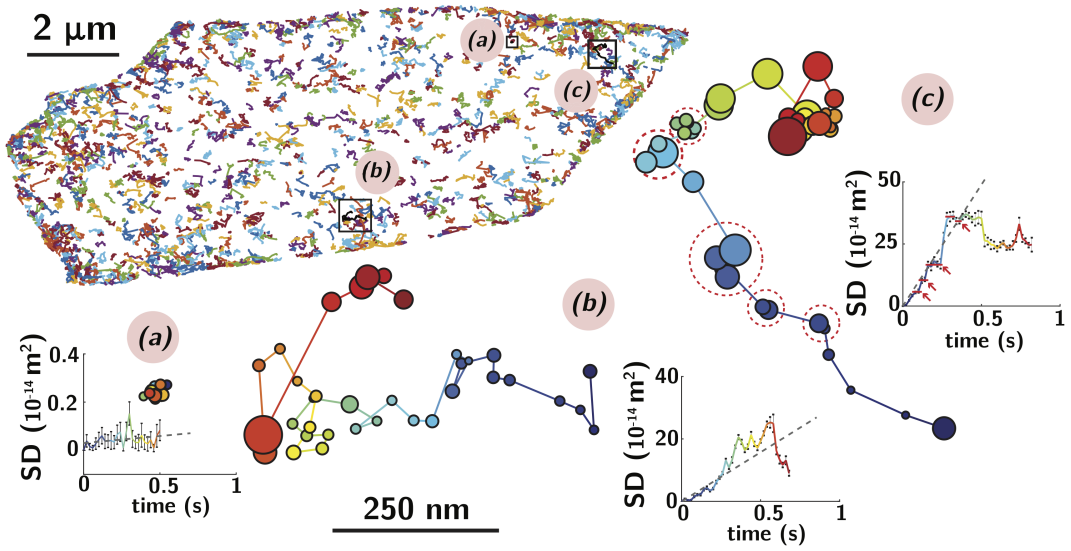

Figure 6.3 – Large-scale mapping of proton trajectories. Trajectories longer than 10 frames (200 ms) measured at the surface of the flake. (a-c) Highlighted representative trajectories, with the corresponding evolution of the mean square displacement MSD (Supplementary Movies 4-6). Defect positions are rendered as circles with radius corresponding to the localization uncertainty. SD is square displacement. Black dashed line is a linear fit of the SD for the first 300 ms. In *c)*, dashed red circles in trajectory and red arrows in SD show adsorbing steps at some defect sites.

displacement with time, one can extract a diffusion coefficient D for each individual trajectory, as $SD = 4.D.t$ (dashed line in the SD graphs), which is found to be respectively $D_{a)} \approx 10^{-16}$ m^2s^{-1} (no diffusion), $D_{b)} \approx 25 \cdot 10^{-14}$ m^2s^{-1} and $D_{c)} \approx 8 \cdot 10^{-14}$ m^2s^{-1}. Note the larger number of observed trajectories at the edges might be due to a larger density of defects (see Fig. S27).

6.3 Interfacial mobility and desorption-limited transport

As shown in 6.4a, we characterize the interfacial mobility of protons at the surface of the flake through the evolution of the Mean Square Displacement MSD averaged over all observed trajectories (the averaged MSD = $< (X(t) - X(t=0))^2 >$ is a well-defined quantity, independent of sampling time and tracking parameters, see SI S3). As shown in 6.4a, the MSD follows an initial linear increase, characteristic of a standard diffusive behavior at short times ($t < 300$ ms), followed by a sub-diffusive behavior at longer times, possibly due to longer adsorbing events at some defect's sites. The linear regime allows us to define the average diffusion coefficient D = 2.8x10^{-14} m^2s^{-1} and typically found of the order of 10^{-14} m^2s^{-1} for the majority of flakes. We further show in the inset the broad distribution of diffusion coefficients from individual single-molecule trajectories, with a significant proportion of trajectories characterized by no net observed motion ($D < 1.10^{-16}$ m^2s^{-1}, as in 6.3*a*). In order to analyze in more details the statistics of these bi-dimensional proton walks, we plot respectively in Figs. 6.4b,c the distribution of hopping length δl and residence time T_R at the surface (calculated as T_R =

$N_R \Delta t$, with N_R the trajectory length in frames and Δt = 20 ms the sampling time). Those distributions are well approximated by power laws $N(\delta l) \sim \delta l^{-\nu}$ and $N(T_R) \sim T_R^{-\mu}$, with here $\nu \approx 2.6$ and $\mu \approx 1.6$, and which are found typically in the range $\nu \in [2.4-4]$ and $\mu \in [1.6-2.5]$ (Fig. S13). The power law scaling for the jump length δl is reminiscent of Levy-type processes [326, 327], and demonstrates the anomalous non-Brownian character of these hopping events, due to the finite distance between randomly distributed defects (defect density on this flake can be estimated to be at least 500 μm^{-2}, leading to an averaged inter-defect distance of 40 nm). The power-law scaling of the residence time naturally arises from the length of a diffusion-controlled escape process, and is larger than for normal diffusion, for which $\mu = 1.5$. Importantly, a large fraction (~70%) of protons remains on the flakes' surface between each frame, leading to trajectories which are subsequently analyzed (Fig. S20).

The orders of magnitude difference between the measured diffusion coefficient $D \approx 10^{-14}$ m^2/s for proton surface transport and the hydronium diffusion coefficient in the bulk [315, 319, 328] $D_{bulk} \approx 10^{-8} - 10^{-7}$ m^2/s and at biological membranes [299–301] $D_{membrane} \approx 10^{-11} - 10^{-9}$ m^2/s suggests the presence of a strong rate-limiting step for interfacial proton transport. We thus compare the surface transport of the two isotopes - hydrogen and deuterium (6.4d, comparing transport in H_2O and D_2O in a distinct flake, see also Fig. S22). As shown in 6.4d, diffusion is hindered in D_2O by at least a factor of 4 compared to H_2O. This isotopic hindrance to diffusion is larger than the factor 1.5 to 2 that one would expect from hindrance of either Grotthuss-like proton transfer or self-diffusion [329, 330], pointing to desorption from defects rather than transport between nearby defects as the rate-limiting step for excess proton transport. Such desorption-limited transport is consistent with the low value of the interfacial diffusion coefficient, the large distribution in diffusion coefficients observed in individual trajectories (6.4a, inset), as well as the long adsorbing steps evidenced at some defects' sites (6.3, trajectories *a* and *c*). Note finally that this hindered desorption-limited transport validates *a posteriori* the choice of our spatiotemporal resolution ($\Delta t = 10-20$ ms and $\Delta l = 300$ nm) for which the largest measurable diffusion coefficient is $\Delta l^2/4\Delta t \sim 10^{-12}$ m^2/s. This value, despite being smaller than the bulk hydronium diffusion coefficients, remains two orders of magnitude larger than the desorption-limited interfacial diffusivities, allowing us to consistently measure and characterize the hindered interfacial proton transport between defects (SI S3). Additional characterization of the proton transit time between defects (corresponding to unhindered interfacial proton transport) would require at this 100 nm scale a temporal resolution $\delta t \approx 1$ μs, unreachable even with state-of-the-art single molecule tracking techniques [331].

Based on these insights, we can, for desorption-limited transport, express the diffusion coefficient as $D = \frac{1}{4}\Gamma a^2$, with Γ [s^{-1}] a jump rate and a the characteristic jump length between nearby defects. This jump rate scales as $\Gamma \sim \nu \exp\left(\frac{-\Delta F}{kT}\right)$, with ν [s^{-1}] a molecular frequency and ΔF a free energy desorption barrier from the defect [332]. As an order of magnitude estimate, we take the attempt frequency as $\nu \sim 1/\tau$ with τ of the order of nanoseconds corresponding to the excited state lifetime [95] (Fig. S2) and $a \approx 10-100$ nm, leading to a typical desorption energy barrier of 16-20 $k_BT \approx$ 0.4-0.5 eV. As shown in 6.4e, we indeed observe

an increase in proton mobility with increasing temperature, from which we extract a mean activation energy $\Delta E \approx 0.62 \pm 0.12$ eV, demonstrating the predominantly enthalpic nature of this free-energy barrier (Fig. S28). This barrier then characterizes the energy necessary to break the NH covalent bond from the excited defect $V_B H^*$ and for the solvated H^+ to escape the electrostatic attraction of the negatively charged vacancy V_B^-. Consistently, this barrier is much smaller than the hydrogen removal energy > 2.34 eV predicted to break the NH bond from the $V_B H$ defect in gas phase [137], as the proton desorption barrier might be reduced here by the presence of nearby hydrogen accepting water molecules, as well as by the laser irradiation. Indeed, we did not observe any proton mobility in air (Fig. S26), despite the presence of adsorbed water at the flake surface in ambient conditions (40% relative humidity), demonstrating the crucial role of bulk water in mediating proton mobility at the flake's surface and consistent with recent simulations [295]. Desorption-limited transport is furthermore confirmed by the weak dependence of mobility on illumination power (Fig. S21). Furthermore, as shown in Figs. S23-S24, the presence of salt and dissolved gas does not affect significantly the interfacial proton mobility, while we observed in a majority of flakes a net increase in mobility at low pH (Fig. S25), consistent with increased defect activity and change of surface state. Finally, we note that the high purity and atomic flatness of the hBN surfaces should also lead to reduced probability of proton trapping at non-emissive sites, allowing the direct observation of excess proton transport between nearby defects.

6.4 Proton charge segregation at the solid/water interface

The emerging picture is thus that of a desorption-limited transport of protons between surface defects, mediated by interfacial water. While several experiments have reported evidence for interfacial proton mobility at surfaces through ensemble measurements [298–301, 333], the trajectories observed here at the flake's surface (Figs. 6.2, 6.3) represent the first direct observation at the single-molecule scale of the interfacial segregation of proton excess at the solid-water interface, demonstrating that interfacial water provides a preferential pathway for charge transport. Indeed, in the absence of any free-energy barrier trapping protons at the interface, a proton desorbing into the bulk would irreversibly diffuse over $\delta l \sim \sqrt{D_{\text{bulk}} \cdot \delta t} \approx$ 300 μm during the $\delta t = 20$ ms sampling time, preventing any correlations in the activation of defects ≈100 nm apart. The power-law tail of the surface residence time (6.4c), concomitant with the finite diffusivity (6.4a) accordingly demonstrates the large probability of near-surface charges to remain segregated and mobile at the surface. In-plane proton transport at the flake surface (6.2b, step *ii*) must thus be favored compared to irreversible proton desorption into the bulk (6.2b, step *iii*), due to the presence of an interfacial free-energy barrier leading to segregation of the excess protons at the hBN/water interface.

To probe the segregation of interfacial protons in more detail, we simulated the dynamics of a hydronium ion at the interface of water and pristine hBN (6.4f). As observed in this 20 ps trajectory (Supplementary Movie 9), the hydronium ion indeed remains segregated (physisorbed) at the interface, while keeping high latteral mobility through Grotthus transfer, with a lateral

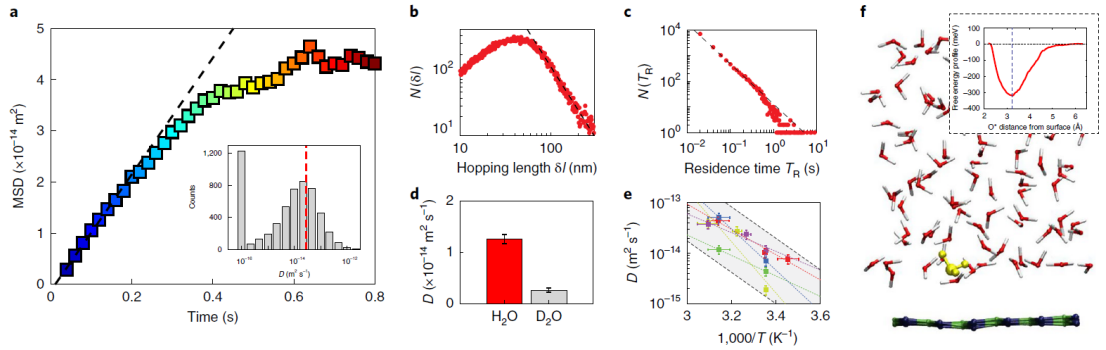

Figure 6.4 – Mobility and segregation of protons at interfaces. a) Variation of the averaged mean square displacement MSD as a function of time for the flake in 6.3. Dashed line is a linear fit from which we extract the averaged diffusion coefficient $D = 2.8\text{x}10^{-14}$ m^2s^{-1}. Inset shows the distribution of the diffusion coefficient determined on individual trajectories, with vertical dashed line the averaged diffusion coefficient. b) Distribution of step length δl between successive jumps. Dashed line is power-law fit with exponent $\alpha \approx 2.6$. c) Distribution of residence time T_R. Dashed line is power-law fit with exponent $\mu \approx 1.6$. d) Isotope effect, comparing diffusion coefficient in D_2O and H_2O in a distinct flake. Error bars represent standard deviation in diffusion coefficient. e) Variation of diffusion coefficient as a function of inverse temperature for 5 distinct flakes, with linear fits shown as dashed colored lines. Black dashed lines are visual guides showing activated Arrhenius behavior with the mean activation energy of 0.62 eV (see Fig. S28). f) Simulation snapshot of the trajectory of an aqueous hydronium ion physisorbed at the pristine hBN/water interface (See Supplementary Movie 9). Inset shows the computed free energy profile of the hydronium ion as it approaches the hBN layer, with a physisorption well of -0.3 eV centered around the maximum of water density at 3.3 Å (blue vertical dotted line in inset, see SI S5).

diffusion coefficient $D \approx 8.10^{-9}$ $m^2.s^{-1}$, close to the bulk hydronium diffusion coefficient [291, 319, 328] $D_{\text{bulk}} \approx 10^{-8} - 10^{-7}$ m^2s^{-1}. As shown in the inset of 6.4f, the computation of the free-energy of the aqueous hydronium approaching a pristine hBN surface further confirms the presence of an interfacial -0.3 eV physisorption well (SI S5). Mechanistically, several effects can be invoked to explain the observed affinity of protons to interfaces. First, in hydronium ions, assymetric charge distribution leads to an amphiphilic surfactant-like character [301, 334], which could lead to segregation due to the hydrophobic nature of the hBN interface. Second, the ionic nature of the insulating hBN crystal [335] could also be responsible for electrostatic trapping of the positively charged hydronium ion. Third, as hydronium donates three hydrogen bonds to water it leads to straining and disruption of the hydrogen bonding network [336]. This effect is reduced at interfaces - at which the hydronium oxygen tend to point away from water[48]- and could lead to trapping of the ion [299, 301, 333, 336]. These simulations suggest that surface transport is characterized by purely bidimensional diffusion at the solid/water interface. In our experiments, measuring whether interfacial proton transport indeed corresponds to purely bidimensional diffusion would require detailed analysis of the statistical properties of the proton transit time between adjacent defects. At this 100 nm scale, such measurements would require a temporal resolution of $\delta t \approx 1$ μs, unfortunately

unreachable even with current state-of-the-art single molecule tracking techniques [331].

6.5 Conclusion

The combination of super-resolution microscopy and single particle tracking on hBN defects allowed us to reveal proton trajectories between adjacent surface defects at the single-molecule scale. These observations establish that interfacial water provides a preferential pathway for proton transport, with excess proton remaining segregated at the hBN/water interface, leading to the observed spatiotemporal correlations in the activation of nearby defects. The direct observation of this interfacial proton pathway has broad implications for charge transport in a range of fields and materials, and suggests to tune defects' densities, binding affinities and illumination to optimize and control interfacial proton transport. Our experiments thus represent a promising platform for the investigation of proton transport at the single molecule scale, opening up a number of avenues, e.g. related to the interplay of flow or confinement with molecular charge transport at liquid/solid interfaces.

Acknowlegment

JC acknowledges valuable discussions with Adrien Descloux and Vytautas Navikas. This work was financially supported by the Swiss National Science Foundation (SNSF) Consolidator grant (BIONIC BSCGI0_157802) and CCMX project ("Large Area Growth of 2D Materials for device integration"). E.G. acknowledges support from the Swiss National Science Foundation through the National Centre of Competence in Research Bio-Inspired Materials. The quantum simulation work was performed on the French national supercomputer Occigen under the DARI grants A0030807364 and A0030802309. MLB acknowledges funding from ANR project Neptune. K.W. and T.T. acknowledge support from the Elemental Strategy Initiative conducted by the MEXT, Japan and the CREST(JPMJCR15F3), JST.

Supplementary information

Supplementary information is available in the online version of the paper at the following address: https://doi.org/10.1038/s41565-020-0695-4

7 Focused Ion Beam enables surface defect engineering in hBN

After exploring the properties of intrinsic and randomly-induced hBN defects, we transition to deterministic engineering of such defects in pre-defined locations. This chapter reviews the current research attempts in this direction, with a particular emphasis on using focused ion beams for this task, and offers a deeper understanding of ion beam interactions with hBN. The text of the chapter is based on the preprint version of the paper

Evgenii Glushkov[1,+,*], Michal Macha[1,+], Esther Rath[2], Vytautas Navikas[1], Nathan Ronceray[1], Cheol Yeon Cheon[3], Ahmed Aqeel[4], Ahmet Avsar[3,5], Kenji Watanabe[6], Takashi Taniguchi[6], Ivan Shorubalko[7], Andras Kis[3], Georg Fantner[2], and Aleksandra Radenovic[1] *Engineering optically active defects in hexagonal boron nitride using focused ion beam and water.* **(in review)** (2021).

A.R., E.G. and M.M. conceived and designed the experiments; E.G., A.A. and C.Y.C. prepared the samples and M.M. performed the FIB irradiation; E.R. did the AFM measurements, helped by N.R. and C.Y.C. E.G. performed the optical measurements with help from V.N. and A.A.; M.M. did the TEM measurements; E.G, V.N. and N.R. analyzed the data; K.W. and T.T. contributed materials; I.S. helped with interpretation of results; E.G. wrote the paper, with inputs from all authors; A.K., G.F. and A.R. supervised the project; All authors discussed the results and commented on the manuscript.

[1]Laboratory of Nanoscale Biology, Institute of Bioengineering,
[2]Laboratory of Nano-Bio Instrumentation, Institute of Bioengineering,
[3]Laboratory of Nanoscale Electronics and Structures, Electrical Engineering Institute and Institute of Materials Science,
[4]Laboratory of Quantum Nano-Optics, Institute of Physics, Ecole Polytechnique Federale de Lausanne (EPFL), Lausanne, Switzerland.
[5]School of Mathematics, Statistics and Physics, Newcastle University, Newcastle upon Tyne, NE1 7RU, United Kingdom.
[6]National Institute for Materials Science, Tsukuba, Japan
[7]Laboratory for Transport at Nanoscale Interfaces, Empa – Swiss Federal Laboratories for Materials Science and Technology, Dübendorf, Switzerland

7.1 Introduction

Optically-active defects in van-der-Waals (vdW) materials have attracted a lot of attention recently, finding applications in the fields of nanophotonics, quantum sensing and nanofluidics [16, 60, 83, 84, 337]. In particular, hexagonal boron nitride (hBN) has emerged as a promising material platform, hosting a plethora of optically-addressable defects within its large bandgap (≈ 6 eV) [58]. Having initially established themselves as bright and stable single-photon sources [338], defects in hBN have since then been proven to be useful for the integration into hybrid photonic devices [120], super-resolution imaging [127, 130, 281] and studying complex charge dynamics in aqueous environments [132, 219]. Moreover, several recent works have demonstrated spin-dependent emission from defects in hBN [122] at room temperature [104, 123, 124], opening novel avenues for this material platform [125].

Defects in hBN are either randomly formed during growth [88, 130], post-growth doping [339] or exfoliation from bulk crystals [97], or can be intentionally induced in the pristine material using large-area irradiation with ions [99, 127, 317], neutrons [136], or using high-temperature annealing [338]. While these approaches reliably produce quantum emitters in hBN, they result in a random spatial distribution of defects, thus complicating their proper and reliable characterization using correlated microscopy [128], and hindering their applications in integrated devices for nanophotonics [120] and nanofluidics (e.g. to systematically study the dynamics of charge transfer at liquid-solid interfaces [132, 219]). Recent attempts to generate defects in hBN at precise spatial locations included strain engineering through either exfoliating [101] or growing hBN material on patterned substrates [93], which offer scalability, but limited subsequent integration. Other patterning approaches included the use of pulsed lasers [102, 106], focused electron [105] and ion beams [103, 104] to locally damage the hBN lattice and generate emitters with desired properties.

Focused ion beam (FIB) seems an especially appealing technique for the generation of optically-active defects in vdW materials due to its versatility, high resolution, ease-of-use and potential scalability. Notably, FIB has found widespread use for patterning of 2D materials as a resist-free method [340, 341], mitigating omnipresent polymer contamination of the patterned material, and emergence of commercially-available plasma FIB (PFIB) machines, employing ions of inert gases, such as argon and xenon, instead of liquid metals, has solved the long-standing problem of sample contamination by gallium ions in the traditional FIB systems [342, 343]. Nevertheless, while deterministic defect generation in hBN using FIB has been recently demonstrated [103, 104], achieving sub-micron spatial accuracy, a proper understanding of the FIB irradiation effects and the formation of defect sites in hBN is lacking.

In this work we present a systematic study of these effects, arising from the beam interacting not only with the thin layer of hBN itself, but also with the substrate, on which it is placed. We also show, that the FIB-induced defects are strongly influenced by the environment in which the irradiated samples are used. In particular, we uncover a new mechanism of water-assisted etching of FIB-irradiated hBN defects, leading to a drastic structural and optical transitions in

irradiated sites. Moreover, by utilizing novel super-resolution microscopy technique correlated with AFM imaging, we are able to explicitly show the localization of emitters in hBN at the rim of FIB-induced defect sites, in good agreement with a hypothesis that exists in literature [103].

7.2 Results and discussion

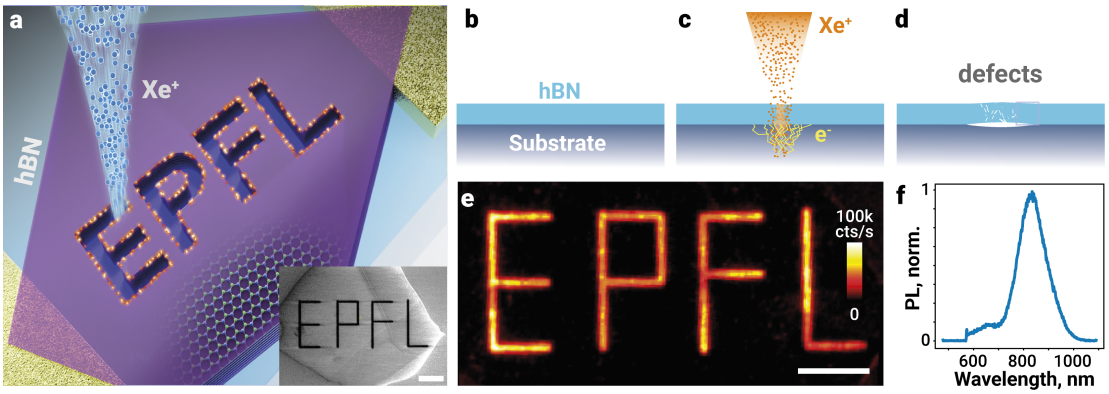

Figure 7.1 – Generation of FIB-induced optically active defects in exfoliated hBN flakes. a) Schematic representation of the defect writing process on an hBN flake using FIB. The inset shows a scanning electron microscope (SEM) image of a patterned flake inside the FIB chamber. b-d) Simplified schematic of the FIB-induced defect generation process: being a result of Xe ions interacting with the substrate (b) which is partially milled (c), creating a defected region and a void beneath the hBN flake (d). e) Fluorescence image of the generated pattern of optically-active defects. Imaging done in water. f) Characteristic spectrum of FIB-induced defects, taken from a dried sample in air. Scale bars: 10 μm (a, inset), 5 μm (e)

We employed the Helios G4 Xe PFIB system to investigate the influence of Xe ions irradiation on pristine hBN flakes, containing very few intrinsic defects [344]. The flakes were prepared on cleaned SiO_2 substrates with gold markers by mechanical exfoliation from high-quality hBN crystals [76], resulting in a typical thickness of hBN flakes ranging between 10-100 nm. Directly after exfoliation the samples were loaded into the PFIB machine and irradiated with a predefined pattern (Fig. 1a). The irradiated flakes were briefly checked in the built-in SEM, clearly demonstrating the FIB-induced changes in the morphology of the sample (Fig. 7.1a, inset). The simplified mechanistic understanding of these changes is shown in Fig. 7.1b-d, where defects are generated as a result of Xe ions interacting with the substrate. After unloading from the FIB machine the samples were inspected on a home-built fluorescence microscope confirming the creation of optically-active defects at the irradiated hBN sites (Fig. 7.1e). The spectral characteristics of FIB patterned defects perfectly agree with the previously reported ones for Xe FIB [104], with the broad emission peak centered around 830 nm (Fig. 7.1f). See Materials and methods for the details of the setup used.

To verify the structural changes induced on hBN flakes by the ion beam a detailed high-resolution transmission electron microscopy (TEM) study of the milled area cross-section

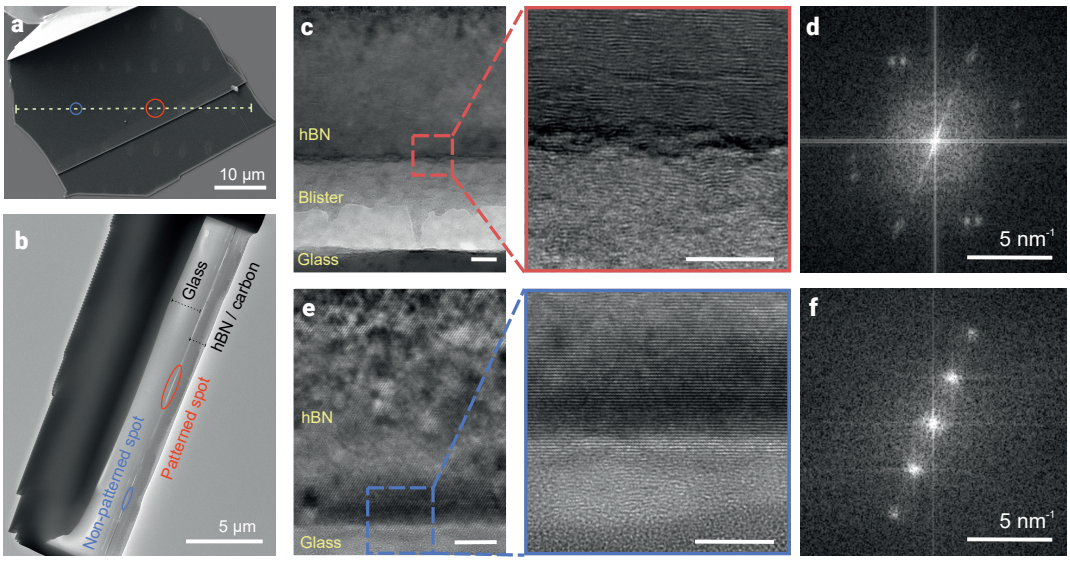

Figure 7.2 – Exploring mechanical effects of FIB irradiation using TEM. a) Irradiated hBN flake on a glass substrate, with $3\mu m$-spaced defect sites (seen as brighter spots on top of a darker hBN surface, marked with the line). b) a lamella of the hBN flake cross-section cut along the dashed line marked in a). A thin layer of carbon was sputtered on top of the flake to prevent charge accumulation. c) A cross-sectional image of the irradiated hBN area and d) corresponding fast Fourier Transform (FFT) compared to e) the pristine area image of the hBN/glass interface and its FFT f) shows a clear mechanical deterioration of hBN layers and the local amorphization of the material. Scale bars: 10 nm

was performed (Fig. 7.2). An hBN flake irradiated with typical experimental parameters (see Methods) was cut along the irradiated spots (Fig. 7.2a) with a Ga FIB system to create a thin lamella (Fig. 7.2b) suitable for TEM imaging. A high resolution image of the hBN/glass area on the irradiated spot (Fig. 7.2c) shows visible signs of mechanical damage and perforation caused by the PFIB on the hBN flake layers. Most of the damage is seen at the hBN/glass boundary due to the ion collision cascades, secondary electron emission and substrate particle sputtering occurring in the interaction volume area underneath the patterned spot (schematically marked in Fig. 7.1c). These effects lead to the hBN milling selectively occurring from beneath the flake, at the hBN/glass interface. Consecutively, this leads to the creation of the blister in between the hBN and glass substrate filled with the milled debris comprising of amorphized and recrystalized hBN as well as particles sputtered from within the substrate. The FFT of the irradiated flake area (Fig. 7.2d) shows signs of substantial amorphization and mechanical damage (smearing of the FFT pattern) of the hBN crystal lattice which can be associated with hBN blistering. The PFIB milling damage is especially visible when compared to unirradiated, pristine hBN/glass interface area (Fig. 7.2e) and its corresponding, clear FFT (Fig. 7.2f) image.

To explore the optical properties of FIB-induced defects, we have used both a home-built confocal setup and a widefield super-resolution microscope, optimized for the single-molecule localization microscopy (SMLM) [127]. We started with an hBN flake irradiated with line

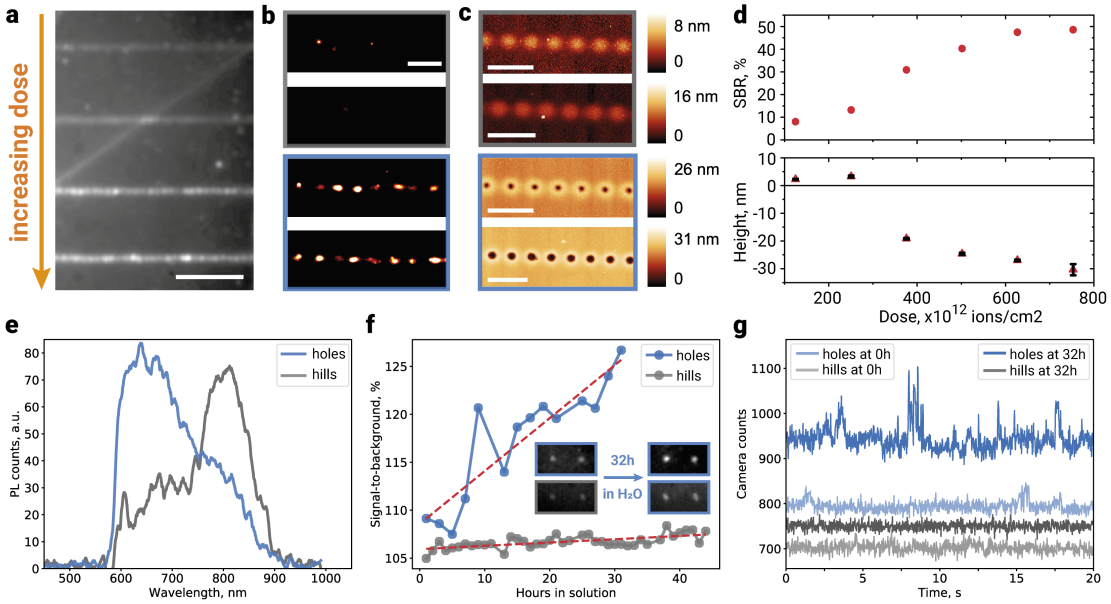

Figure 7.3 – Optical and structural characterization of irradiated defect sites. a) Averaged fluorescence image (under a 561 nm excitation) of an hBN flake with FIB-irradiated horizontal line patterns of a gradually increasing dose, which results in the creation of optically-active defects of increasing intensity. Imaging is performed in DI water, pH 5.8. b) Zoom-ins from (a), processed using localization microscopy algorithms, reveal two different types of emission: dim diffused emitters (type I) which are not picked up by the algorithm, and bright localized ones (type II) which are clearly visible. c) AFM scans of respective areas. Two types of emitters from optical images can be easily correlated with the difference in morphology, depending on the irradiation dose: hills are formed for lower doses and holes for higher ones. Imaging done in air, after thoroughly drying the immersed sample. d) Extracted signal intensities (signal-to-background ratio, SBR) and height/depth of the FIB induced defects vs. irradiation dose, showing the dose-dependent hill-to-hole transition. e) Spectra of two defect types in water. f) Change in brightness of two types of emitters after a long immersion in water. g) Comparison of the temporal dynamics of emitters before and after the long immersion. Scale bars: 5 μm (a), 1 μm (b,c)

patterns of varied irradiation dose ($1-8\times10^{14}$ ions/cm^2) to see how it affects the fluorescent emission from defects. From the averaged image stack, shown in Fig. 7.3a, one can see four horizontal lines of various intensity corresponding to the irradiated pattern of a gradually increasing dose. The zoom-ins into each of these lines in Fig. 7.3b are processed using an SMLM algorithm to precisely localize the isolated emission spots. However, one can see that in the top two images the localization algorithm fails to localize the emitters as their emission is rather dim and diffused (SBR of $\sim 5-10\%$). In contrast to that, the emitters in the bottom two lines are easily localized and are seen as regular bright spots with SBR of $\sim 30-50\%$ and ~ 500 nm pitch distance (Fig. S7.6).

To understand this difference in observed emission we performed AFM measurements on the same lines (Fig. 7.3c). One can immediately see that two types of emitters correspond to either

hill-type or hole-type defects created by the FIB depending on the irradiation dose. Therefore we will be calling these defects from now on hills and holes, respectively. The dose-dependent transition from one defect type to the other is shown in Fig. 7.3d and in the Supplementary Information (Fig.S7.6). The optical differences between two types of defects go much further than just their intensity. In Fig. 7.3e one can see an appearance of another spectral emission peak around 650 nm, measured from hole-type defects in water, while hill-type defects still show predominant emission around 800 nm. The 800 nm emission is also present in the spectrum of holes and is attributed to the remaining damaged material and/or strain around the hole. We further discuss the spatial distribution of these two emission lines in Fig. S7.14.

Another difference concerns the long-term evolution of the measured emission from holes vs. hills when the sample is immersed in an aqueous solution for a long time (tens of hours). In Fig. 7.3f one can see the steady increase in the signal intensity for holes and an absence of such increase for hills. This graph was obtained by analysing the timelapse images of the irradiated area, fitting the maximal intensity values at each defect site and normalizing it to its local background. An example of such images before and after the timelapse is shown in the inset and the full protocol can be found in Fig. S7.7. Finally, the temporal traces from both types of defects in the steady-state, shown in Fig. 7.3g, demonstrate sharp transitions between different intensity levels (blinking) for the emission originating from holes, but not from hills. This blinking behaviour is further intensified after a long stay in water which we link to the accumulation of dangling bonds and functional groups in the circumference of the hole-like defects and enhanced interaction with diffusing charges. The exact chemical composition of the defect sites is not yet know and remains the topic of future studies. Additional characterization of the optical properties of the created defects is shown in Fig. S7.9: bleaching, lifetime and saturation curves, as well as optically-detected magnetic resonance (ODMR) at 3.4 GHz perfectly matching the previously reported one [104].

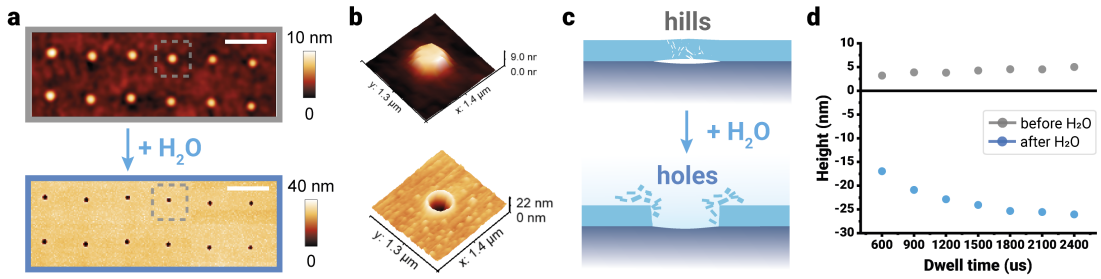

Figure 7.4 – Water-assisted etching of irradiated defect sites. a) AFM images of the same area on the irradiated flake before and after immersing it in water. Scale bar: 3 μm b) Pseudo-3D reconstruction of a single defect site before (top) and after water (bottom). c) Schematic representation of the water-assisted hill-to-hole transition. d) Dependence of the average peak height/depth of irradiated sites on irradiation dose.

Following the structural-optical transitions between two types of FIB-induced defects, immersed in the imaging medium (DI water), we explored in more detail its influence on the formation of defects. Having obtained an AFM scan of a marked area of an hBN flake just

after FIB irradiation, we observed the creation of only hill-type structures, even though the irradiation doses were high enough to create holes (in comparison to Fig. 7.3). However, after immersing the sample in water and imaging the same area with AFM again we have noticed the immediate creation of holes in the irradiated regions (Fig. 7.4a). The observed etching happened at a timescale faster than 2 consecutive AFM scans of the same area (20 minutes long each), suggesting a very fast dissolution process (Fig. S7.10). The 3D zoom-ins of the selected defect are shown in Fig. 7.4b and perfectly illustrate the water-mediated hill-to-hole transition. Fig. 7.4d shows a simplified schematic of the etching process, where the damaged hBN material at the irradiated sites (seen in Fig. 7.2) is quickly removed by water. However, once the holes are created their size doesn't seem to noticeably change both in air and in water over the course of days as seen in Fig. S7.11.

The dependence of the created height/depth of the hills/holes, respectively, on the irradiation dose is shown in Fig. 7.4d, suggesting a quasi-continuous hill-to-hole transition at a lower dose ($\sim 3 \times 10^{14}$ ions/cm^2 on Fig. 7.3d). The slight linear increase in the height of the hills at longer irradiation times probably comes from either more sputtering or a continuous cavity growth underneath hBN, which makes the thin flake bulk up. The saturation behaviour for the depth of the created hills can be explained by water fully etching through the hBN flake and reaching the substrate material. Combining these findings with data from Fig. 7.3, we conclude that the observed hill-to-hole transition is caused by water and is dose-dependent, i.e. starting from a certain FIB irradiation dose, which mechanically damages the hBN material enough for the water to dissolve it. This claim is supported by the TEM inspection of the irradiated areas in Fig. 7.2 and literature studying reactivity of mechanically damaged hBN in water [345]. This defect formation process is unique for hBN flakes deposited on substrates with thicknesses much larger than the typical beam penetration depth (< 100 nm) [104], due to the unique FIB-substrate interaction effects, illustrated in Fig. 7.2. No hole formation or subsequent structural or optical changes in water were observed for FIB-irradiated hBN flakes which were suspended over holes or supported on thin membranes. An example of such sample and its AFM analysis directly after irradiation is shown in Fig. S7.8, demonstrating the creation of hole-type defects pierced by the ion beam in the suspended hBN without any influence of water.

Finally, to better understand the origins of the emission, we performed correlative SMLM and AFM imaging of the hole-type defects. Briefly, we first acquired stacks of thousands of widefield images of irradiated hBN flakes with isolated defect sites immersed in DI water. The averaged image from one of these stacks is shown in the top-left part of Fig. 7.5a, while in the bottom-right part we show a reconstructed super-resolved image, processed by a novel deep-learning based localization algorithm DECODE [346]. Already in some of the bright defect sites in the averaged widefield image one can notice the presence of a darker central region, hinting on the probable emission from the edges of the formed hole as was suggested in literature [103]. However, by using DECODE (DEep COntext DEpendent) method for deep-learning based single-molecule localization [346] to detect and localize blinking emitters from FIB-induced defects, we arrive at the first direct evidence of such edge-related emission,

which is shown in detail in the zoom-in in Fig. 7.5b. Acquired AFM image of the same area matches well the SMLM data (Fig. 7.5c). To further verify and visualize the spatial distribution of emitters, we show the overlayed and rendered AFM-DECODE image in Fig. 7.5d, where one can clearly see the emergence of the fluorescent emission from the edge of the hole-type defects.

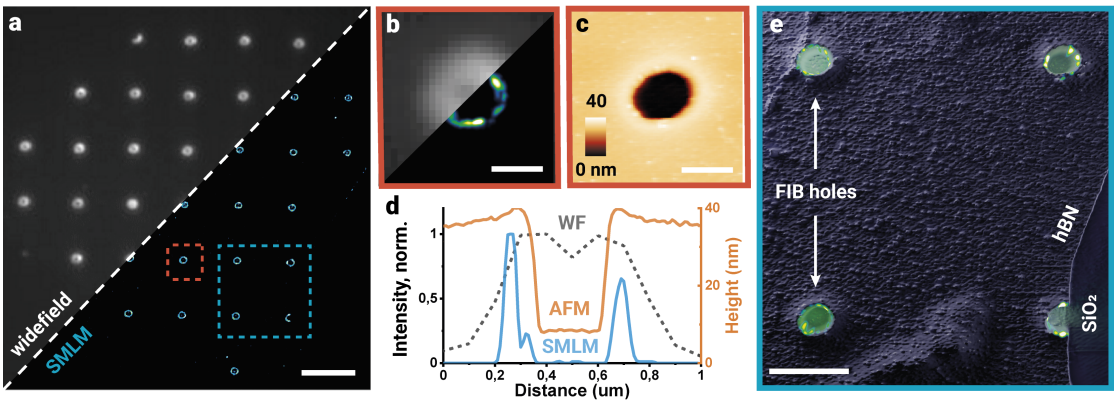

Figure 7.5 – Correlated super-resolution and atomic force microscopy of FIB-induced defects in hBN. a) Averaged fluorescence image of an irradiated hBN flake (2D array of isolated defects, 3 μm apart), overlayed by the super-resolved image of the same flake (processed using SMLM package DECODE). b) Zoom-in into the dashed red area around the isolated defect site (overlayed widefield/SMLM) c) AFM scan of the same area, perfectly matching the fluorescence data. d) Line profiles from zoom-ins in (b) and (c), showing cross-sections of the same defect site in widefield, SMLM and AFM images e) Correlated AFM-SMLM image of four defect sites from a dashed blue area in (a), clearly showing precise spatial localization of optically-active emitters at the rim of the holes, formed by FIB irradiation and activated by water. Scale bars: 3 μm (a), 400 nm (b,c), 1 μm (e)

While the hole-type defects, demonstrated in Fig. 7.5, are relatively large, smaller sub-100 nm defects were successfully created using the current technique and measured with AFM (see Fig. 7.4a and Fig. S7.12). However, having dense emitters on the rim of the defect sites hinders their analysis with SMLM-based super-resolution optical microscopy. Further optimization of irradiation parameters and imaging conditions will be aimed at enabling the use of the FIB-created emitters for multiple super-resolution microscopy modalities. Moreover, better spatial resolution and smaller waist of the ion beam, such as in the Helium Ion Microscopes (HIMs), can further decrease the affected defect sites by 1-2 orders of magnitude [347–349], paving the way for deterministic creation of atomically-small isolated defects with nanometer precision emitting single photons. Further miniaturization of optically-active defects to below 100 nm scale should also enable new studies of nanofluidic phenomena at the liquid-solid interfaces [132, 219] with unprecedented spatial control over the nanoscale charge dynamics.

7.3 Conclusion

We presented a systematic study of the focused ion beam interactions with supported thin exfoliated hexagonal boron nitride flakes, leading to the creation of optically-active spin defects. We showed that the defect creation is the result of the ion beam interacting not only with the thin hBN flakes, but also with the substrate, on which it is supported. Moreover, both the structural and optical properties of the induced defects are dose-dependent and undergo irreversible transitions in aqueous solutions, representing a new mechanism of water-assisted formation of FIB-irradiated hBN defects. By utilizing super-resolution microscopy correlated with AFM imaging, we are able to explicitly show the localization of emitters at the rim of the created defect site. Our findings lay the foundation for FIB-assisted engineering of optically-active defects in hBN with nanoscale control for nanophotonics, quantum sensing and nanofluidics.

7.4 Methods

7.4.1 Sample preparation

hBN flakes from high quality crystals [76] were exfoliated onto glass coverslips (no. 1.5 Micro Coverglass, Electron Microscopy Sciences, 25 mm in diameter), pre-patterned with gold markers for easier navigation and electrode mesh to prevent accumulation of charges. Exfoliation was done either using tape or gel-pack stamps. The flakes for TEM grids (Norcada, NT025C) were polymer-transferred. Si/SiO_2 substrates have also been used, with similar patterning results.

7.4.2 FIB irradiation

Irradiation and hBN patterning was done on Helios G4 PFIB UXe system with Xenon Plasma FIB column. All experiments were done at 30kV and 100pA Xe beam with varying parameters of dwell time and pitch distance between irradiated spots. By varying the dwell time from 100μs to up to 2ms we effectively increase the irradiation dose and pattern outcome in the form of irradiated spot size. Pitch distance is typically set to 3 μm for studying isolated defects and between 300 and 500 nm in case of tighter arrays and line patterns. Typical ion fluence/dose ranges from 1.2×10^{14} to 2.5×10^{15} ions/cm^2 for dwell time range of 100 μs to 2 ms.

7.4.3 Optical inspection

Widefield imaging has been done on a custom widefield fluorescence microscope, described elsewhere [127, 130]. Briefly, the emitters are excited using either 488 or 561 nm laser (Monolitic Laser Combiner 400B, Agilent Technologies), which is collimated and focused on the back focal plane of a high-numerical aperture oil-immersion microscope objective (Olympus TIRFM

100X, NA: 1.45). This creates a wide-field illumination of the sample in an area of $\approx 25\mu m^2$. Fluorescence emission from the sample is collected by the same objective and spectrally separated from the excitation light using dichroic and emission filters (ZT488/561rpc-UF1 and ZET488/561m, Chroma) before being projected on an EMCCD camera (Andor iXon Life 897) with EM gain of 150. An additional spectral path, mounted in parallel to the localization path allows for simultaneous measurements of the emission spectra from individual emitters [127]. The sample itself is mounted in a sealed fluidic chamber, which is placed on a piezoelectric scanner (Nano-Drive, MadCityLabs) for fine focus and drift compensation using an IR-based feedback loop which is especially important for long-term measurements. Typical exposure time is 20-50 ms and typical laser power 50-100 mW. A typical acquired image stack contained 2-10 thousand frames.

Confocal imaging was done on two different setups, utilizing either 532 nm or 561 nm excitation lasers and APDs as well as spectrometers to detect the emitted light. The first setup was used to obtain both emission and absorption spectra of defects to make their 2D spectral maps. However, due to the limitations in construction this setup could only be used to image samples in air. In order to perform emission measurements a diode pumped solid state (DPSS) laser (DJ532-40, ThorLabs) at 532 nm was used. The laser beam was passed through a single mode fiber (P3-460B-FC-1, ThorLabs) to obtain a gaussian beam profile. Afterwards, a narrow bandpass filter (FL05532-1, ThorLabs) was is placed in the beam path to remove any unwanted features from the laser spectrum. A 100X, 0.9 NA objective (MPLFLN, Olympus) focused the beam on the sample and collected the emission. The sample was mounted vertically on a piezoelectric stage (Nano-Drive, MadCityLabs) and a raster scan was performed to obtain the spectral maps. The laser line was removed from the emission spectra by a longpass filter (FELH0550, ThorLabs) and the signal was recorded using a spectrograph (Kymera 193i, Andor) with a CCD (iDus, Andor). For absorption measurement, the sample was illuminated from the back by a calibrated halogen lamp (SLS201L, ThorLabs). The transmitted light was collected, on the opposite side of the sample, by 100X, 0.9 NA objective (MPLFLN, Olympus) and the spectrum was recorded with the CCD. In order to extract the absorption, a measurement was first made on the substrate and used a background signal.

To compensate for this we utilized a second confocal setup in an inverted microscope configuration allowing us to image samples in liquid. Here the emission was split between two fiber-coupled APDs (SPCM-AQRH, Excelitas) in an HBT configuration. One of the APDs could be switched with a fiber-coupled spectrometer (QE Pro, Ocean Optics) to measure the emission spectra in liquid. The setup could also perform lifetime and photon correlation measurements using the PicoHarp TCSPC module (PicoQuant).

7.4.4 TEM Imaging

The lamella for cross-section imaging was cut using the Zeiss NVision 40 CrossBeam system. Irradiated flake chosen for cross-section imaging was patterned using default array parameters

i.e. 30kV, 100pA Xe FIB. High resolution TEM imaging was performed at Talos L120C G2 using 80kV electron beam.

7.4.5 AFM imaging and image processing

For the AFM imaging a customized AFM, consisting of a Dimension Icon AFM head (Bruker) mounted above an optical microscope (Olympus IX83), was used. The position of the hBN flakes with respect to the cantilever was detected with the optical microscope. AFM images in air were recorded at a line rate of $0.5 Hz$ with RTESPA-150 cantilevers (Bruker) with a nominal spring constant of $6 Nm^{-1}$ in tapping mode. The cantilever drive frequency and amplitude were determined by automated cantilever tuning. AFM images in fluid were acquired at $0.5 Hz$ line rate using ScanAsyst Fluid cantilevers (Bruker) with a nominal spring constant of $0.7 Nm^{-1}$ in PeakForce quantitative nanomechanical mode (QNM) at an oscillation rate of $1 kHz$ and a force setpoint of $3 nN$. The images were processed with a standard scanning probe software (Gwyddion).

7.4.6 SMLM processing

Acquired image stacks from the widefield microscope were processed using several SMLM algorithms: ThunderSTORM [350], SOFI [] and DECODE [346], a new deep learning-based localization algorithm. DECODE processing is beneficial in this case as the emitter density around the rim is high (Fig. S7.15) and standard SMLM algorithms, such as Thunderstorm [350], are failing to properly localize individual emitters, resulting in localization artifacts (Figs. S7.15,7.16). To utilize DECODE, We trained the neural network provided by the authors using simulated frames with a high density of emitters ($5\ \mu m^{-2}$), a realistic intensity distribution (1000 ± 800 photons/event), and the experimental point spread function calibrated with fluorescent beads.

Another approach to analyse such type of data with dense emitters is to use the super-resolution optical fluctuation imaging (SOFI), which better tolerates the high density of emitters and similarly to DECODE shows the clear existence of the fluorescent rim at the edge of hole-type defects (Fig. S7.16). SOFI images were processed using a previously published algorithm [351]. Both SOFI and DECODE approaches have allowed to clearly resolve rims of the defect sites, but DECODE led to fewer image artifacts than SOFI.

7.4.7 Acknowledgements

The authors would like to acknowledge support from the EPFL Interdisciplinary Center for Electron Microscopy (CIME) and especially Lucy Navratilova for the help with lamella preparation. E.G. V.N.and A.R. acknowledge the Max-Planck EPFL Center for Molecular Nanoscience and Technology as well as the NCCR Bio-inspired materials. M.M. acknowledges financial support from Swiss National Science Foundation (SNSF) Grant Number $200021_1 92037$. K.W.

and T.T. acknowledge support from the Elemental Strategy Initiative conducted by MEXT, Japan, and CREST (JPMJCR15F3), JST.

7.5 Supplementary Information

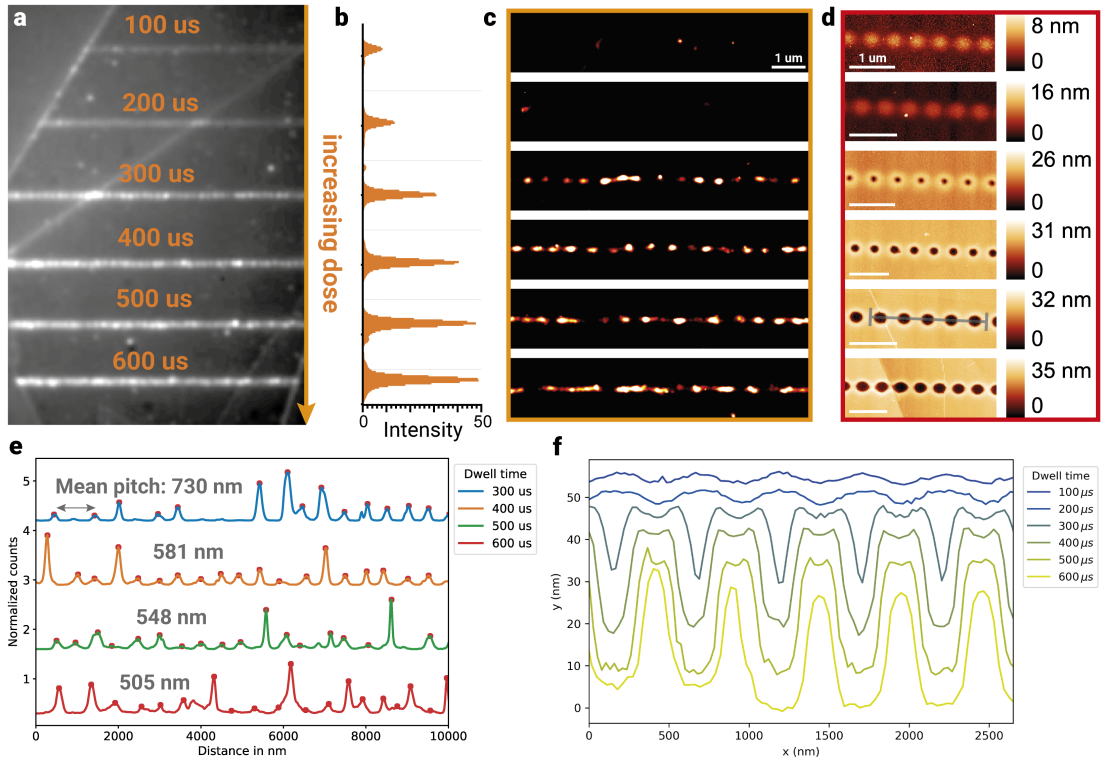

Figure 7.6 – Analysis of FIB-induced line patterns of structural and optically active defects. a) Fluorescence image of an exfoliated hBN flake, with lines of defect sites, induced by the FIB. Irradiation dose increases from the top to the bottom line. In-line pitch: 500 nm. b) Average intensity of each line of defects. c) SMLM images of the defect lines. d) AFM images of the defect lines. Two distinct groups of defects are produced, depending on the irradiation dose: hills for lower doses and holes for higher ones. e) Line profiles of the emitters in (c) with calculated average pitch distance. f) Line profiles of the AFM images in (d). Scale bars: 5mm (a), 1mm (c,d)

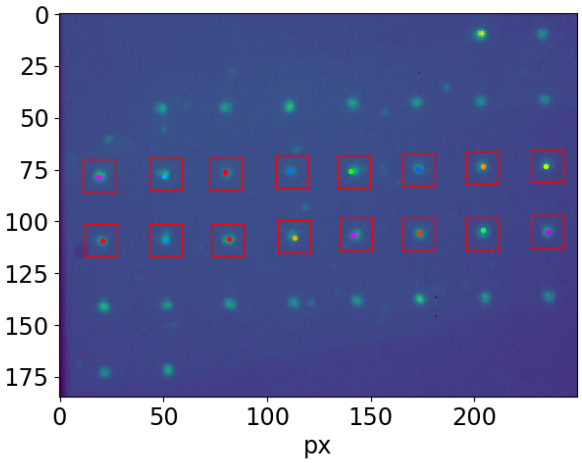

Figure 7.7 – Calculating Signal-To-Background Ratio values from processed widefield images (averaged stacks). Each emitter's position was manually selected, then the maximum intensity pixels were automatically found and averaged to get the signal value. To obtain the local background value the intensities of border pixels (indicated by red squares) were averaged. The final SBR value was calculated as the signal value divided by the background value. Pixel size: 100 nm

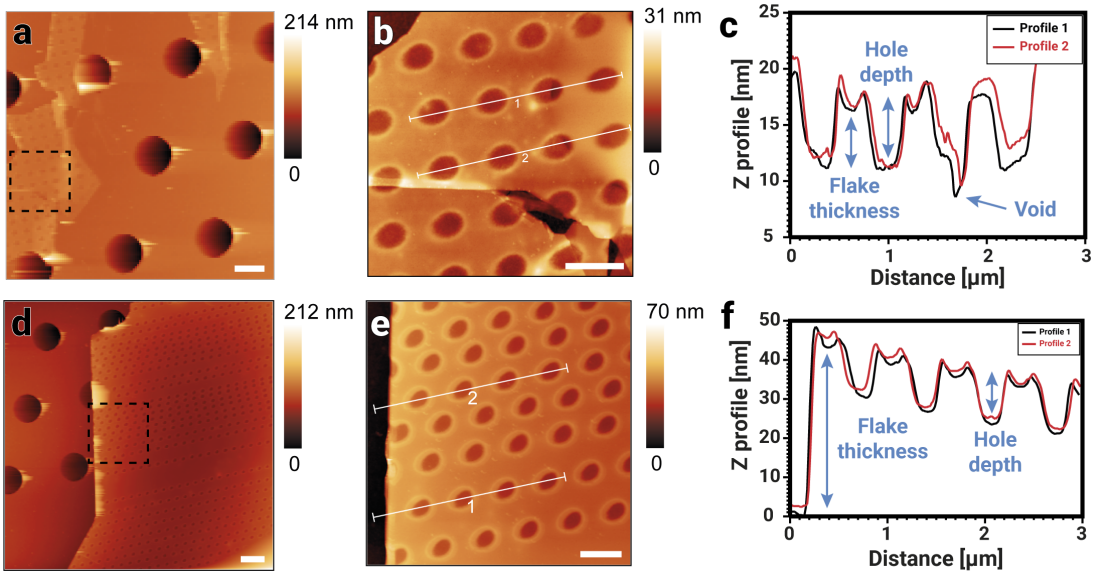

Figure 7.8 – AFM analysis of suspended FIB-irradiated hBN flakes. a) Silicon nitride TEM grid with a thin hBN flake, irradiated with a 2D array of defects (pitch distance 600 nm, beam current 100 pA, dwell time 1.4 ms). b) Zoom-in into highlighted region in (a). c) Height profiles along respective lines in (b), showing that the flake is fully pierced by the ion beam. d) A thicker hBN flake on the same TEM grid, patterned with the same FIB parameters. e) Zoom-in into highlighted region in (d). f) Height profiles along respective lines in (e), showing that the flake is only partially milled by the ion beam. Scale bars: 1 μm (a,d), 500 nm (b,e)

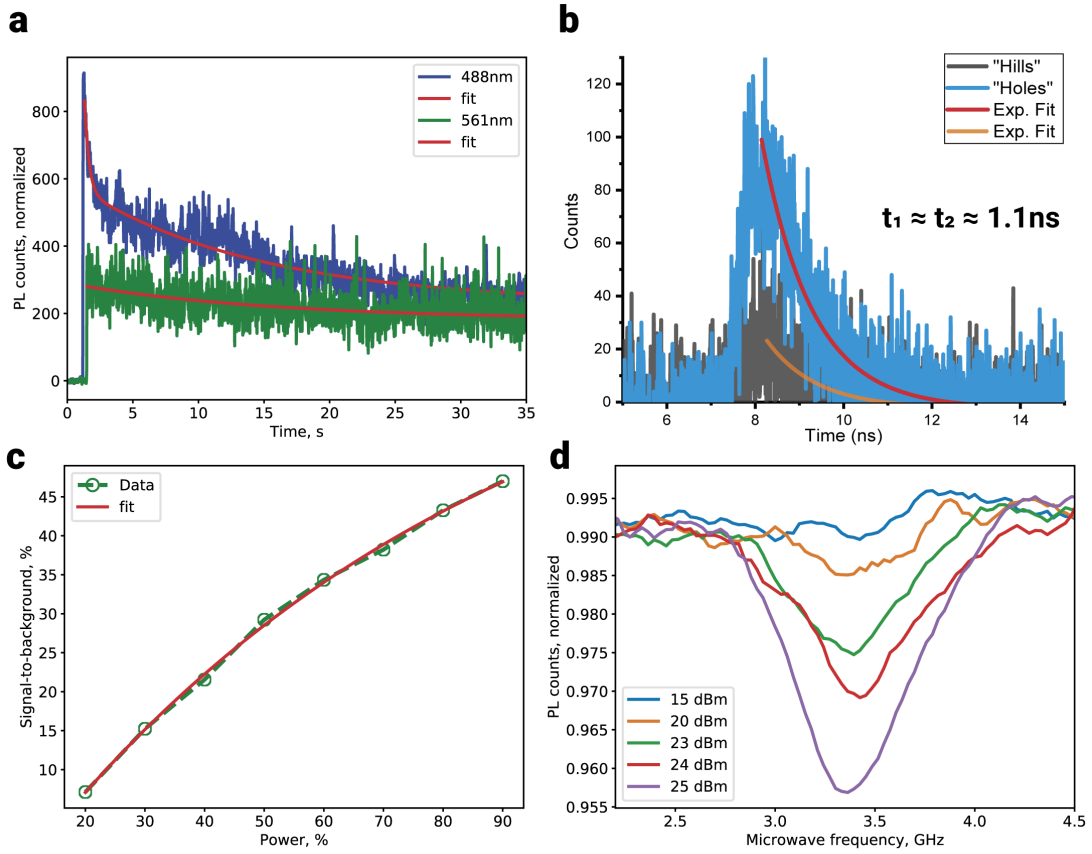

Figure 7.9 – Additional characterization of optical properties of FIB-induced defects. a) Bleaching curves under 488 nm and 561 nm CW illumination. Double-exponent fit for the 488 illumination hints on two types of emitters being bleached. b) Fluorescence lifetime of hole- and hill-type defects under pulsed 561 nm illumination (background-corrected). While amplitude of fluorescence differs significantly, the lifetimes are quite similar, ≈ 1.1 ns. c) Saturation curve for the hole-type defects (P_{sat} ≈ 50% of laser power, corresponding to ≈ 50 mW) d) ODMR curves for varying microwave power, for hole-type defects. Measurement done on a dried sample in air.

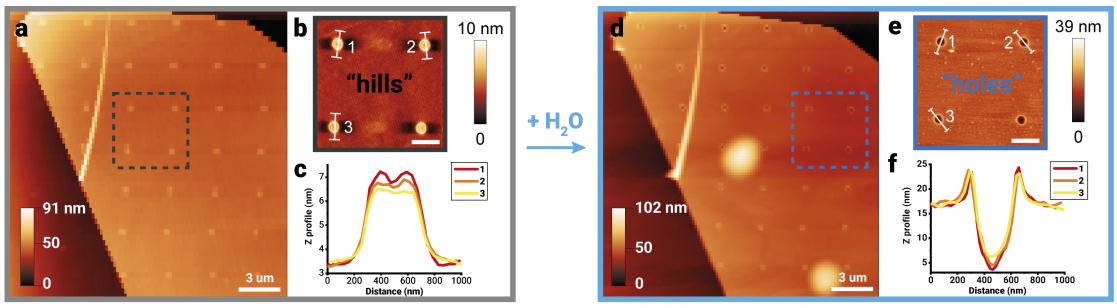

Figure 7.10 – AFM analysis of FIB-irradiated hBN flakes before (a-c) and directly after (d-f) immersing the sample in water. The hole formation therefore happens on a timescale faster than a single high-resolution AFM scan (≈ 20 minutes). Scale bars: 1 μm (a,d), 500 nm (b,e)

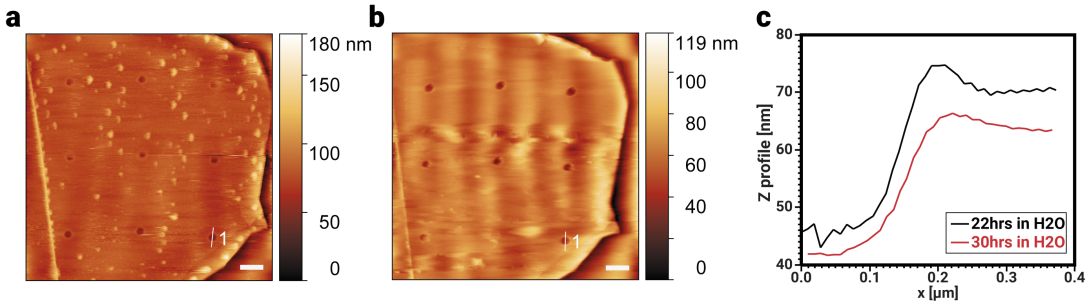

Figure 7.11 – AFM timelapse of the same irradiated hBN flake immersed in water. a) After 22 hours. b) After 30 hours. c) Height profiles along respective lines in (a, b), showing that the holes are not changing their diameter (≈ 400 nm) much over time. Scale bars: 1 μm (a,d), 500 nm (b,e)

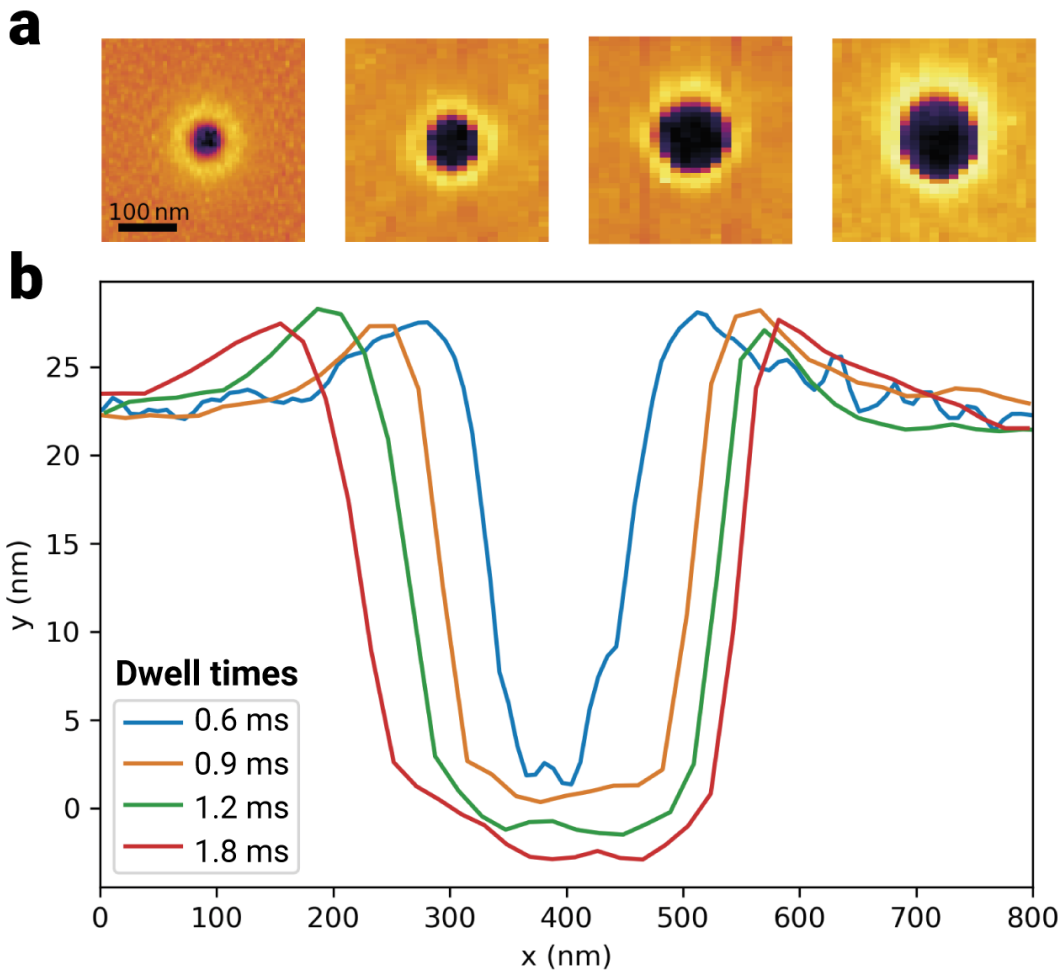

Figure 7.12 – Dependence of hole size on irradiation dose (dwell time). a) AFM images of isolated holes after water. b) Height profiles of their cross-sections. Scale bar: 100 nm

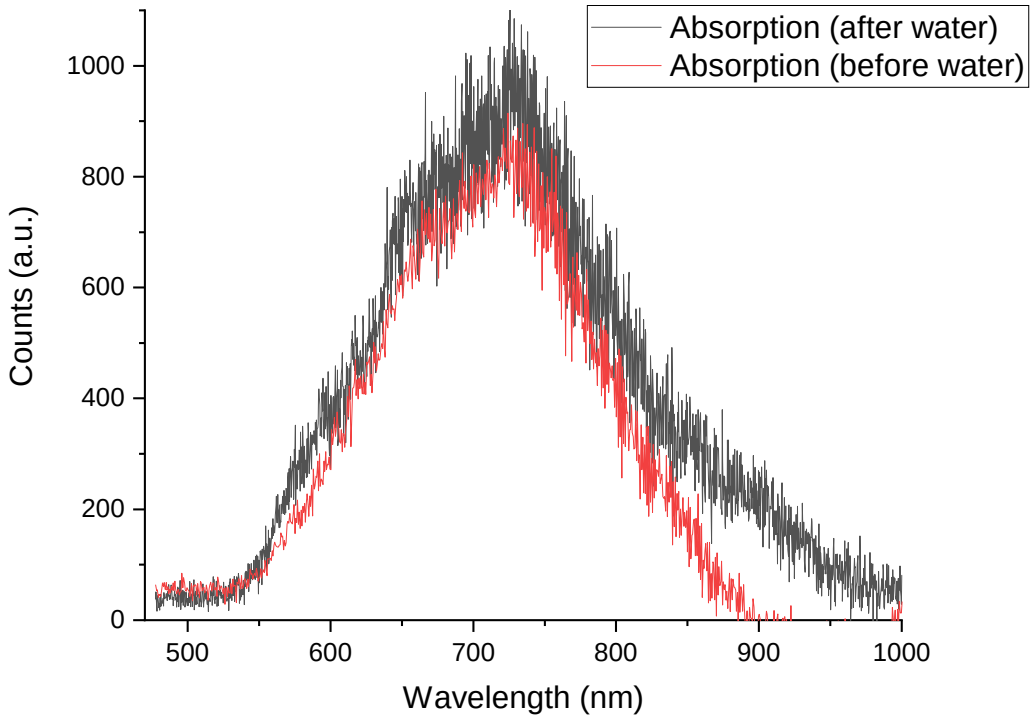

Figure 7.13 – Absorption spectra of defects before and after water treatment. The measurement was done in transmission using a white light source. The background measured next to the irradiated flake was subtracted from the recorded signal.

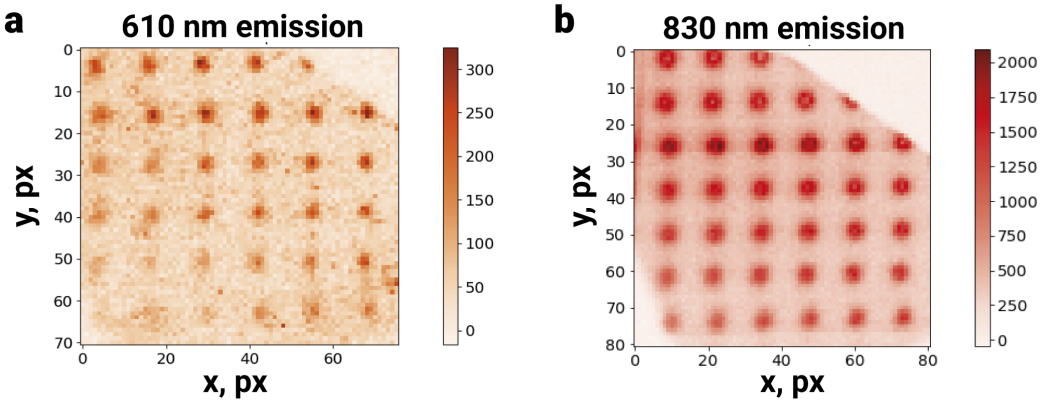

Figure 7.14 – Confocal spectral mapping of produced defects with varying irradiation dose. Emission pattern at a) 610 nm and b) 830 nm, corresponding to two spectral peaks observed in Fig. 3 in the main text. The emission at 830 nm seems to come from a larger ring around the defect site, while the 610 emission is more localized towards the center. Pixel size: 250 nm

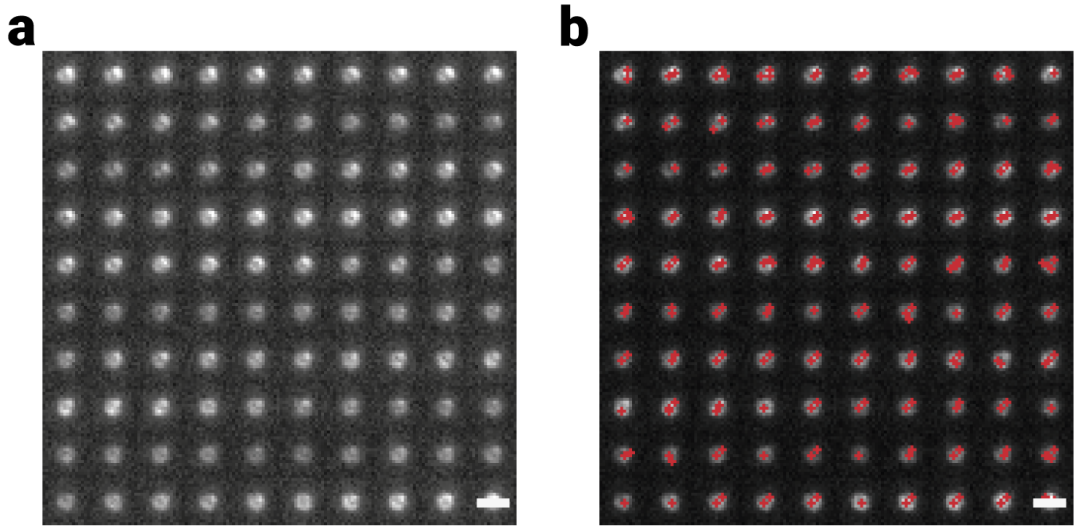

Figure 7.15 – a) Montage of a single FIB-induced defect site, emitting over 100 frames (2 seconds). Fluctuations in fluorescence intensity and spatial distributions are well visible, but the density of emitters is high, which prevents the localization of single emitters b) Same montage with an overlay of the SMLM detections, performed by ThunderSTORM [350] algorithm. One can notice multiple false localizations due to high emitter density, leading to artifacts in the reconstructed image below. Scale bar: 1 μm

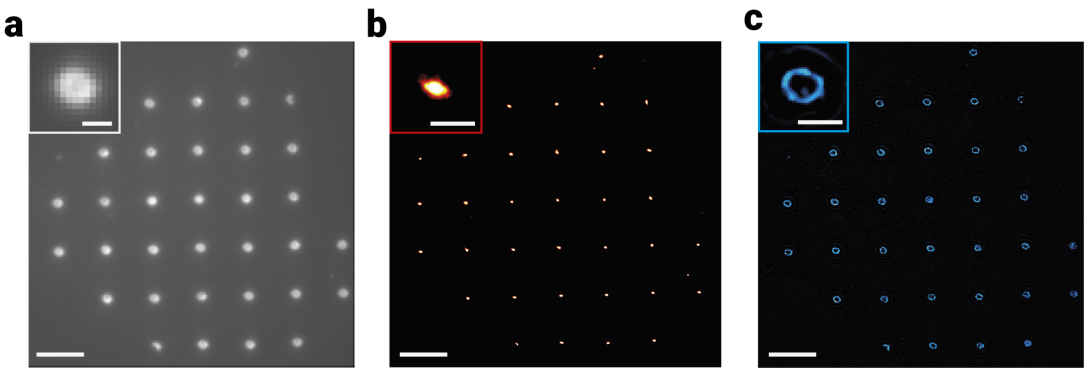

Figure 7.16 – Processed widefield images of fluorescent defects. a) Averaged image of the stack of 10'000 frames with 20 ms exposure. b) Reconstructed image, summing up localizations of the same image stack, processed by the ThunderSTORM plugin. c) Result of super-resolution optical fluctuation imaging (SOFI) processing, clearly displaying the grouping of emitters around the defect rim. Scale bar: 3 μm (a-c), 500 nm (insets)

8 Conclusion and outlook

In this chapter I will summarize the research results obtained during my PhD studies and will provide a personal outlook on the future developments in the field of optically active hBN defects. Everything written in this chapter reflects my personal attitude and views.

Starting my PhD journey with fluorescent nanodiamonds containing NV centers, I used them as an established and well-studied platform to study novel (an, in a way, more exotic) defects in vdW materials with a special emphasis on highly promising emitters in hBN. As the work was already underway when I joined the lab, I could quickly learn from the more experienced lab members and continue their efforts in this research direction. In parallel, I was also building a custom combined confocal/widefield microscope, described in Appendix A.1, which allows to perform both widefield fluorescence microscopy and a scanning one, capable of spectral, lifetime and photon statistics measurements. All these measurement modalities, calibrated on nanodiamonds, were extremely useful to study the optical properties of emitters in hBN.

My first contribution, however, started from performing experiments with Dr. Jean Comtet, who has built a custom spectral localization microscope, allowing both to record the spatial, temporal and spectral distribution of optically active defects in hBN on an ensemble scale. While first we started imaging intrinsic defects in CVD-grown monolayer hBN, which had to be transferred from a metallic growth substrate to the dielectric one to not quench the fluorescence from defects, we later transitioned to inducing optically active defects in pristine exfoliated hBN flakes using O_2 plasma. We observed at least two distinct spectral groups of emitters on both types of samples (with emission lines at 585 and 650 nm, respectively) and characterized their photophysical properties, described in detail in Chapter 4.

As the spectral SMLM setup uses half of the camera sensor to detect the spatial information, and the other half - for the spectral one, the already limited (by the high NA objective) field-of-view is shrunk even further, rendering suitable imaging area to about 20x20 μm^2. Knowing, that a similar problem exists for TIRF microscopy, where it is further deteriorated by the non-uniformity of illumination, together with Dr. Anna Archetti we started developing a specialized waveguide-based imaging platform meant to circumvent these shortfalls (which are not only

limiting the microscopy throughput, but can also introduce imaging artefacts). As a result of our endeavours, we managed to increase the field-of-view by at least 25 times, still having a uniform illumination of the sample. Tackling together all aspects of simulating, designing and measuring such on-chip platform took quite some effort, but resulted in 3 publications over 3 years, spanning from DNA-PAINT applications, to high-throughput imaging of transferred and as-grown two-dimensional materials, described in Chapter 5.

While imaging 2D materials on waveguides for hours in dark room, my eyes started seeing tracks of fluorescent emitters on the surface of hBN flakes, which I first attributed to eye fatigue. However, the reconstructed SMLM images we also from time to time showing a similar picture, indicating that the emitters were switching ON and OFF in a coordinated fashion. Discussing these findings with Dr. Jean Comtet led to an extremely fruitful project, where the appearance of such fluorescence tracks was attributed to charged particles, diffusing along the defects sites and sequentially activating their fluorescence by adsorbing on their surface and changing their charge state. Performing multiple tracking experiments with varying pH and temperature of the aqueous solution covering hBN surface, and carefully analysing the data, we were able to pinpoint single excess protons as the diffusing charged particles responsible for the correlated defect activation. This work, described in detail in Chapter 6, is opening a whole new field of investigating complex charge dynamics at the liquid-solid interfaces using optically active defects. More experiments in mixtures of various solvents have followed, some of which are described in Ref. [219].

Finally, to be able to reliably and systematically explore nanoscale phenomena in liquids using hBN emitters, we needed to be able to have a good degree of control over the locations of individual defect sites. After several attempts on using e-beam irradiation or patterned substrates for this purpose, together with another PhD student, Michal Macha, we employed Xe pFIB to deterministically create the optically active defects in thin exfoliated hBN flakes. Optimizing the irradiation parameters took quite a while, but allowed us to achieve sub-100 nm defect sizes with the positioning accuracy of tens of nanometers. Moreover, during this project we discovered a remarkable structural-optical transition between different defect types, induced by the FIB, depending on the irradiation dose and assisted by aqueous solutions in which the irradiated flake was immersed. Utilizing correlated SMLM-AFM imaging coupled with state-of-the-art processing algorithms, we managed to directly visualise the spatial distribution of fluorescence within a single diffraction-limited defect site. The first steps on this exciting journey are described in Chapter 7.

Looking into the future I can easily see how all the techniques mentioned above are converging to explore in detail the complex charge dynamics at the liquid-solid interfaces using engineered optically-active defects. Spin-dependent emission from such defects can serve as a nanoscale sensor to monitor the fast processes happening at a single-charge scale. Seeing experiments with NV centers in bulk diamond [352, 353] and nanodiamonds [19], I am quite certain that they will be implemented with hBN emitters as well. Moreover, not only detection of nanoscale charges might be possible, but also their manipulation due to preferential

pathways along the liquid-solid interfaces and induced hydrogen-bonding networks. This will require a 1-2 orders of magnitude better control over the size and position of the defects and should be implementable using state-of-the-art helium microscopes.

Another promising avenue opens up with the development of novel single-photon avalanche detector (SPAD) arrays [354], bringing their ultimate sensitivity and picosecond temporal resolution to the traditional widefield microscopes, currently limited by the low signal-to-noise and millisecond time resolution. Application and further development of such detectors to study dynamics of hBN emitters might reveal many exciting details currently inaccessible due to equipment constraints. Using SPAD detectors might also enable the high-throughput quantum sensing applications on arrays of emitters, combined with biological samples [355], micro- or nanofluidic channels.

To harness the full potential of emitters in hBN, it would be advantageous to achieve their electrical excitation [11] and readout, similar to the photoelectrical detection of magnetic resonance (PDMR) demonstrated for NV centers in diamond [13]. This could be highly advantageous for co-integration of hBN emitters into photonic integrated circuits (PICs) and their use in real-life devices. One example of such device can be the quantum random number generator (QRNG), based on the single-photon emission from optically active defects in hBN. While currently demonstrated at the laboratory scale, its integration into a miniaturized device will be crucial for its real-life applications [356]. Another rapidly developing application for spin defects in hBN will be their use as nanoscale sensors for temperature, pressure, strain, etc. [357, 358]

Finishing this outlook, I would also like to reflect on the future of on-chip imaging platforms. After the initial development of imaging waveguides on traditional substrates, like silicon, which are non-transparent for visible light [184, 261], the next step would be to fabricate such waveguides on transparent substrates (e.g. fused silica [359]). This will allow such chips to be used not only on upright microscopes, but also on inverted ones, which are commonly used in biology. Moreover, it will enable the use of higher-NA oil-immersion microscope objectives, enhancing the achievable resolution. Having the imaging objective at the bottom of the chip will also allow for additional co-integration with microfluidics on top [184]. Further benefits can also come from the electrical tuning of the penetration depth of the evanescent field, which can be achieved using transparent conductive films, such as polymers or indium tin oxide (ITO). However, the ultimate challenge for the on-chip imaging platform is their ease-of-use and accessibility for the larger imaging community, and further developments are needed to make this imaging modality widely used.

A Experimental hardware & methods

A.1 Optical setup

Even though during my PhD I worked on multiple optical setups, mentioned throughout this thesis, one is particularly close to my heart as I was disassembling and assembling it again so many times during 5 years! Sometimes I felt like I was still the same 5-year-old kid still playing LEGO, just the kits became a bit more complex and expensive (but not less fun!). This ever-changing multi-purpose home-built confocal/widefield microscope, known as "Evgenii's setup", is shown in Fig. A.1 and Fig. A.2 below.

This setup allows to both excite fluorescence using three excitation lasers (561 nm CW (Spectra-Physics, Excelsior), 561 nm CW and pulsed (PicoQuant LDH-561), 470 nm CW and pulsed (PicoQuant LDH-D-C-470)), see the geometry and navigate around (using motorized micro- and piezo nano-stages) with white light illumination, and perform the detection using sCMOS camera (Andor Neo) or fiber-coupled APDs (Excelitas, SPCM-AQRH-14), one of which can be easily swapped with a fiber-coupled portable spectrometer (Thorlabs OSA) to check the spectrum of the emission. Two APDs in the Hanburry-Brown-Twiss (HBT) configuration not only allow to perform lifetime measurements thanks to the fast counting electronics (dual-channel PicoHarp 300, PicoQuant), but also to collect photon statistics for bunching/antibunching measurements. And the addition of the microwave source (Keysight N5180) connected to a microwave antenna allows one to perform ODMR measurements. The setup also has an infrared laser (1064 nm, Coherent Mephisto) for optical trapping applications.

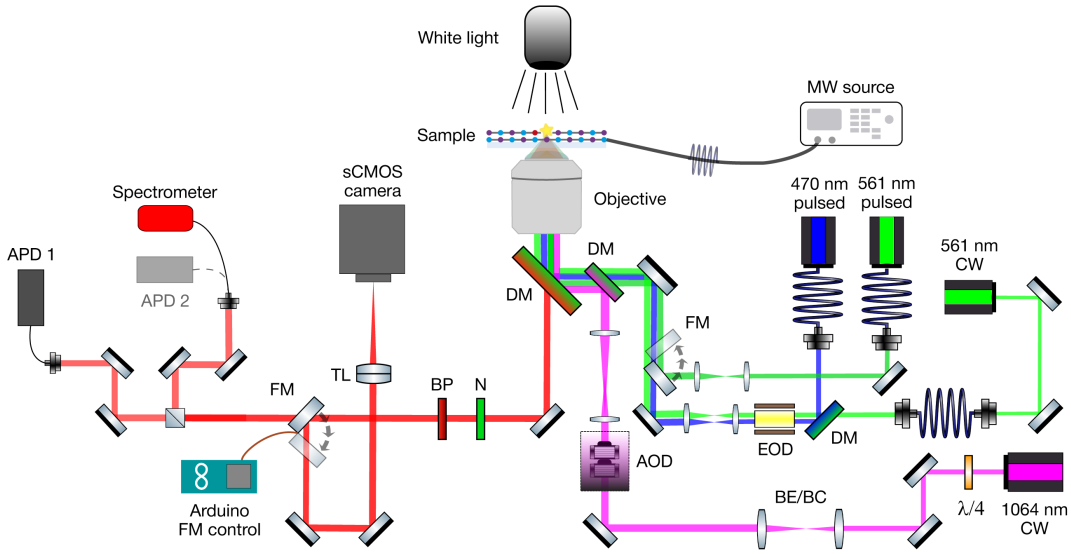

Figure A.1 – Schematic of the multi-purpose home-built confocal/widefield microscope. DM - dichroic mirror, FM - flip mirror, BE/BC - beam expander/beam collimator, EOD - electro-optical deflectors, AOD - acousto-optical deflectors, N - notch filter, BP - banpass filter, TL - tube lens.

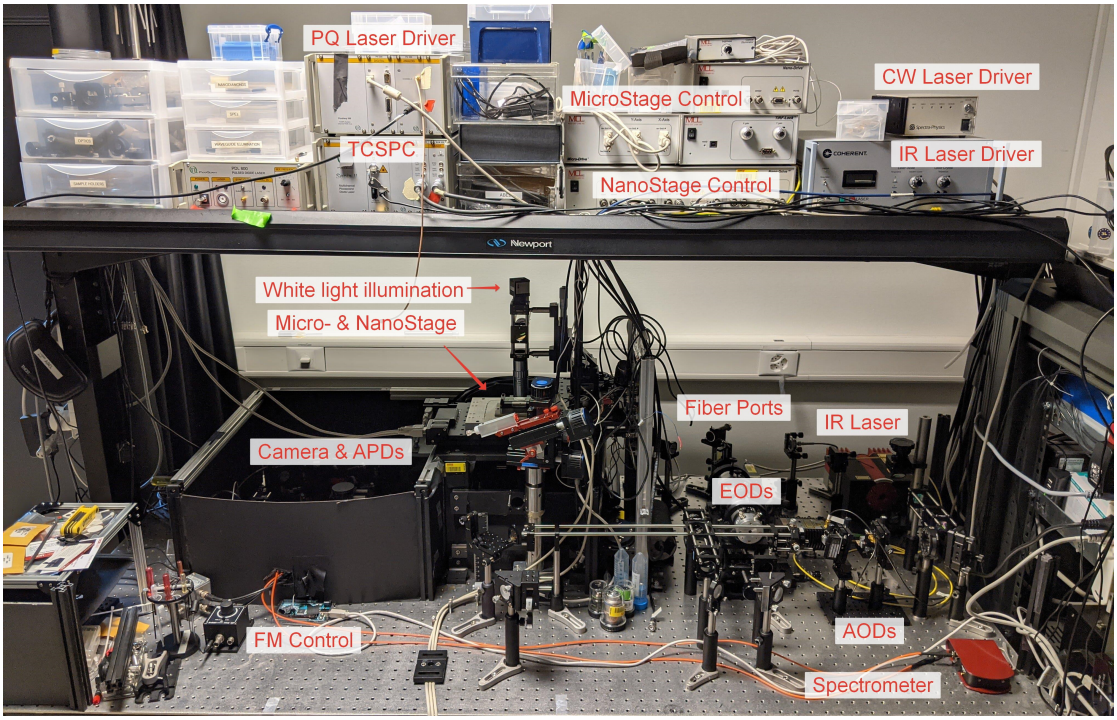

Figure A.2 – Photograph of the home-built confocal/widefield microscopy setup with labels.

A.2 Sample holder for microwave measurements

Coming from the superconducting circuits community, I was used to work with microwave structures. Therefore I designed, developed and fabricated a modular PCB-based sample holder for microwave measurements (aiming at doing ODMR of NV centers and defects in hBN). The sample holder, two versions of which are shown in Fig. A.3a, consisted of a printed circuit board (PCB) and a glass coverslip (25 mm in diameter, 170 μm thick), which was glued and wire-bonded to the PCB. Both PCB and coverslips were patterned to have a coplanar waveguide (CPW) to conduct microwaves in the 1-5 GHz range, generated by a MW source and supplied to the PCB via an SMA cable plugged into an SMA connector (Fig. A.3b). The fluorescent samples under study were placed in the middle of the coverslip (Fig. A.3c), ideally in between the ground and the central wire leaving the optical window of 40 μm wide and several mm long (Fig. A.3d). Such holder allowed for the efficient delivery of microwave power to the inspected samples. Calculations of the CPW dimensions were done in TXLine and the layout was made in the free K-Layout editor, fabrication was done in ACI and CMI at EPFL.

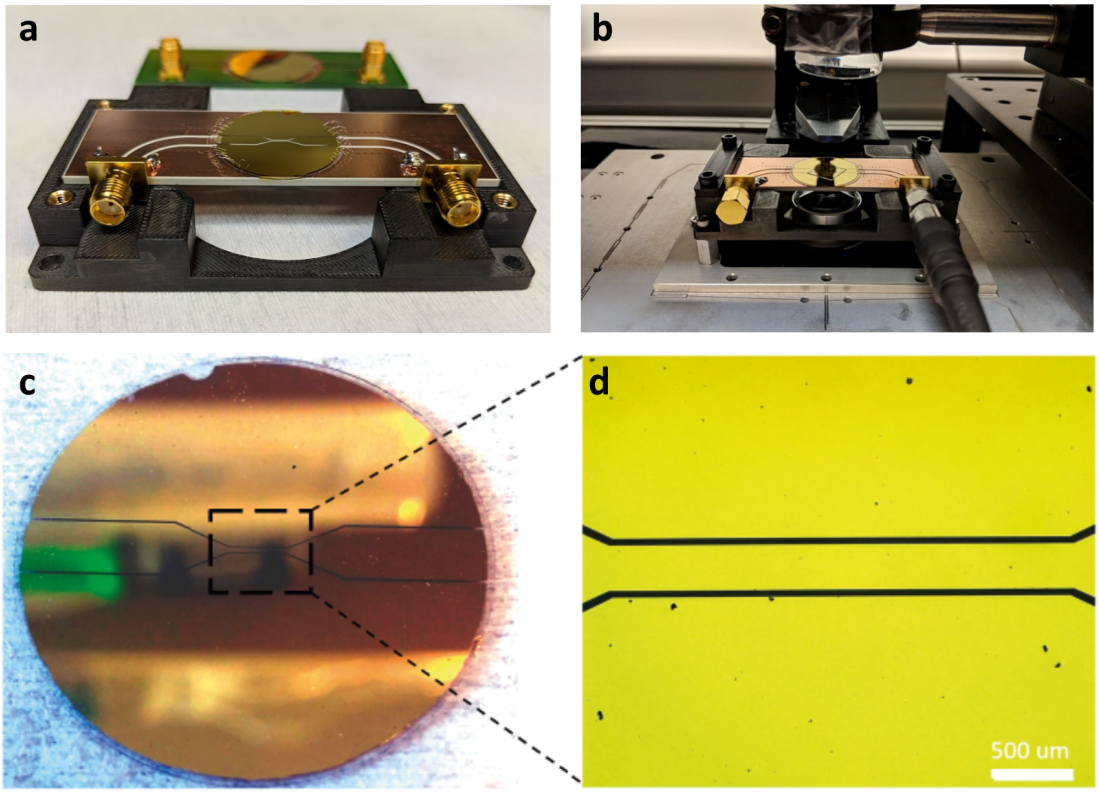

Figure A.3 – a) Two versions of the assembled PCB-based sample holder (with vertically and horizontally-placed SMA connectors, from FR4 or Rogers 4003c laminate, respectively). b) Sample holder mounted on the optical setup from A.1 with a connected SMA cable from the MW source. c) Patterned using photolithography and metal sputtering 25mm glass coverslip. d) Optical windows 40 μm wide and several mm long between the ground and the central wire of the CPW microwave antenna.

A.3 Patterned microscopy coverslips

Most of the microscopy samples greatly profit from having markers for navigation, which can be very tricky with a high-NA objective. That is why I fabricated patterned coverslips with navigation markers and, optionally, electrodes for grounding and/or applying electrical bias (Fig. A.4). Starting from a tedious coating/photolithography/sputtering/lift-off process, I also employed a resist-free 1-step deposition process through a fabricated stencil mask in a silicon nitride membrane.

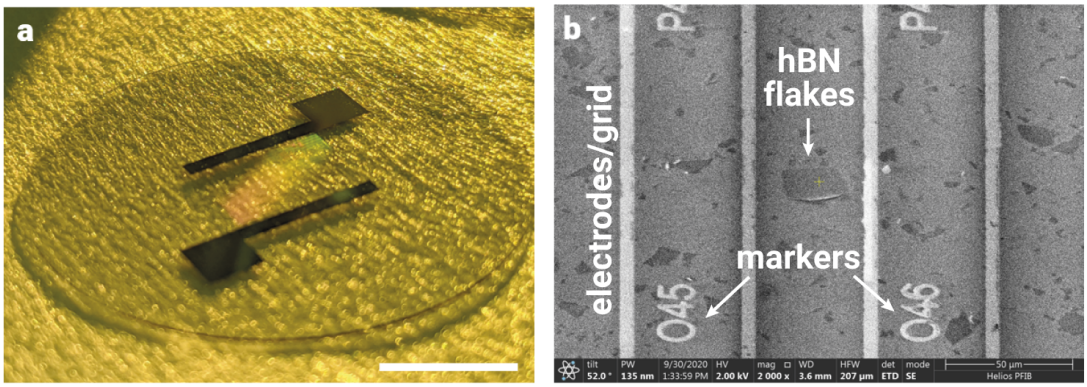

Figure A.4 – a) Patterned microscopy coverslip with a grid of markers and interdigitated electrodes. b) SEM zoom-in into a central region of the patterned coverslip. Field of view is similar to that of a 60x microscope objective. Scale bar: 10 mm (a), 50 μm (b)

B List of publications

While the chapters of this thesis are composed of my most significant contributions, there were several more publications during my PhD which I co-authored. Therefore, I present them below as a part of my publication list in a chronological order, mentioning my personal contribution to each paper. Other publications from my undergraduate studies can be found in the attached CV at the end of the thesis.

1. *Fluorescent Nanodiamonds as Versatile Intracellular Temperature Sensors.* **Evgenii Glushkov**, Vytautas Navikas, Aleksandra Radenovic. CHIMIA International Journal for Chemistry, 73, 1, (2019), pp. 73-77(5).

   I performed detailed literature analysis and wrote the text of this review paper, having discussed it with other co-authors.

2. *Waveguide-PAINT offers an open platform for large field-of-view super-resolution imaging.* Anna Archetti, **Evgenii Glushkov**, Cristian Sieben, Anton Stroganov, Aleksandra Radenovic, and Suliana Manley. Nature Communications (2019), vol. 10, no. 1, pp. 1–9.

   Together with the first author of this paper I have designed, fabricated and characterized the on-chip waveguides. I have also written a part of the manuscript, prepared several figures, and proof-read and corrected the paper.

3. *Wide-field spectral super-resolution mapping of optically active defects in hBN.* Jean Comtet, **Evgenii Glushkov**, Vytautas Navikas, Jiandong Feng, Vitaliy Babenko, Stephan Hofmann, Kenji Watanabe, Takashi Taniguchi, Aleksandra Radenovic. Nano Lett. (2019), 19, 4, 2516–2523.

   I aided in preparing the samples, including hBN exfoliation and transfer, helped with data analysis and interpretation of results. I have also discussed the results with co-authors, proof-read and corrected the whole manuscript.

4. *Facile Production of Hexagonal Boron Nitride Nanoparticles by Cryogenic Exfoliation.* Ngoc My Hanh Duong, **Evgenii Glushkov**, Andrey Chernev, Vytautas Navikas, Jean Comtet, Minh Anh Phan Nguyen, Milos Toth, Aleksandra Radenovic, Toan Trong Tran, Igor Aharonovich. Nano Lett. (2019), 19, 8, 5417–5422.

   I performed SMLM imaging of hBN nanoflakes, analysed blinking statistics of emitters in them, wrote part of the manuscript, and aided in making figures. I have also discussed the results, proof-read and corrected the whole manuscript.

5. *Waveguide-based platform for large-FOV imaging of optically-active defects in 2D materials.* **Evgenii Glushkov**, Anna Archetti, Anton Stroganov, Jean Comtent, Mukeshchand Thakur, Vytautas Navikas, Martina Lihter, Juan Marin Gonzalez, VItaliy Babenko, Stephan Hofmann, Suliana Manley, Aleksandra Radenovic. ACS Photonics (2019), 6, 12, 3100–3107.

   I have designed, fabricated and characterized the waveguide chips. I have further performed the transfer of hBN into the imaging wells and all the imaging experiments mentioned in the paper. I have analysed the data, made the figures and wrote the paper.

6. *Direct observation of water mediated single proton transport between hBN surface defects.* Jean Comtet, Benoit Grosjean, **Evgenii Glushkov**, Ahmet Avsar, Kenji Watanabe, Takashi Taniguchi, Rodolphe Vuilleumier, Marie-Laure Bocquet and Aleksandra Radenovic. Nature Nanotechnology (2020), 15, 7, 598-604.

   I have observed the effect and discussed it with the lead author of the paper. I have further aided with sample preparation, characterization experiments and data interpretation. I have also discussed the results, proof-read and corrected the whole manuscript.

7. *Direct growth of hexagonal boron nitride on photonic chips for high-throughput characterization.* **Evgenii Glushkov**, Noah Mendelson, Andrey Chernev, Ritika Ritika, Martina Lihter, Reza R. Zamani, Jean Comtet, Vytautas Navikas, Igor Aharonovich, Aleksandra Radenovic. ACS Photonics (2021) 8, 7, 2033–2040.

   I have designed, fabricated and characterized the waveguide chips. I have further performed the super-resolution imaging of as-grown and transferred hBN, analysed the data, made most of the figures and wrote most of the paper with input from other co-authors.

8. *Anomalous interfacial dynamics of single proton charges in binary aqueous solutions.* Jean Comtet, Archith Rayabharam, **Evgenii Glushkov**, Miao Zhang, Avsar Ahmet, Kenji Watanabe, Takashi Taniguchi, Narayana R Aluru, Aleksandra Radenovic. (2021) arXiv, arXiv: 2101.00231 (**accepted in Science Advances**)

   I have performed imaging experiments and and discussed them with the lead author of the paper. I have further aided with sample preparation and data interpretation. I have also discussed the results, proof-read and corrected the whole manuscript.

9. *Engineering optically active defects in hexagonal boron nitride using focused ion beam and water.* **Evgenii Glushkov**, Michal Macha, Esther Rath, Vytautas Navikas, Nathan Ronceray, Cheol Yeon Cheon, Ahmet Avsar, Ahmed Aqeel, Kenji Watanabe, Takashi Taniguchi, Ivan Shorubalko, Andras Kis, Georg Fantner and Aleksandra Radenovic. (2021) (**under review**)

   I have designed the study, observed the effects, and performed the optical imaging experiments. I have also coordinated the work of other co-authors, did the data analysis, made most of the figures and drafted the main text of the paper with the input from all co-authors.

Bibliography

1. Doris, B. *et al. Extreme scaling with ultra-thin Si channel MOSFETs* in *Digest. International Electron Devices Meeting,* (2002), 267–270.
2. Jeong, W. *et al. True 7nm platform technology featuring smallest FinFET and smallest SRAM cell by EUV, special constructs and 3 rd generation single diffusion break* in *2018 IEEE Symposium on VLSI Technology* (2018), 59–60.
3. McCarthy, B. H. & Ponedal, S. *IBM Unveils World's First 2 Nanometer Chip Technology, Opening a New Frontier for Semiconductors* 2021. https://newsroom.ibm.com/2021-05-06-IBM-Unveils-Worlds-First-2-Nanometer-Chip-Technology,-Opening-a-New-Frontier-for-Semiconductors.
4. Petrucci, R. H., Herring, F. G., Bissonnette, C. & Madura, J. D. *General chemistry: principles and modern applications* (Pearson, 2017).
5. *Bonding in Metals* [Online; accessed 2021-06-22]. Aug. 25, 2020. https://chem.libretexts.org/@go/page/36874.
6. Aharonovich, I., Englund, D. & Toth, M. Solid-state single-photon emitters. *Nature Photonics* **10,** 631–641. ISSN: 17494893. http://dx.doi.org/10.1038/nphoton.2016.186 (2016).
7. Alkauskas, A., McCluskey, M. D. & Van De Walle, C. G. Tutorial: Defects in semiconductors - Combining experiment and theory. *Journal of Applied Physics* **119.** ISSN: 10897550. http://dx.doi.org/10.1063/1.4948245 (2016).
8. Heremans, F. J., Yale, C. G. & Awschalom, D. D. Control of Spin Defects in Wide-Bandgap Semiconductors for Quantum Technologies. *Proceedings of the IEEE* **104,** 2009–2023. ISSN: 15582256 (2016).
9. Schubert, E. F. *Doping in III-V semiconductors* (E. Fred Schubert, 2015).
10. Erwin, S. C. *et al.* Doping semiconductor nanocrystals. *Nature* **436,** 91–94. ISSN: 00280836. https://doi.org/10.1038/nature03832 (2005).
11. Mizuochi, N. *et al.* Electrically driven single-photon source at room temperature in diamond. *Nature Photonics* **6,** 299–303. ISSN: 17494885. https://doi.org/10.1038/nphoton.2012.75 (2012).

12. Fabbri, F. *et al.* Novel near-infrared emission from crystal defects in MoS2 multilayer flakes. *Nature Communications* **7,** 1–7. ISSN: 20411723. http://dx.doi.org/10.1038/ncomms13044 (2016).

13. Siyushev, P. *et al.* Photoelectrical imaging and coherent spin-state readout of single nitrogen-vacancy centers in diamond. *Science* **363,** 728–731. ISSN: 10959203 (2019).

14. Watanabe, K., Taniguchi, T. & Kanda, H. Direct-bandgap properties and evidence for ultraviolet lasing of hexagonal boron nitride single crystal. *Nature Materials* **3,** 404–409. ISSN: 14761122 (2004).

15. Toth, M. & Aharonovich, I. Single Photon Sources in Atomically Thin Materials. *Annual Review of Physical Chemistry* **70,** 123–142. ISSN: 0066426X (2019).

16. Atatüre, M., Englund, D., Vamivakas, N., Lee, S. Y. & Wrachtrup, J. Material platforms for spin-based photonic quantum technologies. *Nature Reviews Materials* **3,** 38–51. ISSN: 20588437. http://dx.doi.org/10.1038/s41578-018-0008-9 (2018).

17. Balasubramanian, G. *et al.* Nanoscale imaging magnetometry with diamond spins under ambient conditions. *Nature* **455,** 648–651. ISSN: 0028-0836. http://www.nature.com/doifinder/10.1038/nature07278 (2008).

18. Kucsko, G. *et al.* Nanometre-scale thermometry in a living cell. *Nature* **500,** 54–58. ISSN: 00280836 (2013).

19. Holzgrafe, J. *et al.* Nanoscale NMR Spectroscopy Using Nanodiamond Quantum Sensors. *Physical Review Applied* **13,** 1. ISSN: 23317019. https://doi.org/10.1103/PhysRevApplied.13.044004 (2020).

20. Blok, M., Kalb, N., Reiserer, A., Taminiau, T. & Hanson, R. Towards quantum networks of single spins: analysis of a quantum memory with an optical interface in diamond. *Faraday discussions* **184,** 173–182 (2015).

21. Dolde, F. *et al.* Room-temperature entanglement between single defect spins in diamond. *Nature Physics* **9,** 139–143 (2013).

22. Waldherr, G. *et al.* Quantum error correction in a solid-state hybrid spin register. *Nature* **506,** 204–207. ISSN: 00280836. arXiv: 1309.6424 (2014).

23. Zaitsev, A. *Optical Properties of Diamond* ISBN: 9783540665823 (2001).

24. Aharonovich, I., Englund, D. & Toth, M. Solid-state single-photon emitters. *Nature Publishing Group* **10,** 631–641. ISSN: 1749-4885 (2016).

25. Aharonovich, I. *et al.* Diamond-based single-photon emitters. *Reports on Progress in Physics* **74,** 076501. ISSN: 0034-4885 (2011).

26. Schirhagl, R., Chang, K., Loretz, M. & Degen, C. L. Nitrogen-vacancy centers in diamond: Nanoscale sensors for physics and biology. *Annual Review of Physical Chemistry* **65,** 83–105. ISSN: 0066426X (2014).

27. Dolde, F. *et al.* Electric-field sensing using single diamond spins. *Nature Physics* **7,** 459–463. ISSN: 17452473. arXiv: 1103.3432. http://dx.doi.org/10.1038/nphys1969 (2011).

28. Petrakova, V. *et al.* Charge-sensitive fluorescent nanosensors created from nanodiamonds. *Nanoscale* **7,** 12307–11. ISSN: 2040-3372. http://pubs.rsc.org/en/content/articlehtml/2015/nr/c5nr00712g (2015).

29. Maze, J. R. *et al.* Properties of nitrogen-vacancy centers in diamond: The group theoretic approach. *New Journal of Physics* **13,** 1–30. ISSN: 13672630. arXiv: 1010.1338 (2011).

30. Doherty, M. W. *et al.* Electronic properties and metrology applications of the diamond NV - Center under pressure. *Physical Review Letters* **112,** 1–6. ISSN: 00319007. arXiv: arXiv:1305.2291v3 (2014).

31. Toyli, D. M., De Las Casas, C. F., Christle, D. J., Dobrovitski, V. V. & Awschalom, D. D. Fluorescence thermometry enhanced by the quantum coherence of single spins in diamond. *PNAS* **110,** 8417–8421. ISSN: 00278424 (2013).

32. Gruber, A. *et al.* Scanning Confocal Optical Microscopy and Magnetic Resonance on Single Defect Centers. *Science* **276,** 2012–2014. ISSN: 00368075. http://www.sciencemag.org/cgi/doi/10.1126/science.276.5321.2012 (1997).

33. Gali, Á. Ab initio theory of the nitrogen-vacancy center in diamond. *Nanophotonics* **8,** 1907–1943. ISSN: 21928614 (2019).

34. Harrison, J., Sellars, M. J. & Manson, N. B. Measurement of the optically induced spin polarisation of N-V centres in diamond. *Diamond and Related Materials* **15,** 586–588. ISSN: 09259635 (2006).

35. Robledo, L., Bernien, H., Sar, T. V. D. & Hanson, R. Spin dynamics in the optical cycle of single nitrogen-vacancy centres in diamond. *New Journal of Physics* **13.** ISSN: 13672630. arXiv: 1010.1192 (2011).

36. Aslam, N., Waldherr, G., Neumann, P., Jelezko, F. & Wrachtrup, J. Photo-induced ionization dynamics of the nitrogen vacancy defect in diamond investigated by single-shot charge state detection. *New Journal of Physics* **15.** ISSN: 13672630. arXiv: 1209.0268 (2013).

37. Glushkov, E., Navikas, V. & Radenovic, A. Fluorescent nanodiamonds as versatile intracellular temperature sensors. *Chimia* **73,** 73–77. ISSN: 00094293 (2019).

38. Nguyen, C. T. *et al.* All-optical nanoscale thermometry with silicon-vacancy centers in diamond. *Applied Physics Letters* **112.** ISSN: 00036951. arXiv: 1708.05419. http://arxiv.org/abs/1708.05419 (2018).

39. Fan, J. W. *et al.* Germanium-Vacancy Color Center in Diamond as a Temperature Sensor. *ACS Photonics* **5,** 765–770. ISSN: 23304022. arXiv: 1709.00456. http://pubs.acs.org/doi/10.1021/acsphotonics.7b01465 (2018).

40. Alkahtani, M. *et al.* Tin-vacancy in diamonds for luminescent thermometry. *Applied Physics Letters* **112.** ISSN: 00036951 (2018).

41. Alkahtani, M. H. *et al.* Fluorescent nanodiamonds for luminescent thermometry in the biological transparency window. *Optics Letters* **43,** 3317. ISSN: 0146-9592 (2018).

42. Neu, E. *et al.* Single photon emission from silicon-vacancy colour centres in chemical vapour deposition nano-diamonds on iridium. *New Journal of Physics* **13,** 025012 (2011).

43. Bradac, C., Gao, W., Forneris, J., Trusheim, M. E. & Aharonovich, I. Quantum nanophotonics with group IV defects in diamond. *Nature Communications* **10,** 1–13. ISSN: 20411723. arXiv: 1906.10992 (2019).

44. Hemelaar, S. R. *et al.* Nanodiamonds as multi-purpose labels for microscopy. *Scientific Reports* **7,** 720. ISSN: 2045-2322. http://www.nature.com/articles/s41598-017-00797-2 (2017).

45. Shenderova, O. *et al.* Commercial quantities of ultrasmall fluorescent nanodiamonds containing color centers. *SPIE Proceedings* **10118,** 1–16 (2017).

46. Liu, M., Kitai, A. H. & Mascher, P. Point defects and luminescence centres in zinc oxide and zinc oxide doped with manganese. *Journal of Luminescence* **54,** 35–42. ISSN: 00222313 (1992).

47. Morfa, A. J. *et al.* Single-photon emission and quantum characterization of zinc oxide defects. *Nano Letters* **12,** 949–954. ISSN: 15306984 (2012).

48. Choi, S. *et al.* Single photon emission from ZnO nanoparticles. *Applied Physics Letters* **104.** ISSN: 00036951. http://dx.doi.org/10.1063/1.4872268 (2014).

49. Jungwirth, N. R. *et al.* A single-molecule approach to ZnO defect studies: Single photons and single defects. *Journal of Applied Physics* **116.** ISSN: 10897550. http://dx.doi.org/10.1063/1.4890979 (2014).

50. Jungwirth, N. R., Chang, H. S., Jiang, M. & Fuchs, G. D. Polarization spectroscopy of defect-based single photon sources in ZnO. *ACS Nano* **10,** 1210–1215. ISSN: 1936086X (2016).

51. Son, N. T. *et al.* Divacancy in 4H-SiC. *Physical Review Letters* **96,** 8–11. ISSN: 10797114 (2006).

52. Koehl, W. F., Buckley, B. B., Heremans, F. J., Calusine, G. & Awschalom, D. D. Room temperature coherent control of defect spin qubits in silicon carbide. *Nature* **479,** 84–87. ISSN: 00280836 (2011).

53. Christle, D. J. *et al.* Isolated electron spins in silicon carbide with millisecond coherence times. *Nature Materials* **14,** 160–163. ISSN: 14764660. arXiv: 1406.7325 (2015).

54. Castelletto, S. *et al.* A silicon carbide room-temperature single-photon source. *Nature Materials* **13,** 8–13. ISSN: 1476-1122 (2014).

55. Widmann, M. *et al.* Coherent control of single spins in silicon carbide at room temperature. *Nature Materials* **14,** 164–168. ISSN: 14764660 (2015).

56. Kraus, H. *et al.* Magnetic field and temperature sensing with atomic-scale spin defects in silicon carbide. *Scientific Reports* **4.** ISSN: 20452322. arXiv: 1403.7741 (2014).

57. Mak, K. F. & Shan, J. Photonics and optoelectronics of 2D semiconductor transition metal dichalcogenides. *Nature Photonics* **10,** 216–226. ISSN: 17494893 (2016).

58. Caldwell, J. D. *et al.* Photonics with hexagonal boron nitride. *Nature Reviews Materials* **4.** ISSN: 2058-8437 (2019).

59. Geim, A. K. & Grigorieva, I. V. Van der Waals heterostructures. *Nature* **499,** 419–425. ISSN: 00280836. arXiv: 1307.6718 (2013).

60. Novoselov, K. S., Mishchenko, A., Carvalho, A. & Castro Neto, A. H. 2D materials and van der Waals heterostructures. *Science* **353.** ISSN: 0036-8075. https://science.sciencemag.org/content/353/6298/aac9439 (2016).

61. Morozov, S. V. *et al.* Giant intrinsic carrier mobilities in graphene and its bilayer. *Physical Review Letters* **100,** 11–14. ISSN: 00319007 (2008).

62. Dean, C. R. *et al.* Boron nitride substrates for high-quality graphene electronics. *Nature Nanotechnology* **5,** 722–726. ISSN: 17483395 (2010).

63. Kretinin, A. V. *et al.* Electronic properties of graphene encapsulated with different two-dimensional atomic crystals. *Nano Letters* **14,** 3270–3276. ISSN: 15306992 (2014).

64. Cao, Y. *et al.* Unconventional superconductivity in magic-angle graphene superlattices. *Nature* **556,** 43–50. ISSN: 14764687 (2018).

65. Yankowitz, M. *et al.* Tuning superconductivity in twisted bilayer graphene. *Science* **363,** 1059–1064. ISSN: 10959203. arXiv: 1808.07865 (2019).

66. Koperski, M. *et al.* Single photon emitters in exfoliated WSe2 structures. *Nature Nanotechnology* **10,** 503–506. ISSN: 17483395. arXiv: 1411.2774. https://doi.org/10.1038/nnano.2015.67 (2015).

67. Srivastava, A. *et al.* Optically active quantum dots in monolayer WSe2. *Nature Nanotechnology* **10,** 491–496. ISSN: 17483395. arXiv: 1411.0025. https://doi.org/10.1038/nnano.2015.60 (2015).

68. Chakraborty, C., Kinnischtzke, L., Goodfellow, K. M., Beams, R. & Vamivakas, A. N. Voltage-controlled quantum light from an atomically thin semiconductor. *Nature Nanotechnology* **10,** 507–511. ISSN: 17483395. https://doi.org/10.1038/nnano.2015.79 (2015).

69. He, Y. M. *et al.* Single quantum emitters in monolayer semiconductors. *Nature Nanotechnology* **10,** 497–502. ISSN: 17483395. https://doi.org/10.1038/nnano.2015.75 (2015).

70. Chow, P. K. *et al.* Defect-induced photoluminescence in monolayer semiconducting transition metal dichalcogenides. *ACS Nano* **9,** 1520–1527. ISSN: 1936086X (2015).

71. Shepard, G. D. *et al.* Nanobubble induced formation of quantum emitters in monolayer semiconductors. *2D Materials* **4.** ISSN: 20531583. arXiv: 1612.06416 (2017).

72. Darlington, T. P. *et al.* Imaging strain-localized excitons in nanoscale bubbles of monolayer WSe2 at room temperature. *Nature Nanotechnology* **15,** 854–860. ISSN: 17483395. arXiv: 2003.01789. http://dx.doi.org/10.1038/s41565-020-0730-5 (2020).

73. Kern, J. *et al.* Nanoscale Positioning of Single-Photon Emitters in Atomically Thin WSe2. *Advanced Materials* **28,** 7101–7105. ISSN: 15214095 (2016).

74. Branny, A., Kumar, S., Proux, R. & Gerardot, B. D. Deterministic strain-induced arrays of quantum emitters in a two-dimensional semiconductor. *Nature Communications* **8,** 1–7. ISSN: 20411723 (2017).

75. Kianinia, M. *et al.* Robust Solid-State Quantum System Operating at 800 K. *ACS Photonics* **4,** 768–773. ISSN: 23304022 (2017).

76. Taniguchi, T. & Watanabe, K. Synthesis of high-purity boron nitride single crystals under high pressure by using Ba–BN solvent. *Journal of crystal growth* **303,** 525–529 (2007).

77. Duclaux, L., Nysten, B., Issi, J.-P. & Moore, A. Structure and low-temperature thermal conductivity of pyrolytic boron nitride. *Physical Review B* **46.** https://journals.aps.org/prb/pdf/10.1103/PhysRevB.46.3362 (1992).

78. Greim, J. & Schwetz, K. A. Boron Carbide, Boron Nitride, and Metal Borides. *Ullmann's Encyclopedia of Industrial Chemistry* (2006).

79. Engler, M. & Ruisinger, B. Anwendungen von Metallurgie bis Kosmetik. *Ceramic Forum International* **12,** 25–29 (2016).

80. Liu, S. *et al.* Large-Scale Growth of High-Quality Hexagonal Boron Nitride Crystals at Atmospheric Pressure from an Fe-Cr Flux. *Crystal Growth and Design* **17,** 4932–4935. ISSN: 15287505 (2017).

81. Unuchek, D. *et al.* Room-temperature electrical control of exciton flux in a van der Waals heterostructure. *Nature* **560,** 340–344. ISSN: 14764687 (2018).

82. Unuchek, D. *et al.* Valley-polarized exciton currents in a van der Waals heterostructure. *Nature Nanotechnology* **14,** 1104–1109. ISSN: 17483395. http://dx.doi.org/10.1038/s41565-019-0559-y (2019).

83. Esfandiar, A. *et al.* Size effect in ion transport through angstrom-scale slits. *Science* **358,** 511–513. ISSN: 10959203 (2017).

84. Fumagalli, L. *et al.* Anomalously low dielectric constant of confined water. *Science* **360,** 1339–1342. ISSN: 10959203 (2018).

85. Novoselov, K. S. *et al.* Two-dimensional atomic crystals. *Proceedings of the National Academy of Sciences* **102,** 10451–10453. ISSN: 00278424 (2005).

86. Song, X. *et al.* Chemical vapor deposition growth of large-scale hexagonal boron nitride with controllable orientation. *Nano Research* **8,** 3164–3176. ISSN: 19980000 (2015).

87. Wu, Q. *et al.* Single Crystalline Film of Hexagonal Boron Nitride Atomic Monolayer by Controlling Nucleation Seeds and Domains. *Scientific Reports* **5,** 1–8. ISSN: 20452322 (2015).

88. Caneva, S. *et al.* Nucleation control for large, single crystalline domains of monolayer hexagonal boron nitride via Si-doped Fe catalysts. *Nano Letters* **15,** 1867–1875. ISSN: 15306992 (2015).

89. Caneva, S. *et al.* Controlling Catalyst Bulk Reservoir Effects for Monolayer Hexagonal Boron Nitride CVD. *Nano Letters* **16,** 1250–1261. ISSN: 15306992 (2016).

90. Nicolosi, V., Chhowalla, M., Kanatzidis, M. G., Strano, M. S. & Coleman, J. N. Liquid exfoliation of layered materials. *Science* **340,** 72–75. ISSN: 10959203 (2013).

91. Li, L. H. *et al.* Large-scale mechanical peeling of boron nitride nanosheets by low-energy ball milling. *Journal of Materials Chemistry* **21,** 11862–11866. ISSN: 09599428 (2011).

92. Behura, S. *et al.* Chemical Interaction-Guided, Metal-Free Growth of Large-Area Hexagonal Boron Nitride on Silicon-Based Substrates. *ACS Nano* **11,** 4985–4994. ISSN: 1936086X (2017).

93. Li, C. *et al.* Scalable and Deterministic Fabrication of Quantum Emitter Arrays from Hexagonal Boron Nitride. *Nano Letters* **21,** 3626–3632. ISSN: 1530-6984. arXiv: 2103.02875. http://arxiv.org/abs/2103.02875 (2021).

94. Elshaari, A. W. *et al.* Deterministic Integration of hBN Emitter in Silicon Nitride Photonic Waveguide. *Advanced Quantum Technologies* **2100032,** 1–9. ISSN: 25119044 (2021).

95. Tran, T. T., Bray, K., Ford, M. J., Toth, M. & Aharonovich, I. Quantum emission from hexagonal boron nitride monolayers. *Nature Nanotechnology* **11,** 37–41. ISSN: 17483395. http://dx.doi.org/10.1038/nnano.2015.242 (2016).

96. Tran, T. T. *et al.* Quantum Emission from Defects in Single-Crystalline Hexagonal Boron Nitride. *Physical Review Applied* **5,** 2–6. ISSN: 23317019. arXiv: 1603.02305 (2016).

97. Choi, S. *et al.* Engineering and Localization of Quantum Emitters in Large Hexagonal Boron Nitride Layers. *ACS Applied Materials & Interfaces* **8,** 29642–29648. ISSN: 1944-8244. https://doi.org/10.1021/acsami.6b09875 (2016).

98. Tran, T. T. *et al.* Robust Multicolor Single Photon Emission from Point Defects in Hexagonal Boron Nitride. *ACS Nano* **10,** 7331–7338. ISSN: 1936086X. arXiv: 1603.09608 (2016).

99. Fischer, M. *et al.* Controlled generation of luminescent centers in hexagonal boron nitride by irradiation engineering. *Science Advances* **7.** ISSN: 2375-2548 (2021).

100. Yim, D., Yu, M., Noh, G., Lee, J. & Seo, H. Polarization and Localization of Single-Photon Emitters in Hexagonal Boron Nitride Wrinkles. *ACS Applied Materials and Interfaces* **12,** 36362–36369. ISSN: 19448252 (2020).

101. Proscia, N. V. *et al.* Near-deterministic activation of room-temperature quantum emitters in hexagonal boron nitride. *Optica* **5,** 1128–1134. https://doi.org/10.1364/OPTICA.5.001128 (2018).

102. Hou, S. *et al.* Localized emission from laser-irradiated defects in 2D hexagonal boron nitride. *2D Materials* **5.** ISSN: 20531583 (2018).

103. Ziegler, J. *et al.* Deterministic Quantum Emitter Formation in Hexagonal Boron Nitride via Controlled Edge Creation. *Nano Letters* **19,** 2121–2127. ISSN: 15306992 (2019).

104. Kianinia, M., White, S., Fröch, J. E., Bradac, C. & Aharonovich, I. Generation of Spin Defects in Hexagonal Boron Nitride. *ACS Photonics* **7,** 2147–2152. ISSN: 23304022 (2020).

105. Fournier, C. *et al.* Position-controlled quantum emitters with reproducible emission wavelength in hexagonal boron nitride. *Nature Communications* **12.** ISSN: 23318422. arXiv: 2011.12224. http://arxiv.org/abs/2011.12224 (2021).

106. Gao, X. *et al.* Femtosecond Laser Writing of Spin Defects in Hexagonal Boron Nitride. *ACS Photonics* **8,** 994–1000. https://doi.org/10.1021/acsphotonics.0c01847 (2021).

107. Noh, G. *et al.* Stark Tuning of Single-Photon Emitters in Hexagonal Boron Nitride. *Nano Letters* **18,** 4710–4715. ISSN: 15306992. arXiv: 1807.04945 (2018).

108. Nikolay, N. *et al.* Very Large and Reversible Stark-Shift Tuning of Single Emitters in Layered Hexagonal Boron Nitride. *Physical Review Applied* **11,** 1. ISSN: 23317019. arXiv: 1812.02530. https://doi.org/10.1103/PhysRevApplied.11.041001 (2019).

109. Mendelson, N. *et al.* Engineering and Tuning of Quantum Emitters in Few-Layer Hexagonal Boron Nitride. *ACS Nano* **13,** 3132–3140. ISSN: 1936086X (2019).

110. Scavuzzo, A. *et al.* Electrically tunable quantum emitters in an ultrathin graphene–hexagonal boron nitride van der Waals heterostructure. *Applied Physics Letters* **114,** 62104. https://doi.org/10.1063/1.5067385 (2019).

111. Grosso, G. *et al.* Tunable and high-purity room temperature single-photon emission from atomic defects in hexagonal boron nitride. *Nature Communications* **8,** 1–8. ISSN: 20411723. arXiv: 1611.03515. http://dx.doi.org/10.1038/s41467-017-00810-2 (2017).

112. Xue, Y. *et al.* Anomalous Pressure Characteristics of Defects in Hexagonal Boron Nitride Flakes. *ACS Nano* **12,** 7127–7133. ISSN: 1936086X (2018).

113. Mendelson, N., Doherty, M., Toth, M., Aharonovich, I. & Tran, T. T. Strain-Induced Modification of the Optical Characteristics of Quantum Emitters in Hexagonal Boron Nitride. *Advanced Materials* **32.** ISSN: 15214095 (2020).

114. Tran, T. T. *et al.* Deterministic Coupling of Quantum Emitters in 2D Materials to Plasmonic Nanocavity Arrays. *Nano Letters* **17,** 2634–2639. ISSN: 15306992 (2017).

115. Eftekhari, Z. *et al.* Strong light emission from a defective hexagonal boron nitride monolayer coupled to near-touching random plasmonic nanounits. *Optics Letters* **46,** 1664. ISSN: 0146-9592 (2021).

116. Schell, A. W., Takashima, H., Tran, T. T., Aharonovich, I. & Takeuchi, S. Coupling Quantum Emitters in 2D Materials with Tapered Fibers. *ACS Photonics* **4,** 761–767. ISSN: 23304022. arXiv: 1701.02696 (2017).

117. Kim, S. *et al.* Integrated on Chip Platform with Quantum Emitters in Layered Materials. *Advanced Optical Materials* **7,** 1901132. ISSN: 21951071. arXiv: 1907.04546 (2019).

118. Peyskens, F., Chakraborty, C., Muneeb, M., Van Thourhout, D. & Englund, D. Integration of single photon emitters in 2D layered materials with a silicon nitride photonic chip. *Nature Communications* **10,** 1–7. ISSN: 20411723. arXiv: 1904.08841 (2019).

119. Kim, S. *et al.* Photonic crystal cavities from hexagonal boron nitride. *Nature Communications* **9,** 1–8. ISSN: 20411723. arXiv: 1801.04399. http://dx.doi.org/10.1038/s41467-018-05117-4 (2018).

120. Kim, S. *et al.* Integrated on Chip Platform with Quantum Emitters in Layered Materials. *Advanced Optical Materials* **7,** 1901132. ISSN: 21951071. arXiv: 1907.04546 (2019).

121. Fröch, J. E., Hwang, Y., Kim, S., Aharonovich, I. & Toth, M. Photonic Nanostructures from Hexagonal Boron Nitride. *Advanced Optical Materials* **7.** ISSN: 21951071 (2019).

122. Chejanovsky, N. *et al.* Single-spin resonance in a van der Waals embedded paramagnetic defect. *Nature Materials.* ISSN: 1476-4660. arXiv: 1906.05903. https://doi.org/10.1038/s41563-021-00979-4 (2021).

123. Gottscholl, A. *et al.* Initialization and read-out of intrinsic spin defects in a van der Waals crystal at room temperature. *Nature Materials* **19,** 540–545. ISSN: 14764660 (2020).

124. Stern, H. L. *et al.* Room-temperature optically detected magnetic resonance of single defects in hexagonal boron nitride. *arXiv,* 1–25. arXiv: 2103.16494. http://arxiv.org/abs/2103.16494 (2021).

125. Gottscholl, A. *et al.* Room temperature coherent control of spin defects in hexagonal boron nitride. *Science Advances* **7** (2021).

126. Kozawa, D. *et al.* Observation and spectral assignment of a family of hexagonal boron nitride lattice defects. *arXiv.* arXiv: 1909.11738. https://arxiv.org/ftp/arxiv/papers/1909/1909.11738.pdf (2019).

127. Comtet, J. *et al.* Wide-Field Spectral Super-Resolution Mapping of Optically Active Defects in Hexagonal Boron Nitride. *Nano Letters* **19,** 2516–2523. ISSN: 15306992 (2019).

128. Hayee, F. *et al.* Revealing multiple classes of stable quantum emitters in hexagonal boron nitride with correlated optical and electron microscopy. *Nature Materials.* ISSN: 14764660 (2020).

129. Abdi, M., Chou, J. P., Gali, A. & Plenio, M. B. Color Centers in Hexagonal Boron Nitride Monolayers: A Group Theory and Ab Initio Analysis. *ACS Photonics* **5,** 1967–1976. ISSN: 23304022. arXiv: 1709.05414 (2018).

130. Feng, J. *et al.* Imaging of Optically Active Defects with Nanometer Resolution. *Nano Letters* **18,** 1739–1744. ISSN: 15306992. arXiv: 1706.06313 (2018).

131. Mendelson, N. *et al.* Grain Dependent Growth of Bright Quantum Emitters in Hexagonal Boron Nitride. *Advanced Optical Materials* **9,** 1–8. ISSN: 21951071. arXiv: 2005.10699 (2021).

132. Comtet, J. *et al.* Direct observation of water-mediated single-proton transport between hBN surface defects. *Nature Nanotechnology* **15,** 598–604. ISSN: 17483395. arXiv: 1906.09019 (2020).

133. Turiansky, M. E., Alkauskas, A., Bassett, L. C. & Van De Walle, C. G. Dangling Bonds in Hexagonal Boron Nitride as Single-Photon Emitters. *Physical Review Letters* **123.** ISSN: 10797114 (2019).

134. Tawfik, S. A. *et al.* First-principles investigation of quantum emission from hBN defects. *Nanoscale* **9,** 13575–13582. ISSN: 20403372. arXiv: 1705.05753 (2017).

135. Wu, F., Galatas, A., Sundararaman, R., Rocca, D. & Ping, Y. First-principles engineering of charged defects for two-dimensional quantum technologies. *Physical Review Materials* **1.** ISSN: 24759953. arXiv: 1710.00257 (2017).

136. Toledo, J. R. *et al.* Electron paramagnetic resonance signature of point defects in neutron-irradiated hexagonal boron nitride. *Physical Review B* **98,** 1–6. ISSN: 24699969 (2018).

137. Weston, L., Wickramaratne, D., Mackoit, M., Alkauskas, A. & Van De Walle, C. G. Native point defects and impurities in hexagonal boron nitride. *Physical Review B* **97,** 1–13. ISSN: 24699969 (2018).

138. Gloter, A., Urita, K., Iijima, S., Suenaga, K. & Hashimoto, A. Direct evidence for atomic defects in graphene layers. *Nature* **430,** 870–873. http://dx.doi.org/10.1038/nature02817 (2004).

139. Jin, C., Lin, F., Suenaga, K. & Iijima, S. Fabrication of a freestanding boron nitride single layer and Its defect assignments. *Physical Review Letters* **102,** 3–6. ISSN: 00319007 (2009).

140. Kotakoski, J., Jin, C. H., Lehtinen, O., Suenaga, K. & Krasheninnikov, A. V. Electron knock-on damage in hexagonal boron nitride monolayers. *Physical Review B - Condensed Matter and Materials Physics* **82,** 1–4. ISSN: 10980121 (2010).

141. Graham, R. J. & Ravi, K. V. Cathodoluminescence investigation of impurities and defects in single crystal diamond grown by the combustion-flame method. *Applied Physics Letters* **60,** 1310–1312. ISSN: 00036951 (1992).

142. Jaffrennou, P. *et al.* Origin of the excitonic recombinations in hexagonal boron nitride by spatially resolved cathodoluminescence spectroscopy. *Journal of Applied Physics* **102,** 6–9. ISSN: 00218979. arXiv: 0707.0599 (2007).

143. Wong, D. *et al.* Characterization and manipulation of individual defects in insulating hexagonal boron nitride using scanning tunnelling microscopy. *Nature Nanotechnology* **10,** 949–953. ISSN: 17483395 (2015).

144. Fei, Z. *et al.* Electronic and plasmonic phenomena at graphene grain boundaries. *Nature Nanotechnology* **8,** 821–825. ISSN: 17483395 (2013).

145. Bao, W. *et al.* Visualizing nanoscale excitonic relaxation properties of disordered edges and grain boundaries in monolayer molybdenum disulfide. *Nature Communications* **6,** 1–7. http://dx.doi.org/10.1038/ncomms8993 (2015).

146. Optical nano-imaging of gate-tunable graphene plasmons. *Nature* **487,** 77–81. ISSN: 0028-0836 (2012).

147. Ogletree, D. F. *et al.* Revealing Optical Properties of Reduced-Dimensionality Materials at Relevant Length Scales. *Advanced Materials* **27,** 5693–5719. ISSN: 15214095 (2015).

148. Ares, P. *et al.* Direct Visualization and Effects of Atomic-Scale Defects on the Opto-electronic Properties of Hexagonal Boron Nitride. *Advanced Electronic Materials.* ISSN: 2199160X (2021).

149. Wilke, V. Laser Scanning In Microscopy. *Advances in Laser Scanning and Recording* **0396,** 164–172 (1983).

150. Ploem, J. S. Laser scanning fluorescence microscopy. *Applied Optics* **26,** 3226. ISSN: 0003-6935 (1987).

151. Ishikawa-Ankerhold, H. C., Ankerhold, R. & Drummen, G. P. Advanced fluorescence microscopy techniques-FRAP, FLIP, FLAP, FRET and FLIM. *Molecules* **17,** 4047–4132. ISSN: 14203049 (2012).

152. Jelezko, F., Gaebel, T., Popa, I., Gruber, A. & Wrachtrup, J. Observation of Coherent Oscillations in a Single Electron Spin. *Physical Review Letters* **92,** 1–4. ISSN: 10797114 (2004).

153. Gaebel, T. *et al.* Room-temperature coherent coupling of single spins in diamond. *Nature Physics* **2,** 408–413. ISSN: 17452481 (2006).

154. Batalov, A. *et al.* Temporal coherence of photons emitted by single nitrogen-vacancy defect centers in diamond using optical rabi-oscillations. *Physical Review Letters* **100,** 1–4. ISSN: 00319007 (2008).

155. Marvin, M. *Microscopy apparatus* US Patent 3,013,467. 1961.

156. Webb, R. H. Confocal optical microscopy. *Rep. Prog. Phys.* **59,** 427–471 (1996).

157. Macklin, J. J., Trautman, J. K., Harris, T. D. & Brus, L. E. Imaging and Time-Resolved Spectroscopy of Single Molecules at an Interface. *Science* **272,** 255–258. ISSN: 0036-8075. https://science.sciencemag.org/content/272/5259/255 (1996).

158. Nirmal, M. *et al.* Fluorescence intermittency in single cadmium selenide nanocrystals. *Nature* **383,** 802–804. ISSN: 1476-4687. https://doi.org/10.1038/383802a0 (1996).

159. Prasad, V., Semwogerere, D. & Weeks, E. R. Confocal microscopy of colloids. *Journal of Physics Condensed Matter* **19,** 1–25. ISSN: 09538984 (2007).

160. Brakenhoff, G. J., Van Der Voort, H. T., Van Spronsen, E. A., Linnemans, W. A. & Nanninga, N. Three-Dimensional chromatin distribution in neuroblastoma nuclei shown by confocal scanning laser microscopy. *Nature* **317,** 748–749. ISSN: 00280836 (1985).

161. White, J. G., Amos, W. B. & Fordham, M. An evaluation of confocal versus conventional imaging of biological structures by fluorescence light microscopy. *The Journal of Cell Biology* **105,** 41–48. ISSN: 00219525 (1987).

162. Lipson, A. *Optical physics* 4th ed. eng. ISBN: 9780521493451 (Cambridge University Press, Cambridge, 2011).

163. Lippincott-Schwartz, J. & Patterson, G. H. Development and use of fluorescent protein markers in living cells. *Science* **300,** 87–91. ISSN: 00368075 (2003).

164. Garini, Y., Vermolen, B. J. & Young, I. T. From micro to nano: Recent advances in high-resolution microscopy. *Current Opinion in Biotechnology* **16,** 3–12. ISSN: 09581669 (2005).

165. Pohl, D. W., Denk, W. & Lanz, M. Optical stethoscopy: Image recording with resolution $\lambda/20$. *Applied Physics Letters* **44,** 651–653. ISSN: 00036951 (1984).

166. Betzig, E., Trautman, J. K., Harris, T. D., Weiner, J. S. & Kostelak, R. L. Breaking the diffraction barrier: Optical microscopy on a nanometric scale. *Science* **251,** 1468–1470. ISSN: 00368075 (1991).

167. Erik, S. J., Novotny, L. & Xie, X. S. Near-field fluorescence microscopy based on two-photon excitation with metal tips. *Physical Review Letters* **82,** 4014–4017. ISSN: 10797114 (1999).

168. Scanning near-field optical microscopy with aperture probes: Fundamentals and applications. *Journal of Chemical Physics* **112,** 7761–7774. ISSN: 00219606 (2000).

169. Taminiau, T. H., Moerland, R. J., Segerink, F. B., Kuipers, L. & Van Hulst, N. F. $\lambda/4$ Resonance of an optical monopole antenna probed by single molecule fluorescence. *Nano Letters* **7,** 28–33. ISSN: 15306984 (2007).

170. Pohl, D. W. & Courjon, D. *Near field optics* (Springer Science & Business Media, 2012).

171. Huang, B., Bates, M. & Zhuang, X. Super-resolution fluorescence microscopy. *Annual Review of Biochemistry* **78,** 993–1016. ISSN: 00664154 (2009).

172. Heintzmann, R. & Ficz, G. Breaking the resolution limit in light microscopy. *Briefings in Functional Genomics and Proteomics* **5,** 289–301. ISSN: 14739550 (2006).

173. Beckers, J. M. Adaptive optics for astronomy: Principles, performance, and applications. *Annual Review of Astronomy and Astrophysics* **31,** 13–62. ISSN: 00664146 (1993).

174. Booth, M. J. Adaptive optics in microscopy. *Philosophical Transactions of the Royal Society A: Mathematical, Physical and Engineering Sciences* **365,** 2829–2843. ISSN: 1364503X (2007).

175. De Villiers, G. & Pike, E. R. *The limits of resolution* (CRC press, 2016).

176. Bos, A. v. d. & Dekker, A. J. d. Resolution reconsidered—Conventional approaches and an alternative. *ADVANCES IN IMAGING AND ELECTRON PHYSICS* **117.** https://www.sciencedirect.com/science/article/pii/S1076567001801142 (2001).

177. Yildiz, A. *et al.* Myosin V walks hand-over-hand: Single fluorophore imaging with 1.5-nm localization. *Science* **300,** 2061–2065. ISSN: 00368075 (2003).

178. Ober, R. J., Ram, S. & Ward, E. S. Localization Accuracy in Single-Molecule Microscopy. *Biophysical Journal* **86,** 1185–1200. ISSN: 00063495. http://dx.doi.org/10.1016/S0006-3495(04)74193-4 (2004).

179. Banterle, N., Bui, K. H., Lemke, E. A. & Beck, M. Fourier ring correlation as a resolution criterion for super-resolution microscopy. *Journal of Structural Biology* **183,** 363–367. ISSN: 10478477 (2013).

180. Descloux, A., Grußmayer, K. S. & Radenovic, A. Parameter-free image resolution estimation based on decorrelation analysis. *Nature Methods* **16,** 918–924. ISSN: 15487105 (2019).

181. Gittes, F., Mickey, B., Nettleton, J. & Howard, J. Flexural rigidity of microtubules and actin filaments measured from thermal fluctuations in shape. *Journal of Cell Biology* **120,** 923–934. ISSN: 00219525 (1993).

182. Gell, C., Berndt, M., Enderlein, J. & Diez, S. TIRF microscopy evanescent field calibration using tilted fluorescent microtubules. *Journal of Microscopy* **234,** 38–46. ISSN: 00222720 (2009).

183. Steinhauer, C., Jungmann, R., Sobey, T. L., Simmel, F. C. & Tinnefeld, P. DNA origami as a nanoscopic ruler for superresolution microscopy. *Angewandte Chemie - International Edition* **48,** 8870–8873. ISSN: 14337851 (2009).

184. Archetti, A. *et al.* Waveguide-PAINT offers an open platform for large field-of-view super-resolution imaging. *Nature Communications* **10,** 1–9. ISSN: 20411723. http://dx.doi.org/10.1038/s41467-019-09247-1 (2019).

185. Burgert, A., Letschert, S., Doose, S. & Sauer, M. Artifacts in single-molecule localization microscopy. *Histochemistry and Cell Biology* **144,** 123–131. ISSN: 1432119X (2015).

186. Jimenez, A., Friedl, K. & Leterrier, C. About samples, giving examples: Optimized Single Molecule Localization Microscopy. *Methods* **174,** 100–114. ISSN: 10959130. https://doi.org/10.1016/j.ymeth.2019.05.008 (2020).

187. Schermelleh, L. *et al.* Super-resolution microscopy demystified. *Nature Cell Biology* **21,** 72–84. ISSN: 14764679. http://dx.doi.org/10.1038/s41556-018-0251-8 (2019).

188. Lelek, M. *et al.* Single-molecule localization microscopy. *Nature Reviews Methods Primers* **1** (2021).

189. Hell, S. W. & Wichmann, J. Breaking the diffraction resolution limit by stimulated emission: stimulated-emission-depletion fluorescence microscopy. *Optics Letters* **19,** 780. ISSN: 0146-9592 (1994).

190. Klar, T. A. & Hell, S. W. Subdiffraction resolution in far-field fluorescence microscopy. *Optics Letters* **24,** 954. ISSN: 0146-9592 (1999).

191. Westphal, V. & Hell, S. W. Nanoscale resolution in the focal plane of an optical microscope. *Physical Review Letters* **94,** 1–4. ISSN: 00319007 (2005).

192. Dyba, M. & Hell, S. W. Focal Spots of Size $\lambda/23$ Open Up Far-Field Fluorescence Microscopy at 33 nm Axial Resolution. *Physical Review Letters* **88,** 4. ISSN: 10797114 (2002).

193. Hell, S. W. & Kroug, M. Ground-state-depletion fluorscence microscopy: a concept for breaking the diffraction resolution limit. *Applied Physics B Laser and Optics* **60,** 495–497 (1995).

194. Bretschneider, S., Eggeling, C. & Hell, S. W. Breaking the diffraction barrier in fluorescence microscopy by optical shelving. *Physical Review Letters* **98,** 1–4. ISSN: 00319007 (2007).

195. Hell, S. W. Far-field optical nanoscopy. *Science* **316,** 1153–1159 (2007).

196. Hofmann, M., Eggeling, C., Jakobs, S. & Hell, S. W. Breaking the diffraction barrier in fluorescence microscopy at low light intensities by using reversibly photoswitchable proteins. *Proceedings of the National Academy of Sciences* **102,** 17565–17569. ISSN: 00278424 (2005).

197. Rittweger, E., Wildanger, D. & Hell, S. W. Far-field fluorescence nanoscopy of diamond color centers by ground state depletion. *EPL* **86.** ISSN: 02955075 (2009).

198. Lukosz, W. Optical Systems with Resolving Powers Exceeding the Classical Limit. *Journal of the Optical Society of America* **56,** 1463. ISSN: 0030-3941 (1966).

199. Gustafsson, M. G. Surpassing the lateral resolution limit by a factor of two using structured illumination microscopy. *Journal of Microscopy* **198,** 82–87. ISSN: 00222720 (2000).

200. Gustafsson, M. G. Nonlinear structured-illumination microscopy: Wide-field fluorescence imaging with theoretically unlimited resolution. *Proceedings of the National Academy of Sciences* **102,** 13081–13086. ISSN: 00278424 (2005).

201. Kner, P., Chhun, B. B., Griffis, E. R., Winoto, L. & Gustafsson, M. G. Super-resolution video microscopy of live cells by structured illumination. *Nature Methods* **6,** 339–342. ISSN: 15487091 (2009).

202. Markwirth, A. *et al.* Video-rate multi-color structured illumination microscopy with simultaneous real-time reconstruction. *Nature Communications* **10,** 1–11. ISSN: 20411723. http://dx.doi.org/10.1038/s41467-019-12165-x (2019).

203. Kural, C. *et al.* Cell Biology: Kinesin and dynein move a peroxisome in vivo: A tug-of-war or coordinated movement? *Science* **308,** 1469–1472. ISSN: 00368075 (2005).

204. Betzig, E. *et al.* Imaging intracellular fluorescent proteins at nanometer resolution. *Science* **313,** 1642–1645. ISSN: 00368075 (2006).

205. Rust, M. J., Bates, M. & Zhuang, X. Sub-diffraction-limit imaging by stochastic optical reconstruction microscopy (STORM). *Nature Methods* **3,** 793–795. ISSN: 15487091 (2006).

206. Hess, S. T., Girirajan, T. P. & Mason, M. D. Ultra-high resolution imaging by fluorescence photoactivation localization microscopy. *Biophysical Journal* **91,** 4258–4272. ISSN: 00063495 (2006).

207. Sharonov, A. & Hochstrasser, R. M. Wide-field subdiffraction imaging by accumulated binding of diffusing probes. *Proceedings of the National Academy of Sciences* **103,** 18911–18916. ISSN: 0027-8424 (2006).

208. Egner, A. *et al.* Fluorescence nanoscopy in whole cells by asynchronous localization of photoswitching emitters. *Biophysical Journal* **93,** 3285–3290. ISSN: 00063495 (2007).

209. Heilemann, M. *et al.* Subdiffraction-resolution fluorescence imaging with conventional fluorescent probes. *Angewandte Chemie - International Edition* **47,** 6172–6176. ISSN: 14337851 (2008).

210. Uno, S. N. *et al.* A spontaneously blinking fluorophore based on intramolecular spirocyclization for live-cell super-resolution imaging. *Nature Chemistry* **6,** 681–689. ISSN: 17554349 (2014).

211. Zheng, Q. *et al.* Rational Design of Fluorogenic and Spontaneously Blinking Labels for Super-Resolution Imaging. *ACS Central Science* **5,** 1602–1613. ISSN: 23747951 (2019).

212. Giannone, G. *et al.* Dynamic superresolution imaging of endogenous proteins on living cells at ultra-high density. *Biophysical Journal* **99,** 1303–1310. ISSN: 15420086 (2010).

213. Lew, M. D. *et al.* Three-dimensional superresolution colocalization of intracellular protein superstructures and the cell surface in live Caulobacter crescentus. *Proceedings of the National Academy of Sciences* **108.** ISSN: 00278424 (2011).

214. Jungmann, R. *et al.* Single-molecule kinetics and super-resolution microscopy by fluorescence imaging of transient binding on DNA origami. *Nano Letters* **10,** 4756–4761. ISSN: 15306984 (2010).

215. Jungmann, R. *et al.* Multiplexed 3D cellular super-resolution imaging with DNA-PAINT and Exchange-PAINT. *Nature Methods* **11,** 313–318. ISSN: 15487105 (2014).

216. Yuan, H. *et al.* Photoluminescence Blinking of Single-Crystal Methylammonium Lead Iodide Perovskite Nanorods Induced by Surface Traps. *ACS Omega* **1,** 148–159. ISSN: 24701343 (2016).

217. Krauss, T. D. & Brus, L. E. Charge, polarizability, and photoionization of single semiconductor nanocrystals. *Physical Review Letters* **83,** 4840–4843. ISSN: 10797114 (1999).

218. Wrachtrup, J., Neumann, P., Jelezko, F., Aslam, N. & Waldherr, G. Photo-induced ionization dynamics of the nitrogen vacancy defect in diamond investigated by single-shot charge state detection. *New Journal of Physics* **15,** 013064 (2013).

219. Comtet, J. *et al.* Anomalous interfacial dynamics of single proton charges in binary aqueous solutions. *arXiv*. arXiv: 2101.00231. http://arxiv.org/abs/2101.00231 (2021).

220. Lidke, K. A., Rieger, B., Jovin, T. M. & Heintzmann, R. Superresolution by localization of quantum dots using blinking statistics. *Optics Express* **13,** 7052. ISSN: 1094-4087 (2005).

221. Wöll, D. & Flors, C. Super-resolution Fluorescence Imaging for Materials Science. *Small Methods* **1,** 1700191 (2017).

222. Kianinia, M. *et al.* All-optical control and super-resolution imaging of quantum emitters in layered materials. *Nature Communications* **9.** ISSN: 20411723. http://dx.doi.org/10.1038/s41467-018-03290-0 (2018).

223. Malein, R. N. E., Khatri, P., Ramsay, A. J. & Luxmoore, I. J. Stimulated Emission Depletion Spectroscopy of Color Centers in Hexagonal Boron Nitride. *ACS Photonics* **8,** 1007–1012. ISSN: 23304022. arXiv: 2103.01718 (2021).

224. Khatri, P., Malein, R. N. E., Ramsay, A. J. & Luxmoore, I. J. Stimulated Emission Depletion Microscopy with Color Centers in Hexagonal Boron Nitride. *arXiv preprint arXiv:2103.01718* (2021).

225. Mizuochi, N. *et al.* Electrically driven single-photon source at room temperature in diamond. *Nature Photonics* **6,** 299–303. ISSN: 17494885 (2012).

226. Hong, S. *et al.* Nanoscale magnetometry with NV centers in diamond. *MRS Bulletin* **38,** 155–161. ISSN: 08837694 (2013).

227. Nikolay, N. *et al.* Very Large and Reversible Stark Shift Tuning of Single Emitters in Layered Hexagonal Boron Nitride (2018).

228. Palacios-Berraquero, C. *et al.* Large-scale quantum-emitter arrays in atomically thin semiconductors. *Nature Communications* **8,** 1–6. ISSN: 20411723 (2017).

229. Ranjan, A. *et al.* Mechanism of soft and hard breakdown in hexagonal boron nitride 2D dielectrics. *IEEE International Reliability Physics Symposium Proceedings (IRPS),* 4A.1-1-4A.1–6. ISSN: 15417026 (2018).

230. Li, L. H. & Chen, Y. Atomically Thin Boron Nitride: Unique Properties and Applications. *Advanced Functional Materials* **26,** 2594–2608. ISSN: 16163028 (2016).

231. Merdasa, A. *et al.* supertrapät Work: Extremely Efficient Nonradiative Recombination Channels in MAPbI3 Perovskites Revealed by Luminescence Super-Resolution Imaging and Spectroscopy. *ACS Nano* **11,** 5391–5404. ISSN: 1936086X (2017).

232. Ponseca, C. S., Pullerits, T., Yartsev, A., Sundstro, V. & Scheblykin, I. G. Giant Photoluminescence Blinking of Perovskite Nanocrystals Reveals Single-Trap Control of Luminescence (2015).

233. Nicovich, P. R., Owen, D. M. & Gaus, K. Turning single-molecule localization microscopy into a quantitative bioanalytical tool. **12** (2017).

234. Moon, S. *et al.* Spectrally Resolved, Functional Super-Resolution Microscopy Reveals Nanoscale Compositional Heterogeneity in Live-Cell Membranes. *Journal of the American Chemical Society* **139,** 10944–10947. ISSN: 15205126 (2017).

235. Zhang, Z., Kenny, S. J., Hauser, M., Li, W. & Xu, K. Ultrahigh-throughput single-molecule spectroscopy and spectrally resolved super-resolution microscopy. *Nature Methods* **12,** 935–938. ISSN: 15487105 (2015).

236. Yan, R., Moon, S., Kenny, S. J. & Xu, K. Spectrally Resolved and Functional Super-resolution Microscopy via Ultrahigh-Throughput Single-Molecule Spectroscopy. *Accounts of Chemical Research* **51,** 697–705. ISSN: 15204898 (2018).

237. Kim, D., Zhang, Z. & Xu, K. Spectrally Resolved Super-Resolution Microscopy Unveils Multipath Reaction Pathways of Single Spiropyran Molecules. *Journal of the American Chemical Society* **139,** 9447–9450. ISSN: 15205126 (2017).

238. Deschout, H. *et al.* Complementarity of PALM and SOFI for super-resolution live-cell imaging of focal adhesions. *Nature Communications* **7,** 1–11 (2016).

239. Martınez, L. J. *et al.* Efficient single photon emission from a high-purity hexagonal boron nitride crystal. *Physical Review B* **94,** 1–5. ISSN: 24699969 (2016).

240. Xu, Z. Q. *et al.* Single photon emission from plasma treated 2D hexagonal boron nitride. *Nanoscale* **10,** 7957–7965. ISSN: 20403372 (2018).

241. Tran, T. T., Bray, K., Ford, M. J., Toth, M. & Aharonovich, I. Quantum emission from hexagonal boron nitride monolayers. *Nature Nanotechnology* **11,** 37–41. ISSN: 17483395 (2016).

242. Frantsuzov, P., Kuno, M., Jankó, B. & Marcus, R. A. Universal emission intermittency in quantum dots, nanorods and nanowires. *Nature Physics* **4,** 519–522. ISSN: 17452473 (2008).

243. Efros, A. L. & Nesbitt, D. J. Origin and control of blinking in quantum dots. *Nature Nanotechnology* **11,** 661–671. ISSN: 17483395 (2016).

244. Jungwirth, N. R. *et al.* Temperature Dependence of Wavelength Selectable Zero-Phonon Emission from Single Defects in Hexagonal Boron Nitride. *Nano Letters* **16,** 6052–6057. ISSN: 15306992. arXiv: 1605.04445 (2016).

245. Chejanovsky, N. *et al.* Structural Attributes and Photodynamics of Visible Spectrum Quantum Emitters in Hexagonal Boron Nitride. *Nano Letters* **16,** 7037–7045. ISSN: 15306992. arXiv: 1608.03114 (2016).

246. Dietrich, A. *et al.* Observation of Fourier transform limited lines in hexagonal boron nitride. *Physical Review B* **98,** 2–6. ISSN: 24699969 (2018).

247. Shotan, Z. *et al.* Photoinduced Modification of Single-Photon Emitters in Hexagonal Boron Nitride. *ACS Photonics* **3,** 2490–2496. ISSN: 23304022 (2016).

248. Reimers, J. R., Sajid, A., Kobayashi, R. & Ford, M. J. Understanding and Calibrating Density-Functional-Theory Calculations Describing the Energy and Spectroscopy of Defect Sites in Hexagonal Boron Nitride. *Journal of Chemical Theory and Computation* **14,** 1602–1613. ISSN: 15499626 (2018).

249. Ovesn ý, M., Křížek, P., Borkovec, J., Švindrych, Z. & Hagen, G. M. ThunderSTORM: A comprehensive ImageJ plug-in for PALM and STORM data analysis and super-resolution imaging. *Bioinformatics* **30,** 2389–2390. ISSN: 14602059 (2014).

250. Gao, L. *et al.* Repeated growth and bubbling transfer of graphene with millimetre-size single-crystal grains using platinum. *Nature Communications* **3,** 697–699. ISSN: 20411723 (2012).

251. Gonzalez Marin, J. F., Unuchek, D., Watanabe, K., Taniguchi, T. & Kis, A. MoS2 photodetectors integrated with photonic circuits. *npj 2D Materials and Applications* **3.** ISSN: 2397-7132. http://dx.doi.org/10.1038/s41699-019-0096-4 (2019).

252. Xia, F., Wang, H., Xiao, D., Dubey, M. & Ramasubramaniam, A. Two-dimensional material nanophotonics. *Nature Photonics* **8,** 899–907. ISSN: 17494893. arXiv: 1410.3882 (2014).

253. Shiue, R.-J. *et al.* Active 2D materials for on-chip nanophotonics and quantum optics. *Nanophotonics* **6** (2017).

254. Tongay, S. *et al.* Defects activated photoluminescence in two-dimensional semiconductors: Interplay between bound, charged, and free excitons. *Scientific Reports* **3,** 1–5. ISSN: 20452322 (2013).

255. Nan, H. *et al.* Strong photoluminescence enhancement of MoS2 through defect engineering and oxygen bonding. *ACS Nano* **8,** 5738–5745. ISSN: 1936086X (2014).

256. Cun, H. *et al.* Centimeter-Sized Single-Orientation Monolayer Hexagonal Boron Nitride with or Without Nanovoids. *Nano Letters* **18,** 1205–1212. ISSN: 15306992. https://doi.org/10.1021/acs.nanolett.7b04752 (2018).

257. Cun, H. *et al.* Wafer-scale MOCVD growth of monolayer MoS2 on sapphire and SiO2. *Nano Research* **12,** 2646–2652. ISSN: 19980000. https://doi.org/10.1007/s12274-019-2502-9 (2019).

258. Dertinger, T., Colyera, R., Iyer, G., Weiss, S. & Enderlein, J. Fast, background-free, 3D super-resolution optical fluctuation imaging (SOFI). *Proceedings of the National Academy of Sciences* **106,** 22287–22292. ISSN: 00278424. https://www.pnas.org/content/106/52/22287 (2009).

259. Fu, Y. *et al.* Axial superresolution via multiangle TIRF microscopy with sequential imaging and photobleaching. *Proceedings of the National Academy of Sciences* **113,** 4368–4373. ISSN: 0027-8424 (2016).

260. Tinguely, J.-C., Helle, Ø. I. & Ahluwalia, B. S. Silicon nitride waveguide platform for fluorescence microscopy of living cells. *Optics Express* **25,** 27678. ISSN: 1094-4087 (2017).

261. Diekmann, R. *et al.* Chip-based wide field-of-view nanoscopy. *Nature Photonics* **11,** 322–328. ISSN: 17494893 (2017).

262. Mak, K. F., Lee, C., Hone, J., Shan, J. & Heinz, T. F. Atomically thin MoS2: A new direct-gap semiconductor. *Physical Review Letters* **105,** 2–5. ISSN: 00319007 (2010).

263. Splendiani, A. *et al.* Emerging photoluminescence in monolayer MoS2. *Nano Letters* **10,** 1271–1275. ISSN: 15306984 (2010).

264. Cong, C. *et al.* Synthesis and optical properties of large-area single-crystalline 2D semiconductor WS2 monolayer from chemical vapor deposition. *Advanced Optical Materials* **2,** 131–136. ISSN: 21951071 (2014).

265. Li, H., Zhu, X., Tang, Z. K. & Zhang, X. H. Low-temperature photoluminescence emission of monolayer MoS2 on diverse substrates grown by CVD. *Journal of Luminescence* **199,** 210–215. ISSN: 00222313 (2018).

266. Ciarrocchi, A. *et al.* Polarization switching and electrical control of interlayer excitons in two-dimensional van der Waals heterostructures. *Nature Photonics* **13,** 131–136. ISSN: 17494893. https://doi.org/10.1038/s41566-018-0325-y (2019).

267. Amani, M. *et al.* Near-unity photoluminescence quantum yield in MoS2. *Science* **350,** 1065–1068. ISSN: 10959203. arXiv: arXiv:1011.1669v3. http://science.sciencemag.org/content/350/6264/1065 (2015).

268. Mouri, S., Miyauchi, Y. & Matsuda, K. Tunable photoluminescence of monolayer MoS2 via chemical doping. *Nano Letters* **13,** 5944–5948. ISSN: 15306984 (2013).

269. Molas, M. R. *et al.* The optical response of monolayer, few-layer and bulk tungsten disulfide. *Nanoscale* **9,** 13128–13141. ISSN: 20403372. arXiv: 1706.09285 (2017).

270. Rabouw, F. T. *et al.* Non-blinking single-photon emitters in silica. *Scientific Reports* **6,** 1–7. ISSN: 20452322. arXiv: 1509.07262 (2016).

271. Pfeiffer, M. H. P. *et al.* Ultra-smooth silicon nitride waveguides based on the Damascene reflow process: fabrication and loss origins. *Optica* **5,** 884. ISSN: 2334-2536 (2018).

272. Abràmoff, M. D., Magalhães, P. J. & Ram, S. J. Image processing with imageJ. *Biophotonics International* **11,** 36–41. ISSN: 10818693. https://dspace.library.uu.nl/handle/1874/204900 (2004).

273. Abidi, I. H. *et al.* Selective Defect Formation in Hexagonal Boron Nitride. *Advanced Optical Materials* **7.** ISSN: 21951071. arXiv: 1902.07932 (2019).

274. Narayana Deepak, K. L., Rao, V. & Rao, N. Direct Writing in Polymers with Femtosecond Laser Pulses: Physics and Applications. *Laser Pulses - Theory, Technology, and Applications* (2012).

275. Cho, K. *et al.* Electrical and Optical Characterization of MoS2 with Sulfur Vacancy Passivation by Treatment with Alkanethiol Molecules. *ACS Nano* **9,** 8044–8053. ISSN: 1936086X. https://doi.org/10.1021/acsnano.5b04400 (2015).

276. Luo, P. *et al.* Doping engineering and functionalization of two-dimensional metal chalcogenides. *Nanoscale Horizons* **4,** 26–51. ISSN: 20556764 (2019).

277. Dumcenco, D. *et al.* Large-area epitaxial monolayer moS2. *ACS Nano* **9,** 4611–4620. ISSN: 1936086X. arXiv: 1405.0129. https://doi.org/10.1021/acsnano.5b01281 (2015).

278. Graf, M. *et al.* Fabrication and practical applications of molybdenum disulfide nanopores. *Nature Protocols* **14,** 1130–1168. ISSN: 17502799. https://doi.org/10.1038/s41596-019-0131-0 (2019).

279. Edelstein, A., Amodaj, N., Hoover, K., Vale, R. & Stuurman, N. Computer control of microscopes using uManager. *Current Protocols in Molecular Biology,* 1–17. ISSN: 19343639 (2010).

280. Vancsó, P. *et al.* The intrinsic defect structure of exfoliated MoS2 single layers revealed by Scanning Tunneling Microscopy. *Scientific Reports* **6,** 1–7. ISSN: 20452322 (2016).

281. Glushkov, E. *et al.* Waveguide-Based Platform for Large-FOV Imaging of Optically Active Defects in 2D Materials. *ACS Photonics* **6,** 3100–3107. ISSN: 23304022 (2019).

282. Li, X. *et al.* Large-area synthesis of high-quality and uniform graphene films on copper foils. *Science* **324,** 1312–1314. ISSN: 00368075 (2009).

283. Gao, L. *et al.* Repeated growth and bubbling transfer of graphene with millimetre-size single-crystal grains using platinum. *Nature Communications* **3.** ISSN: 20411723 (2012).

284. Hallam, T., Berner, N. C., Yim, C. & Duesberg, G. S. Strain, Bubbles, Dirt, and Folds: A Study of Graphene Polymer-Assisted Transfer. *Advanced Materials Interfaces* **1.** ISSN: 21967350 (2014).

285. Stehle, Y. Y. *et al.* Effect of polymer residues on the electrical properties of large-area graphene-hexagonal boron nitride planar heterostructures. *Nanotechnology* **28.** ISSN: 13616528 (2017).

286. Song, L. *et al.* Large scale growth and characterization of atomic hexagonal boron nitride layers. *Nano Letters* **10,** 3209–3215. ISSN: 15306984 (2010).

287. Duong, N. M. H. *et al.* Facile production of hexagonal boron nitride nanoparticles by cryogenic exfoliation. *Nano Letters* **19.** ISSN: 1530-6984. http://pubs.acs.org/doi/10.1021/acs.nanolett.9b01913 (2019).

288. Bocquet, L. Nanofluidics coming of age. *Nature materials* **19,** 254–256. ISSN: 14761122. http://dx.doi.org/10.1038/s41563-020-0625-8 (2020).

289. Urban, B. E. *et al.* Subsurface Super-resolution Imaging of Unstained Polymer Nanostructures. *Scientific Reports* **6,** 2–10. ISSN: 20452322. http://dx.doi.org/10.1038/srep28156 (2016).

290. Kreuer, K. D. Proton conductivity: Materials and applications. *Chemistry of Materials* **8,** 610–641. ISSN: 08974756 (1996).

291. Chen, M. *et al.* Hydroxide diffuses slower than hydronium in water because its solvated structure inhibits correlated proton transfer. *Nature Chemistry* **10,** 413–419. ISSN: 17554349 (2018).

292. Reider, G., Höfer, U. & Heinz, T. Surface diffusion of hydrogen on Si (111) 7× 7. *Physical review letters* **66,** 1994–1997 (1991).

293. Merte, L. R. *et al.* Water-mediated proton hopping on an iron oxide surface. *Science* **336,** 889–893. ISSN: 10959203 (2012).

294. Kumagai, T. *et al.* H-atom relay reactions in real space. *Nature Materials* **11,** 167–172. ISSN: 14764660 (2012).

295. Tocci, G. & Michaelides, A. Solvent-induced proton hopping at a water-oxide interface. *Journal of Physical Chemistry Letters* **5,** 474–480. ISSN: 19487185 (2014).

296. Nagasaka, M., Kondoh, H., Amemiya, K., Ohta, T. & Iwasawa, Y. Proton transfer in a two-dimensional hydrogen-bonding network: Water and hydroxyl on a Pt(111) surface. *Physical Review Letters* **100,** 8–11. ISSN: 00319007 (2008).

297. Grosjean, B., Bocquet, M. L. & Vuilleumier, R. Versatile electrification of two-dimensional nanomaterials in water. *Nature Communications* **10,** 1–8. ISSN: 20411723 (2019).

298. Bränden, M., Sanden, T., Brzezinkski, P. & Widengren, J. Localized proton microcircuits at the biological membrane–water interface. *Proceedings of the National Academy of Sciences.* ISSN: 0027-8424 (2006).

299. Cherepanov, D. A., Pohl, P., Hagen, V., Antonenko, Y. N. & Springer, A. Protons migrate along interfacial water without significant contributions from jumps between ionizable groups on the membrane surface. *Proceedings of the National Academy of Sciences* **108,** 14461–14466. ISSN: 0027-8424 (2011).

300. Serowy, S. *et al.* Structural proton diffusion along lipid bilayers. *Biophysical Journal* **84,** 1031–1037. ISSN: 00063495 (2003).

301. Zhang, C. *et al.* Water at hydrophobic interfaces delays proton surface-to-bulk transfer and provides a pathway for lateral proton diffusion. *Proceedings of the National Academy of Sciences* **109,** 9744–9749. ISSN: 0027-8424 (2012).

302. Karim, W. *et al.* Catalyst support effects on hydrogen spillover. *Nature* **541,** 68–71. ISSN: 14764687 (2017).

303. Michaelides, A. & Hu, P. Catalytic water formation on platinum: A first-principles study. *Journal of the American Chemical Society* **123,** 4235–4242. ISSN: 00027863 (2001).

304. Cortright, R. D., Davda, R. R. & Dumesic, J. A. Hydrogen from catalytic reforming of biomass-derived hydrocarbons in liquid water. *Nature* **418,** 964–967. ISSN: 00280836 (2002).

305. Schmidt-Rohr, K. & Chen, Q. Parallel cylindrical water nanochannels in Nafion fuel-cell membranes. *Nature Materials* **7,** 75–83. ISSN: 14764660 (2008).

306. Hickner, M. A., Ghassemi, H., Kim, Y. S., Einsla, B. R. & McGrath, J. E. Alternative Polymer Systems for Proton Exchange Membranes (PEMs). *Chemical Reviews* **104,** 4587–4612. ISSN: 0009-2665 (2004).

307. Kreuer, K.-D., Paddison, S. J., Spohr, E. & Schuster, M. Transport in Proton Conductors for Fuel-Cell Applications: Simulations, Elementary Reactions, and Phenomenology. *Chemical Reviews* **104,** 4637–4678. ISSN: 0009-2665 (2004).

308. Ling, X., Bonn, M., Domke, K. F. & Parekh, S. H. Correlated interfacial water transport and proton conductivity in perfluorosulfonic acid membranes. *Proceedings of the National Academy of Sciences* **116,** 8715–8720. ISSN: 0027-8424 (2019).

309. Boysen, D. A., Uda, T., Chisholm, C. R. I. & Haile, S. M. High-Performance Solid Acid Fuel Cells Through Humidity Stabilization. *Science* **303,** 68–70. ISSN: 00368075 (2004).

310. Gopinadhan, K. *et al.* Complete steric exclusion of ions and proton transport through confined monolayer water. *Science (New York, N.Y.)* **363,** 145–148. ISSN: 1095-9203 (2019).

311. Lee, C. Y., Choi, W., Han, J.-H. & Strano, M. S. Coherence Resonance in a Single-Walled Carbon Nanotube Ion Channel. *Science* **329,** 1320–1324. ISSN: 0036-8075 (2010).

312. Tunuguntla, R. H. *et al.* Enhanced water permeability and tunable ion selectivity in subnanometer carbon nanotube porins. **796,** 792–796 (2017).

313. Zhou, K. G. *et al.* Electrically controlled water permeation through graphene oxide membranes. *Nature* **559,** 236–240. ISSN: 14764687 (2018).

314. Freier, E., Wolf, S. & Gerwert, K. Proton transfer via a transient linear water-molecule chain in a membrane protein. *Proceedings of the National Academy of Sciences* **108,** 11435–11439. ISSN: 00278424 (2011).

315. Wendt, S. *et al.* Formation and Splitting of Paired Hydroxyl Groups on Reduced TiO2. *Physical Review Letters* **96,** 066107. ISSN: 0031-9007 (2006).

316. Léonard, S., Ingrid, S., Frédéric, F., Annick, L. & Julien, B. Characterization methods dedicated to nanometer-thick hBN layers. *2D Materials* **4,** 15028 (2017).

317. Vogl, T., Buchler, B. C., Lu, Y. & Lam, P. K. Fabrication and Deterministic Transfer of High-Quality Quantum Emitters in Hexagonal Boron Nitride. *ACS Photonics* **5,** 2305–2312 (2018).

318. Wang, N. *et al.* Magnetic Criticality Enhanced Hybrid Nanodiamond Thermometer under Ambient Conditions. *Physical Review X* **8,** 1–21. ISSN: 21603308 (2018).

319. Agmon, N. Elementary steps in excited-state proton transfer. *Journal of Physical Chemistry A* **109,** 13–35. ISSN: 10895639 (2005).

320. Scharnagl, C., Raupp-Kossmann, R. & Fischer, S. F. Molecular basis for pH sensitivity and proton transfer in green fluorescent protein: Protonation and conformational substates from electrostatic calculations. *Biophysical Journal* **77,** 1839–1857. ISSN: 00063495 (1999).

321. Habuchi, S. *et al.* Photo-induced protonation/deprotonation in the GFP-like fluorescent protein Dronpa: Mechanism responsible for the reversible photoswitching. *Photochemical and Photobiological Sciences* **5,** 567–576. ISSN: 1474905X (2006).

322. Janssen, K. P. *et al.* Single molecule methods for the study of catalysis: From enzymes to heterogeneous catalysts. *Chemical Society Reviews* **43,** 990–1006. ISSN: 03060012 (2014).

323. Roeffaers, M. B. *et al.* Spatially resolved observation of crystal-face-dependent catalysis by single turnover counting. *Nature* **439,** 572–575. ISSN: 14764687 (2006).

324. Zou, N. *et al.* Cooperative communication within and between single nanocatalysts. *Nature Chemistry* **10,** 607–614. ISSN: 17554349 (2018).

325. Manley, S. *et al.* High-density mapping of single-molecule trajectories with photoactivated localization microscopy. *Nature Methods* **5,** 155–157. ISSN: 15487091 (2008).

326. Bouchaud, J. P., Comtet, A., Georges, A. & Le Doussal, P. Classical diffusion of a particle in a one-dimensional random force field. *Annals of Physics* **201,** 285–341. ISSN: 1096035X (1990).

327. Zaburdaev, V., Denisov, S. & Klafter, J. Lévy walks. *Reviews of Modern Physics* **87,** 483–530. ISSN: 15390756 (2015).

328. Heberle, J., Riesle, J., Thiedemann, G., Oesterhelt, D. & Dencher, N. A. Proton migration along the membrane surface and retarded surface to bulk transfer. *Nature* **370,** 379–382. ISSN: 00280836 (1994).

329. Halle, B. & Karlström, G. Prototropic charge migration in water. *J.Chem.Soc., Faraday Trans* **79,** 1047–1073 (1983).

330. Sluyters, J. H. & Sluyters-Rehbach, M. The mechanism of the hydrogen ion conduction in liquid light and heavy water derived from the temperature dependence of their limiting conductivities. *Journal of Physical Chemistry B* **114,** 15582–15589. ISSN: 15205207 (2010).

331. Eilers, Y., Ta, H., Gwosch, K. C., Balzarotti, F. & Hell, S. W. MINFLUX monitors rapid molecular jumps with superior spatiotemporal resolution. *Proceedings of the National Academy of Sciences* **115,** 6117–6122. ISSN: 10916490 (2018).

332. Reed, D. A. & Ehrlich, G. Surface diffusion, atomic jump rates and thermodynamics. *Surface Science* **102,** 588–609. ISSN: 00396028 (1981).

333. Weichselbaum, E. *et al.* Origin of proton affinity to membrane/water interfaces. *Scientific Reports* **7,** 1–8. ISSN: 20452322 (2017).

334. Kudin, K. N. & Car, R. Why are water-hydrophobic interfaces charged? *Journal of the American Chemical Society* **130,** 3915–3919. ISSN: 00027863 (2008).

335. Tocci, G., Joly, L. & Michaelides, A. Friction of water on graphene and hexagonal boron nitride from ab initio methods: very different slippage despite very similar interface structures. *Nano Letters* **14,** 6872–6877. ISSN: 1530-6984 (2014).

336. Dellago, C. & Hummer, G. Kinetics and mechanism of proton transport across membrane nanopores. *Physical Review Letters* **97,** 1–4. ISSN: 00319007 (2006).

337. Radha, B. *et al.* Molecular transport through capillaries made with atomic-scale precision. *Nature* **538,** 222–225. ISSN: 14764687 (2016).

338. Tran, T. T. *et al.* Robust Multicolor Single Photon Emission from Point Defects in Hexagonal Boron Nitride. *ACS Nano* **10,** 7331–7338. ISSN: 1936086X. arXiv: 1603.09608 (2016).

339. Koperski, M. *et al.* Midgap radiative centers in carbon-enriched hexagonal boron nitride. *Proceedings of the National Academy of Sciences* **117,** 13214–13219. ISSN: 10916490 (2020).

340. Fox, D. S. *et al.* Nanopatterning and Electrical Tuning of MoS2 Layers with a Subnanometer Helium Ion Beam. *Nano Letters* **15,** 5307–5313 (2015).

341. Mupparapu, R. *et al.* Facile Resist-Free Nanopatterning of Monolayers of MoS2 by Focused Ion-Beam Milling. *Advanced Materials Interfaces* **7.** ISSN: 21967350 (2020).

342. Giannuzzi, L. & Smith, N. TEM Specimen Preparation with Plasma FIB Xe + Ions. *Microscopy and Microanalysis* **17,** 646–647. ISSN: 1431-9276 (2011).

343. Zhong, X. *et al.* Comparing Xe+pFIB and Ga+FIB for TEM sample preparation of Al alloys: Minimising FIB-induced artefacts. *Journal of Microscopy* **282,** 101–112. ISSN: 0022-2720. https://doi.org/10.1111/jmi.12983 (2021).

344. Schué, L., Stenger, I., Fossard, F., Loiseau, A. & Barjon, J. Characterization methods dedicated to nanometer-thick hBN layers. *2D Materials* **4,** 15028 (2016).

345. Streletskii, A. N., Permenov, D. G., Bokhonov, B. B., Leonov, A. V. & Mudretsova, S. N. Mechanochemistry of hexagonal boron nitride. 2. Reactivity upon interaction with water. *Colloid Journal* **72,** 553–558. ISSN: 1061933X (2010).

346. Speiser, A. *et al.* Deep learning enables fast and dense single-molecule localization with high accuracy. *bioRxiv,* 1–28. ISSN: 26928205 (2020).

347. Kalhor, N., Boden, S. A. & Mizuta, H. Microelectronic Engineering Sub-10 nm patterning by focused He-ion beam milling for fabrication of downscaled graphene nano devices. *MICROELECTRONIC ENGINEERING* **114,** 70–77. ISSN: 0167-9317. http://dx.doi.org/10.1016/j.mee.2013.09.018 (2014).

348. Buchheim, J., Wyss, R. M., Shorubalko, I. & Park, H. G. Understanding the interaction between energetic ions and freestanding graphene towards practical 2D perforation. *Nanoscale* **8,** 8345–8354. ISSN: 20403372 (2016).

349. Shorubalko, I., Choi, K., Stiefel, M. & Park, H. G. Ion beam profiling from the interaction with a freestanding 2D layer. *Beilstein Journal of Nanotechnology* **8,** 682–687. ISSN: 21904286 (2017).

350. Ovesn, M., Křížek, P., Borkovec, J., Švindrych, Z. & Hagen, G. M. ThunderSTORM: a comprehensive ImageJ plug-in for PALM and STORM data analysis and super-resolution imaging. *Bioinformatics* **30,** 2389–2390 (2014).

351. Geissbuehler, S. *et al.* Mapping molecular statistics with balanced super-resolution optical fluctuation imaging (bSOFI). *Optical Nanoscopy* **1,** 1–7. ISSN: 21922853 (2012).

352. Aslam, N. *et al.* Nanoscale nuclear magnetic resonance with chemical resolution. *Science* **357,** 67–71. ISSN: 10959203 (2017).

353. Glenn, D. R. *et al.* High-resolution magnetic resonance spectroscopy using a Solid-State spin sensor. *Nature* **555,** 351–354. ISSN: 14764687 (2018).

354. Morimoto, K. *et al.* Megapixel time-gated SPAD image sensor for 2D and 3D imaging applications. *Optica* **7,** 346. ISSN: 2334-2536. arXiv: 1912.12910 (2020).

355. Zickus, V. *et al.* Fluorescence lifetime imaging with a megapixel SPAD camera and neural network lifetime estimation. *Scientific Reports* **10,** 1–10. ISSN: 20452322. https://doi.org/10.1038/s41598-020-77737-0 (2020).

356. Wen, C. *et al.* Advanced Data Encryption using 2D Materials. *Advanced Materials* **33,** 2100185.

357. Liu, W. *et al.* Temperature-dependent energy-level shifts of Spin Defects in hexagonal Boron Nitride, 1–6. arXiv: 2101.09920. http://arxiv.org/abs/2101.09920 (2021).

358. Gottscholl, A. *et al.* Sub-nanoscale Temperature, Magnetic Field and Pressure sensing with Spin Centers in 2D hexagonal Boron Nitride, 1–9. arXiv: 2102.10890. http://arxiv.org/abs/2102.10890 (2021).

359. Priyadarshi, A. *et al.* A transparent waveguide chip for versatile TIRF-based microscopy and nanoscopy. *arXiv preprint arXiv:2006.07275* (2020).

Evgenii Glushkov | CV

Chemin de Champagne, 2 – 1025 St-Sulpice – Switzerland
+41 78 971 48 30 • evgenii.glushkov@epfl.ch
instagram.com/phdsuisse • linkedin.com/in/evgenii-glushkov

Education

École polytechnique fédérale de Lausanne — **Lausanne**
PhD — *2016–to date*
Microsystems and Microelectronics

Moscow Institute of Physics and Technology — **Dolgoprudnii**
Masters, 4.8/5 — *2014–2016*
Physics and Technology of Nanostructures

Moscow Institute of Physics and Technology — **Dolgoprudnii**
Bachelors, 4.5/5 — *2010–2014*
Applied Physics and Mathematics

Work and Research

Laboratory of Nanoscale Biology — **EPFL**
prof. Aleksandra Radenovic — *2016–to date*
Optically-active defects as quantum probes for imaging and sensing.

Laboratory of Artificial Quantum Systems — **MIPT**
prof. Oleg Astafiev — *2014–2016*
Superconducting circuits for quantum optics.

Laboratory of Photonics and Quantum Measurements — **EPFL**
prof. Tobias Kippenberg — *07.2015–12.2015*
Circuit electromechanics with 3D cavities.

Laboratory of Superconducting Metamaterials — **NUST MISIS**
prof. Alexey Ustinov — *2013–2015*
Superconducting flux qubits.

Research Topics

- Super-resolution microscopy
- Design & fabrication of nanostructures
- Optically-active defects in novel materials
- Quantum optics & Quantum Information

Skills & Experience

Science education & outreach: Teaching physics to high school and university students, writing for popular science magazines, presenting at various sci-comm events

Optics: Designing, building and maintaining various home-built optical microscopes

Programming: Python, Matlab, LabVIEW, C, Arduino

Organization: Leading full-stack organization & planning of multiple online & in-person science-related events ranging from tens to hundreds of participants

Cleanroom fabrication: 6 years of experience in micro- and nanofabrication

Simulation & Design: COMSOL, SolidWorks, Autodesk Inventor

Science Education & Outreach

My passion for teaching physics was ignited by my incredible physics teacher in high school. Since my Bachelor's I was teaching physics-related subjects first to middle- and high school students (including *summer camps*), and then to university students. With the support of several personal grants (*Potanin Scholarship*, *Rosmolodezh*, *Moscow Government Scholarship*), I was also developing study plans and educational activities (including hands-on experiments) for all of these courses.
Alongside that I was writing for multiple popular science magazines (`nplus1.ru`, `novayagazeta.ru`, `nauka.tass.ru`), giving talks at sci-comm events and participating in competitions for young scientists: *Exposure Science Film Hackathon*, *My Thesis in 180 seconds*, *Science Slam*, *EPFL Open Days* (where I presented my portable fluorescence microscope), etc. I was also one of the authors of a *popular science comic book*, that was published in collaboration with *Skoltech*.
During my PhD I highly enjoyed supervising students, both for individual lab projects and team competitions. In 2016-2018, I was a team leader of EPFL teams for two international student competitions: International Physicists' Tournament (IPT, `iptnet.info`) and SensUs Biosensor Competition (`sensus.org`). Both teams won the competitions in 2018.

Experience as an organizer

I've been organizing multiple science-related events: monthly Symposium for PhD students at EPFL, a Summer School in Davos, a Scientific Meeting for my research center (NCCR Bio-inspired Materials). Since 2017 I serve as the representative of the International Physicists' Tournament in Switzerland, responsible for organizing the Swiss National Selections and forming the Swiss national team. I was also leading the organization of the IPT 2019 for more than 200 students from 20 countries.

Recent Publications

- Comtet, J., Grosjean, B., **Glushkov, E.** et al. Direct observation of water-mediated single-proton transport between hBN surface defects. Nature Nanotechnology 15, 598–604 (2020).
- **Glushkov, E.** et al. Waveguide-Based Platform for Large-FOV Imaging of Optically Active Defects in 2D Materials. ACS Photonics 6, 3100–3107 (2019).
- Duong, N. M. H., **Glushkov, E.** et al. Facile production of hexagonal boron nitride nanoparticles by cryogenic exfoliation. Nano Lett. 19, (2019).
- Comtet, J., **Glushkov, E.** et al. Wide-Field Spectral Super-Resolution Mapping of Optically Active Defects in Hexagonal Boron Nitride. Nano Lett. 19, 2516–2523 (2019).
- Archetti, A., **Glushkov, E.** et al. Waveguide-PAINT offers an open platform for large field-of-view super-resolution imaging. Nature Communications, 10 (2019).
- **Glushkov, E.**, Navikas, V., Radenovic, A. Fluorescent nanodiamonds as versatile intracellular temperature sensors. Chimia, 73, 73-77 (2019).
- Full list of publications: https://scholar.google.com/citations?user=0wA2zzYAAAAJ

Languages

Russian: C2	*Mother tongue*
English: C1	*Fluent*
French: B2	*EPFL Language Center*
German: B2	*DSH-2*